



저작자표시-비영리-변경금지 2.0 대한민국

이용자는 아래의 조건을 따르는 경우에 한하여 자유롭게

- 이 저작물을 복제, 배포, 전송, 전시, 공연 및 방송할 수 있습니다.

다음과 같은 조건을 따라야 합니다:



저작자표시. 귀하는 원저작자를 표시하여야 합니다.



비영리. 귀하는 이 저작물을 영리 목적으로 이용할 수 없습니다.



변경금지. 귀하는 이 저작물을 개작, 변형 또는 가공할 수 없습니다.

- 귀하는, 이 저작물의 재이용이나 배포의 경우, 이 저작물에 적용된 이용허락조건을 명확하게 나타내어야 합니다.
- 저작권자로부터 별도의 허가를 받으면 이러한 조건들은 적용되지 않습니다.

저작권법에 따른 이용자의 권리는 위의 내용에 의하여 영향을 받지 않습니다.

이것은 [이용허락규약\(Legal Code\)](#)을 이해하기 쉽게 요약한 것입니다.

[Disclaimer](#)

Ph.D. Dissertation of Engineering

In-vivo Sap Flow Measurement System Using Microneedle Sensor

미세 바늘 센서를 이용한
생체 내 수액 흐름 측정 시스템

August 2018

**Graduate School of Seoul National University
Department of Mechanical and Aerospace Engineering**

Sangwoong Baek

In-vivo Sap Flow Measurement System Using Microneedle Sensor

Supervisor: Prof. Junghoon Lee

Submitting a Ph.D. Dissertation of Public
Administration

April 2018

Graduate School of Seoul National University
Department of Mechanical and Aerospace Engineering
Sangwoong Baek

Confirming the Ph.D. Dissertation written by
Sangwoong Baek

June 2018

Chair _____ 최 해 천 (Seal)

Vice Chair _____ 이 정 훈 (Seal)

Examiner _____ 고 승 환 (Seal)

Examiner _____ 손 정 익 (Seal)

Examiner _____ 조 일 환 (Seal)

Abstract

In-vivo Sap Flow Measurement System Using Microneedle Sensor

Sangwoong Baek
Department of Mechanical
and Aerospace Engineering
Graduate School of
Seoul National University

Measurement of xylem sap flow is essential in understanding plant physiology in agriculture. Advanced hydroponics, for instance, require sap flow measurement to observe the plant reaction to environmental variables such as sunlight, humidity, and soil water content. However, most conventional approaches for sap flow measurement have been limited to large woody plants. Plants grown in hydroponics, e.g., tomatoes and bell peppers, are smaller and softer, and thus can hardly survive the invasion of thick thermal probes for flow speed measurement. A microneedle thermal probe system that can be implanted into a small plant was developed for the measurement of sap flow through the xylem. The microneedle sap flow sensor and its measurement method were presented. The thermal property of microneedle probe was studied with analytical model and multiphysics simulation. The microneedle sap flow sensor was fabricated with MEMS fabrication process. The measurement system including electronics and data acquisition setup was prepared. The calibration of the sensor was conducted for xylem flow. Tests with a tomato stem resulted in a universal calibration model that can be applied to the same species. The sensors were installed to greenhouse plants to measure the in-vivo signal for total of 612 days. More than 207 sensors were installed and sap flow and internal relative temperature were measured in field. We demonstrate routine measurements of sap flow in

greenhouse plants including tomato plant over a month, opening up the possibility for production scale application. A microscale hot wire on a single probe benefits from small-scale physics with a simple configuration. The single probe enables minimally invasive measurement with a minimal thermal impact on plant tissues.

Keywords: Fluid flow measurement, in-vivo sensor, MEMS, Plant implantable sensor

Student Number: 2012 - 22557

Table of Contents

Abstract	i
Table of Contents	iii
List of Figures	ix
List of Tables	xviii
Chapter 1. General Introduction.....	1
1.1. Background of research	1
1.1.1. Importance of measuring biometric information in greenhouse cultivation	1
1.1.2. Importance of sap flow as biometric information	2
1.1.3. Thermometric sap flow measurement methods	4
1.1.4. Demand for minimally invasive measurements.....	9
1.1.5. MEMS implantable microneedle sensors	9
1.1.6. Benefits of microscale needle probe in thermal characteristic aspects	1 0
1.2. Research objective	1 1
Bibliography	1 2
Chapter 2. Methods, Design and Fabrication	1 7
2.1. Design of microneedle sap flow sensor probe	1 7
2.1.1. Sap flow measurement with heat dissipation method.....	1 7
2.1.2. Sap flow measurement method with a single thermal probe ..	1 8
2.1.3. Determination of T_M	2 0
2.1.4. Thermal design of microneedle probe	2 3
2.1.5. Structural design of microneedle probe	2 4
2.1.6. Target performance of the sensor	2 5

2.2.	Fabrication of microneedle sap flow sensor	2 7
2.2.1.	Fabrication process of microneedle sensor	2 7
2.2.2.	Packaging of the sensor	2 9
2.3.	Measurement circuit design and fabrication	3 1
2.3.1.	Design of measurement circuit	3 1
2.3.2.	Fabrication of the measurement circuit.....	3 2
2.3.3.	Evaluatoin of measurement system.	3 3
2.4.	Design for electrical breakdown prevention	3 6
2.4.1.	What is electrical breakdown.....	3 6
2.4.2.	Analysis of electrical breakdown phenomena	3 6
2.4.3.	Elelctrode patterning process to minimize electrical breakdown	3 8
2.4.4.	Composite dielectric layer process to minimize electrical breakdown	4 1
2.4.5.	Negative vottage driving to minimize electrical breakdown ..	4 2
2.5.	Configuration of complete measurement system.....	4 4
2.6.	Performance specification of the measurement system	4 5
2.7.	Conclusion	4 6
	Bibliography	4 7
Chapter 3. Theory and Analysis.....		5 1
3.1.	Thermal analysis of microneedle probe	5 1
3.1.1.	Theoretical background and assumptions	5 1
3.1.2.	Energy equation for conjugated heat transfer in porous media	5 2
3.1.3.	Lumped capacitance method.....	5 3
3.1.4.	Comparison between convective heat transfer versus conduction heat transfer in conjugatd heat transfer.	5 4
3.1.5.	Single component lumped capacitance model, transient state response	5 7

3.1.6.	Steady state response of single component lumped capacitance model	5 9
3.1.7.	Multi component lumped capacitance model	6 1
3.2.	Simulation analysis of microneedle probe	6 4
3.2.1.	Simulation method	6 4
3.2.2.	Transition heat transfer simulation	6 5
3.2.3.	Steady-state heat transfer simulation	6 7
3.3.	Conclusion	7 0
	Bibliography	7 1

Chapter 4. Thermal Characterization and Calibration..... 7 3

4.1.	Analysis of thermal characteristics by heating power	7 3
4.1.1.	Basic thermal property of microneedle probe.....	7 3
4.1.2.	Heating power of microneedle probe.....	7 4
4.1.3.	Analysis of the experimental result with lumped capacitance model	7 6
4.2.	Thermal characterization and calibration of microneedle.....	8 0
4.2.1.	Calibration of microneedle probe	8 0
4.2.2.	Pipe flow: calibration method.....	8 0
4.2.3.	Pipe flow: thermal characterization	8 1
4.2.4.	Pipe flow: calibration result	8 4
4.2.5.	Xylem flow: calibration method	8 8
4.2.6.	Xylem flow: thermal characterization	9 0
4.2.7.	Xylem flow: calibration result	9 2
4.2.8.	Comparison between calibration for pipe and calibration for xylem flow	9 5
4.3.	Conclusion	9 6
	Bibliography	9 7

Chapter 5. In-Vivo Measurement of Microneedle Sap Flow Sensor 9 9

5.1.	Measurement of sap flow by artificial light.....	9 9
5.1.1.	Artificial light experiment method.....	9 9
5.1.2.	Result of artificial light experiment	1 0 0
5.1.3.	Conclusion of artificial light experiment	1 0 2
5.2.	In-vivo measurement of tomato plant	1 0 4
5.2.1.	Field measurement method for tomato plant	1 0 4
5.2.2.	Long-term measurement of tomato plant in greenhouse	1 0 6
5.2.3.	Result of long-term measurement of tomato plant in greenhouse.	1 0 6
5.2.4.	Comparison between environmental variables and sap flow	1 1 1
5.2.5.	Result of comparison between environment variables and sap flow	1 1 1
5.2.6.	Irrigation cut test.....	1 1 7
5.2.7.	Result of irrigation cut test.....	1 1 8
5.2.8.	Mass population measurement of sap flow signal	1 2 1
5.2.9.	Statistical use of sap flow signal.....	1 2 2
5.2.10.	Pedicle / peduncle sap flow measurement	1 2 7
5.2.11.	Result of pedicle / peduncle measurement.....	1 2 8
5.2.12.	Conclusion of in-vivo measurement of tomato plant.....	1 3 0
5.3.	In-vivo measurement of other plants	1 3 1
5.3.1.	Measurement methods	1 3 1
5.3.2.	In-vivo measurement of paprika	1 3 1
5.3.3.	In-vivo measurement of cucumber	1 3 2
5.3.4.	In-vivo measurement of clusia.....	1 3 3
5.3.5.	In-vivo measurement of rubber tree.....	1 3 6
5.4.	Microneedle implantation effect	1 3 8
5.5.	Conclusion	1 4 1

Bibliography	1	4	2
Chapter 6. Compensation of Natural Temperature Gradient.....	1	4	3
6.1. Introduction to natural temperature gradient (NTG).....	1	4	3
6.1.1. What is NTG.....	1	4	3
6.1.2. Effect of NTG in sap flow measurement	1	4	3
6.2. Compensation of NTG.....	1	4	5
6.2.1. Compensation method for NTG.....	1	4	5
6.2.2. NTG compensaion result	1	4	8
6.3. Conclusion	1	5	2
Bibliography	1	5	3
Chapter 7. Array Sensor Measurement.....	1	5	5
7.1. Introduction.....	1	5	5
7.1.1. Measurement of sap flow distribution	1	5	5
7.2. Design and fabrication	1	5	7
7.2.1. Sensor design	1	5	7
7.2.2. Sensor fabrication	1	5	9
7.3. Test and calibration.....	1	6	1
7.3.1. Operation power test.....	1	6	1
7.3.2. Calibration	1	6	6
7.4. Field application of array measurement sensor.....	1	7	2
7.4.1. Field measurement method of array sensor	1	7	2
7.4.2. Field measurement result of array measure sensor	1	7	2
7.5. Concluison	1	7	6
Bibliography	1	7	7
Chapter 8. Conclusion	1	7	9

Appendix	1 8 3
A. Circuit diagram of measurement circuit.	1 8 3
B. Matlab code for sap flow conversion.....	1 8 4
C. Processing code for data acquisition.....	1 8 8
D. Arduino code for measurement.....	1 9 3
국문 초록	1 9 7

List of Figures

Chapter. 1

Figure 1-1. Simplified control diagram of greenhouse cultivation.	1
Figure 1-2. Example of feedback control in hydroponics.	2
Figure 1-3. SEM image of bacteria infected xylem. Leaf wither by bacterial infection.....	3
Figure 1-4. Flow of water and nutrient and fruit growth.....	3
Figure 1-5. Installation of T-max probe.	5
Figure 1-6. Installation of CHP method probe.	6
Figure 1-7. Installation of HR method probe.	7
Figure 1-8. Installation of HDM probe.	8
Figure 1-9. Optofluidic neural probe simultaneous drug delivery and photostimulation, Mouse with cannula implanted into dorsal striatum, connected to microinfusion pump.	1 0

Chapter. 2

Figure 2-1. HDM probe installed on a tree.	1 8
Figure 2-2. Sensor operation flow chart for sap flow measurement.	1 9
Figure 2-3. Schematic diagram of the method for measuring sap flow in a plant through heat dissipation of a single probe.....	2 2
Figure 2-4. Graph of temperature changes in heating and cooling cycles when there is no fluid flow in the conduit, and the flow is turned on.....	2 2
Figure 2-5. Schematic diagram and dimensions of microneedle probe for the sap flow measurement.	2 4
Figure 2-6. Fabrication process of microneedle sap flow sensor. Bottom dielectric deposition (a), electrode patterning (b) top dielectric deposition (c), bottom silicon deep etching (d), dielectric layer patterning (e), top silicon deep etching (f)...	2 8
Figure 2-7. Picture of fabricated microneedle sap flow sensor (a), Optical microscope image of needle tip (b).	2 9

Figure 2-8. SEM image of microneedle tip (a), and heater element (b).....	2 9
Figure 2-9. Assembled microneedle sensor. Single channel packaging board type A (a), Single channel packaging board type B (b), Packaging for multi-channel measurement (C), multi-channel measurement assembly (d).	3 0
Figure 2-10. Functional block diagram of measurement circuit.	3 2
Figure 2-11. Assembled measurement circuit. Circuit with 10-bit Atmega328 internal ADC (a). Circuit with 16-bit ADS1115 ADC (b).	3 3
Figure 2-12. Signal-to-noise test of measurement circuit with 10-bit ADC.....	3 4
Figure 2-13. Signal-to-noise test of measuring circuit with 16-bit ADC.	3 5
Figure 2-14. Electric breakdown by mechanical defect.	3 7
Figure 2-15. Electric breakdown by pinhole defect	3 7
Figure 2-16. FE-SEM image of the fabricated electrode with lift-off process (top view).....	3 8
Figure 2-17. SEM image of the fabricated electrode with lift-off process (side view).	3 9
Figure 2-18. Lift-off process flow with dielectric deposition in ideal case (a). Shear fracture and shear lip created during the non-ideal lift-off process (b).	3 9
Figure 2-19. Process flow of electrode patterning with dry etch process.	4 0
Figure 2-20. SEM image of the fabricated electrode with dry etch process. ...	4 0
Figure 2-21. Multilayer composite dielectric layer.	4 1
Figure 2-22. Microneedle probe operation in ionic solution. Oxidation from electrode in positive voltage driving (a). reduction from electrode in negative voltage driving (b).....	4 2
Figure 2-23. Optical microscope image of heating thermistor electrode after accelerated corrosion test. Electrode after 1 hour of operation at +10 V (a). Electrode after 24 hours of operation at -10 V (b).	4 3
Figure 2-24. Sap flow sensor installed on plant stem (a), Entire measurement system (b).....	4 4
Figure 2-25. Diagram of the entire measurement system.....	4 6

Chapter. 3

Figure 3-1. SEM image of the vascular bundle.....	5 1
Figure 3-2. Heat transfer modes in porous plant tissues, Cytoplasm and cell wall	5 2
Figure 3-3. Plot of convective heat dissipation and conductive heat dissipation, plot of heat dissipation ratio between conduction and convection.....	5 6
Figure 3-4. Simplified 2D single component heat transfer model.	5 7
Figure 3-5. Simplified 2D multi component heat transfer model	6 1
Figure 3-6. COMSOL simulation model. Full model image, image of heating thermistor in simulation	6 4
Figure 3-7. Temperature change of heating probe by flow speed from simulation.	6 5
Figure 3-8. Flow speed – exponential dissipation time constant plot from simulation.	6 7
Figure 3-9 . Obtained flow speed-temperature difference plot from simulation result and curve fitting based on Equation 3-36.....	6 8
Figure 3-10. Obtained flow index-flow speed plot from simulation result and curve fitting based on Equation 3-24.	6 9

Chapter. 4

Figure 4-1. Temperature graph of microneedle probe while heating.	7 5
Figure 4-2. Curve fitting result of the temperature change graph of the probe heated to 40 mW for 30 seconds.....	7 7
Figure 4-3. Steady state probe temperature according to heating power.	7 9
Figure 4-4. Change of time constant according to heating power.	7 9
Figure 4-5. Calibration setup for microneedle sap flow sensor to measure the flow in the test tube (a). Position of sap flow sensor probe for pipe flow calibration. Vertical cross section view (b). Horizontal cross section view (c).....	8 1
Figure 4-6. Temperature change of heating probe for pipe flow by the flow speed.	8 2

Figure 4-7. Flow speed – steady state heated temperature graph for pipe flow.	8 3
Figure 4-8. Flow speed–exponential dissipation time constant graph for pipe flow.	8 4
Figure 4-9. Relation between flow speed and temperature difference of probe (ΔT) in pipe flow.	8 5
Figure 4-10. Relation between flow index $\Delta T_M - \Delta T \Delta T$ and flow speed in pipe flow.	8 6
Figure 4-11. The response of microneedle sap flow sensor to the applied pipe flow speed.	8 7
Figure 4-12. Comparison between the applied water flow speed in pipe and measured flow speed from sap flow sensor.....	8 7
Figure 4-13. Calibration setup of microneedle sap flow sensor for xylem flow.	8 9
Figure 4-14. Cross section of tomato plant stem. The xylem is stained with crystal violet solution.	8 9
Figure 4-15. Temperature change of heating probe in xylem flow by flow speed.	9 0
Figure 4-16. Flow speed – steady state heated temperature for xylem flow..	9 1
Figure 4-17. Flow speed – exponential dissipation time constant plot for xylem flow.	9 2
Figure 4-18. Relationship between flow speed and temperature difference of probe (ΔT) in xylem flow.....	9 3
Figure 4-19. Relation between flow index $\Delta T_M - \Delta T \Delta T$ and flow speed in xylem flow.	9 4
Figure 4-20. Comparison between the applied water flow speed in xylem and measured flow speed from sap flow sensor.....	9 4

Chapter. 5

Figure 5-1. Experiment setup for artificial light illumination test.....	1 0 0
--	-------

Figure 5-2. Measured internal relative temperature of tomato stem during the artificial light illumination test.....	1	0	2
Figure 5-3. Measured sap flow of tomato stem during the artificial light illumination test.....	1	0	2
Figure 5-4. Picture inside the greenhouse at the Protected Horticulture Research Institute. Microneedle sap flow sensor installed on tomato plant stem.....	1	0	5
Figure 5-5. Sap flow speed of tomato stem during the long-term field measure test.....	1	0	8
Figure 5-6. Internal relative temperature of tomato stem during the long-term field measure test.....	1	0	8
Figure 5-7. Solar radiation intensity inside the greenhouse during the long-term field measure test.....	1	0	8
Figure 5-8. Ambient temperature inside the greenhouse during the long-term field measure test.....	1	0	9
Figure 5-9. Vapor pressure deficit inside the greenhouse during the long-term field measure test.....	1	0	9
Figure 5-10. Sap flow speed of tomato stem from Mar. 18th to Mar. 23rd..	1	1	0
Figure 5-11. Internal relative temperature of tomato stem from Mar. 18th to Mar. 23rd.....	1	1	0
Figure 5-12. Solar radiation intensity inside the greenhouse from Mar. 18th to Mar. 23rd.....	1	1	0
Figure 5-13. Ambient temperature inside the greenhouse from Mar. 18th to Mar. 23rd.....	1	1	0
Figure 5-14. Vapor pressure deficit inside the greenhouse from Mar. 18th to Mar. 23rd.....	1	1	1
Figure 5-15. Sap flow speed of tomato stem on May 20th.	1	1	2
Figure 5-16. Internal relative temperature of tomato stem on May 20th.	1	1	2
Figure 5-17. Solar radiation intensity inside the greenhouse on May 20th..	1	1	3
Figure 5-18. Ambient temperature inside the greenhouse on May 20th.	1	1	3
Figure 5-19. Vapor pressure deficit inside the greenhouse on May 20th.	1	1	3

Figure 5-20. Comparison between solar radiation and sap flow on May 20th.	1 1 4
Figure 5-21. Comparison between air temperature and sap flow on May 20th.	1 1 5
Figure 5-22. Comparison between vapor pressure deficit and sap flow on May 20th.	1 1 5
Figure 5-23. Comparison between solar radiation and sap flow from May 13th to May 26th.	1 1 6
Figure 5-24. Comparison between air temperature and sap flow from May 13th to May 26th.	1 1 7
Figure 5-25. Comparison between VPD and sap flow from May 13th to May 26th.	1 1 7
Figure 5-26. Sap flow and internal relative temperature of experimental group. The irrigation was cut on Oct. 1st.	1 1 9
Figure 5-27. Sap flow and internal relative temperature of control group... ..	1 1 9
Figure 5-28. Solar intensity inside the greenhouse during the experiment period.....	1 1 9
Figure 5-29. Air temperature inside the greenhouse during the experiment period.....	1 2 0
Figure 5-30. Comparison between daily watering and daily integrated solar radiation for experimental group.....	1 2 1
Figure 5-31. Comparison between daily watering and daily integrated solar radiation for control group.	1 2 1
Figure 5-32. Measured sap flow signal from 32 tomato plants.....	1 2 2
Figure 5-33. Average of 32 channels of sap flow signal.	1 2 3
Figure 5-34. Standard deviation of 32 channels of sap flow signal.	1 2 3
Figure 5-35. Coefficient of variation of 32 channels of sap flow signal.	1 2 3
Figure 5-36. Comparison between the sap flow signal of Ch.1 and the averaged sap flow signal.	1 2 4
Figure 5-37. Graph of the sap flow rate of Ch.1 divided by	

the average sap flow rate.....	1	2	4
Figure 5-38. Comparison between the sap flow signal of Ch.11 and the averaged sap flow signal.	1	2	5
Figure 5-39. Graph of the sap flow rate of Ch.11 divided by the average sap flow rate.	1	2	5
Figure 5-40. Bar graph of 32 channels of sap flow rate on Feb. 13th.....	1	2	6
Figure 5-41. Histogram of 32 channels of sap flow rate on Feb. 13th.....	1	2	7
Figure 5-42. Microneedle sap flow sensors installed on tomato peduncle and pedicel.	1	2	8
Figure 5-43. Sap flow rate of tomato peduncle.....	1	2	9
Figure 5-44. Internal relative temperature of tomato peduncle.....	1	2	9
Figure 5-45. Sap flow rate of tomato pedicel.....	1	2	9
Figure 5-46. Internal relative temperature of tomato pedicel.....	1	3	0
Figure 5-47. Experiment set up for in-vivo measurement of paprika . Microneedle sap flow sensor installed on paprika stem	1	3	2
Figure 5-48. Sap flow and internal relative temperature of paprika stem. ...	1	3	2
Figure 5-49. Experiment set up for in-vivo measurement of cucumber, Microneedle sap flow sensor installed on cucumber stem	1	3	3
Figure 5-50. Sap flow and internal relative temperature of cucumber stem.	1	3	3
Figure 5-51. Experiment set up for in-vivo measurement of clusia, Microneedle sap flow sensor installed on clusia stem.....	1	3	5
Figure 5-52. Sap flow and internal relative temperature of clusia stem. The daytime is marked with red box.....	1	3	5
Figure 5-53. Sap flow and internal relative temperature of clusia stem. The daytime is marked with red box.....	1	3	5
Figure 5-54. Comparison between C3, C4 and CAM photosynthesis mechanism.....	1	3	6
Figure 5-55. Experiment setup for in-vivo measurement of rubber tree. Microneedle sap flow sensor installed on rubber tree stem.	1	3	7
Figure 5-56. Sap flow and internal relative temperature of rubber tree stem	1	3	7

Figure 5-57. Surface of tomato stem after 37 days of measurement.....	1 3 9
Figure 5-58. Micro CT image of tomato stem with the trace of the microneedle sensor.	1 4 0

Chapter. 6

Figure 6-1. Temperature gradient monitored by infrared imagery.	1 4 4
Figure 6-2. Installation of reference probe for NTG compensation and compensation method.....	1 4 6
Figure 6-3. Experimental setup for NTG compensation.	1 4 8
Figure 6-4. Internal relative temperature during NTG compensation experiment.....	1 4 8
Figure 6-5. Temperature difference signal during NTG compensation experiment.....	1 4 9
Figure 6-6. Natural temperature gradient error during NTG compensation experiment.....	1 5 0
Figure 6-7. Compensated thermal dissipation signal during NTG compensation experiment.....	1 5 0
Figure 6-8. Measured sap flow rate without NTG compensation.	1 5 1
Figure 6-9. Measured sap flow rate with NTG compensation.	1 5 1

Chapter. 7

Figure 7-1. Cross-sectional image of a plant stem	1 5 5
Figure 7-2. Thermal simulation for silicon substrate microneedle.....	1 5 6
Figure 7-3. Blueprint of quartz microneedle probe sensor (a). Design scheme of quartz microneedle probe assembly (b). Magnified image of heating thermistor (c). Heat transfer simulation results (d).	1 5 8
Figure 7-4. Fabrication process of quartz microneedle probe. Substrate preparation (a). Electrode 1 patterning (b). Electrode 2 patterning (c). Dielectric layer deposition (d). Polymer layer deposition (e). Dicing (f).	1 5 9
Figure 7-5. Optical microscope image of quartz microneedle.	1 6 0

Figure 7-6. Temperature graph of microneedle probe while heating.	1 6 1
Figure 7-7. Steady state probe temperature according to heating power.	1 6 4
Figure 7-8. Change of time constant according to heating power.	1 6 5
Figure 7-9. Temperature change of heating probe in xylem flow by flow speed.	1 6 7
Figure 7-10. Flow speed – steady state heated temperature for xylem flow.	1 6 8
Figure 7-11. Flow speed–exponential dissipation time constant plot for xylem flow.	1 6 9
Figure 7-12. Relation between flow speed and temperature difference of probe (ΔT) in pipe flow.	1 7 0
Figure 7-13. Relation between flow index and flow speed in pipe flow.	1 7 1
Figure 7-14. Picture of array measure sensor. Array measure sensor installed in tomato plant stem.	1 7 2
Figure 7-15. Installation of array measurement sensor.	1 7 4
Figure 7-16. Sap flow measure result of array measure sensor.	1 7 4
Figure 7-17. Daily cumulative sap flow of array measure sensor.	1 7 4
Figure 7-18. Picture of plant stem cross section and installed sensor. Microscope image of plant tissue near the installed sensor.	1 7 5
Figure 7-19. Secondary growth in a plant stem.	1 7 5

List of Tables

Chapter. 2

Table 2-1. The maximum sap flow of plants.....	2	5
Table 2-2. The target performance of sap flow sensor.	2	6
Table 2-3. SNR and PSNR comparison between 10-bit and 16-bit circuit.	3	5
Table 2-4. Electric properties of measurement system.....	4	5
Table 2-5. Thermal properties of measurement system.....	4	5
Table 2-6. Performance of measurement system at $u=1$ mm/s.....	4	5

Chapter. 3

Table 3-1. curve fitting result of time-temperature graph of heat dissipating probe by flow speed from simulation and 3-component lumped capacitance model.	6	6
---	---	---

Chapter. 4

Table 4-1. Table of operating voltage, resolution, ADC value change, temperature change by the driving power of microneedle probe.	7	4
Table 4-2. Temperature change curve of probe according to heating power....	7	8
Table 4-3. Curve fitting result of time-temperature graph of heating probe in pipe flow by flow speed based on 3-component lumped capacitance model.	8	3
Table 4-4. Curve fitting result of time-temperature graph of heating probe in xylem flow by flow speed based on 3-component lumped capacitance model.	9	1

Chapter. 5

Table 5-1. List of field experiments of microneedle sap flow sensor for tomato plant.	1	0	6
Table 5-2. List of field experiments of microneedle sap flow sensor for other herbaceous plants.	1	3	1

Chapter. 7

Table 7-1. Comparison of material properties for substrate materials.	1 5 7
Table 7-2. Table of operating voltage, resolution, ADC value change, temperature change by the driving power of microneedle probe.	1 6 2
Table 7-3. Temperature change curve of probe according to heating power.	1 6 4
Table 7-4. Curve fitting result of time-temperature graph of heating probe in pipe flow by flow speed based on 3-component lumped capacitance model.	1 6 8

Chapter 1. General Introduction

1.1. Background of research

1.1.1. Importance of measuring biometric information in greenhouse cultivation

Proper environmental and irrigation control determines crop productivity and quality in greenhouse cultivation. A greenhouse can be modeled as a control system (Figure 1-1). In the control system, precise system status monitoring is required for better control result. In conventional agriculture, environmental variables such as temperature, humidity, and light intensity are monitored to determine the system status. However, these environmental variables reflect the status of crop indirectly. Therefore, a method for direct measurement of bio-signals of plants has been required.

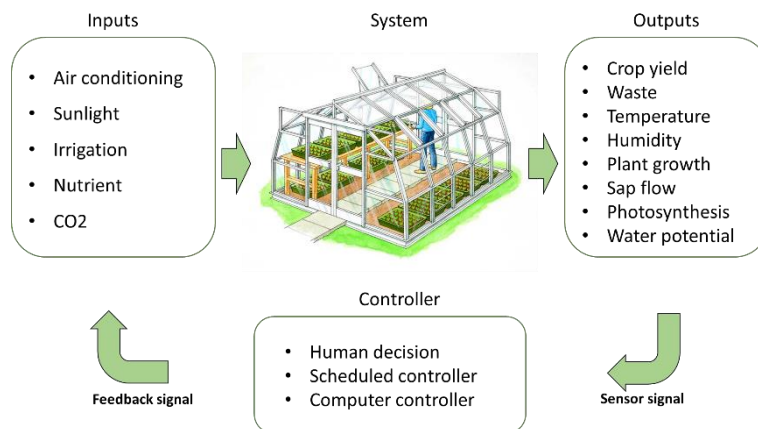


Figure 1-1. Simplified control diagram of greenhouse cultivation.

1.1.2. Importance of sap flow as biometric information

Water transport in plants is one of the best indicators of the plant status. The sap flow in plant stem is related to the amount of transpiration in leaves and water absorption in roots. The amount of water transpiration can be estimated from the sap flow in stem [1]. The water activity and photosynthesis of plant are closely related to transpiration. It is possible to monitor the supply and absorption of nutrient solution by measuring sap flow from the root of plants [2]. Figure 1-2 shows the application of sap flow measurement in hydroponics. The water status in hydroponics can be monitored, and the supply of water and nutrient can be regulated accordingly [3].

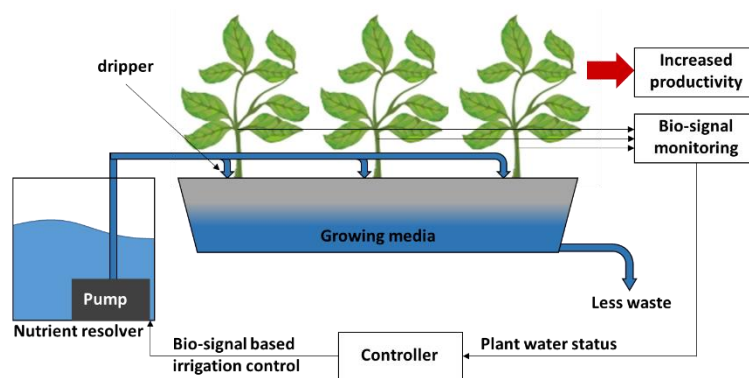


Figure 1-2. Example of feedback control in hydroponics.

The sap flow reflects the health and physiological state of a plant as well as the water status of the plant. When the plant suffers from infection such as bacteria wilt caused by *Erwinia tracheiphila*, bacteria proliferates in vascular bundle (Figure 1-3). In this case, sap flow is reduced even when the plant is well irrigated [4]. And the infection status of the plant can be monitored early on by measuring the sap flow and water potential.



Figure 1-3. SEM image of bacteria infected xylem (left) [5]. Leaf wither by bacterial infection (right) [6].

The flowering and hypertrophy of pulp is directly affected by the sap and nutrients flow in the peduncle and pedicel of the plant. The size of the fruit increases while the net flux from the plant stem to the fruit is positive. Sugar and nutrients flow into the fruit through the phloem, and the fruit matures [7, 8]. Therefore, the flow of sap in each part of the plant is a major physiological information representing fruit growth and reproduction.

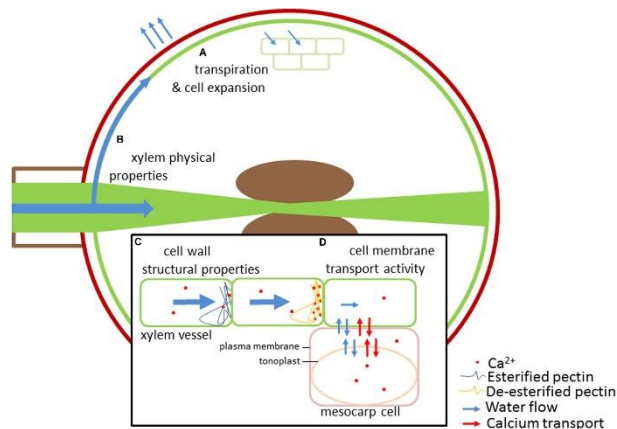


Figure 1-4. Flow of water and nutrient and fruit growth [9].

1.1.3. Thermometric sap flow measurement methods

There have been great demands for measuring the flow of sap to increase plant productivity and for physiological studies [10, 11]. Huber was the first to introduce heat as a tracer for estimating sap flow in plant stems in 1937 [12]. Marshall described the analytical background of heat transfer in sapwood and quantified heat velocity measurement [13]. Sakuratani measured the sap flow of soybean plants and sunflowers using the heat balance method with an external annular heater [14].

Various thermometric methods are available for measuring the sap flow. (i) T-max technology measures the flow by installing the heating probe and the temperature measurement probe on the plant stem in the direction of the fluid flow. This system generates a heat pulse in the heating probe and measures the taken time to reach the maximum temperature at the measurement probe [15]. (ii) A heater probe and two temperature probes are installed in the direction of the fluid flow in Compensation Heat Pulse (CHP) method. Each temperature probe is installed upstream and downstream of the heater probe, respectively. A heat pulse is generated by the heater probe, and the speed of heat pulse to the upper temperature probe and lower temperature probe is measured [16]. (iii) Heat Ratio (HR) method measures the flow rate by measuring the ratio of temperatures in the upper and lower probes a certain period after generating a heat pulse in the heater probe. The probes are installed in the same manner as the CHP method [13]. (iv) Heat Dissipation (HD) method measures the amount of heat dissipation by measuring the temperature of the heated probe. Heated probe temperature and unheated probe temperature are compared, and the amount of heat dissipation is

converted into sap flow [17].

The T-max method was proposed by Cohen. Two probes are installed on a plant stem in a radial direction (Figure 1-5). The distance between two probes is fixed. A heat pulse is generated in the upstream probe, and the time passed between the heat pulse generation and detection by the downstream probe is measured. The sap flow speed is calculated from the heat pulse travel time. Since the speed of the fluid flow is indirectly estimated in this method, conversion process is necessary. The relationship between the velocity of the heat pulse and the velocity of the liquid flow depends on the thermal properties of the medium:

$$v_h = \frac{\sqrt{x^2 + 4kt_m}}{t_m} \quad (1-1)$$

where, v_h is heat velocity, x is distance between two probes, k is thermal diffusivity, t_m is time to reach the maximum temperature.



Figure 1-5. Installation of T-max probe [18].

For CHP method, two temperature sensor probes are installed radially along the flow direction. A heater element is inserted between the upstream sensor probe and downstream sensor probe at a fixed distance. During the measurement, the heating element is heated with a pulse and convective heat transfer occurs. The heat pulse is measured at both upstream and downstream probes. The time until arrival of heat pulse depends on the flow rate and is used to calculate heat pulse velocity (v_h):

$$v_h = \frac{x_1 + x_2}{2t_0} \cdot 3600 \quad (1-2)$$

where v_h is heat velocity, x_1 is distance to downstream probe, x_2 is distance to upstream probe, t_0 is time when two probes are at the same temperature after the heat pulse generation.



Figure 1-6. Installation of CHP method probe [19].

HR method consists of a heating element and two temperature sensors spaced equidistantly above and below the heater along the flow direction. For

measurement, a pulse of heat is applied, and the upstream and downstream temperatures are measured 60 to 100 seconds after the heat pulse. The ratio of the upstream and downstream temperature rises is calculated and converted into the heat velocity:

$$v_h = \frac{k}{x} \ln \left(\frac{\Delta T_d}{\Delta T_u} \right) \quad (1-3)$$

where v_h is heat velocity, k is thermal diffusivity, x is distance to temperature probe, ΔT_d is temperature rise in the downstream probe, and ΔT_u is temperature rise in the upstream probe.



Figure 1-7. Installation of HR method probe [20].

Heat dissipation method was introduced by Grainer, A. [17]. The HD sap flow measurement setup consists of two probes, which are vertically aligned and radially inserted into the sapwood. The upstream probe has copper-constantan thermocouple and measures unheated temperature. The downstream probe is inserted 10 cm above the upstream probe. The downstream probe has coiled metal wire. A constant voltage is applied to the wire which is heated by Joule effect. The

temperature difference between heated probe and unheated probe is influenced by the convective and conductive heat dissipation from the probe. Granier derived empirical relationship between sap flux density and temperature difference:

$$u = a \cdot \left(\frac{\Delta T_M - \Delta T}{\Delta T} \right)^b \quad (1-4)$$

where u ($\text{m}^3/\text{m}^2\text{s}$) is the sap flux density, ΔT (K) is the temperature difference between two probes, ΔT_M (K) is the temperature difference obtained at zero flow, a and b is empirical constant based on experimental regression.

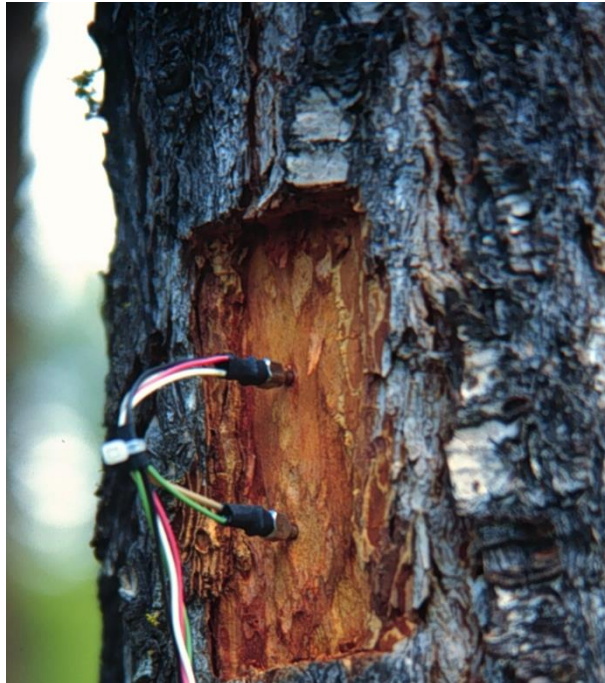


Figure 1-8. Installation of HDM probe [21].

1.1.4. Demand for minimally invasive measurements

However, existing measurement methods for sap flow in plants require invasive or large and complicated measurement setups limiting their application. With conventional sap flow measuring methods, sapwood needs to be drilled, and two or more rigid cylindrical probes are inserted into the sapwood. For example, the usual dimensions of Grainer's probe are 2 mm in diameter and 20 mm or more in length, and may lead to the invasion of xylem and the disturbance of water transportation [22]. This wounding effect can hinder accurate measurement, and sometimes severely interfere with plant growth. This issue becomes more pronounced in soft and small plants typically grown in horticultural hydroponics. Tomatoes and bell peppers are, for example, about 1 cm in stem diameter and can hardly withstand the macroscale probes. More importantly, probes are heated 8-10°C above the surroundings that will obviously disturb plant growth [23]. This physical and thermal invasiveness limits the use of typical HDM for greenhouse plants. A minimally invasive method is required for measuring sap flow of small plants.

1.1.5. MEMS implantable microneedle sensors

Microelectromechanical systems (MEMS) implantable devices have been proven useful in minimally invasive applications in medical science [24]. Various implantable systems for in-vivo applications include implantable biosensor [25], drug delivery [26], and microhypodermic needle [27]. Especially, as an application of microneedle probe, neuroprobes are fabricated with silicon microfabrication

technique [28] and used for brain signal monitoring [29], optogenetic study [30], and drug delivery [31]. These microneedle-based probes enabled neuroscience study of living animals with minimal invasion. Thus, application of microneedle-based probes can be used to measure plant physiological information in a minimally invasive manner. For botanic application of microneedle probes, Jeon reported measurement of electrical conductivity of tomato plant [32].

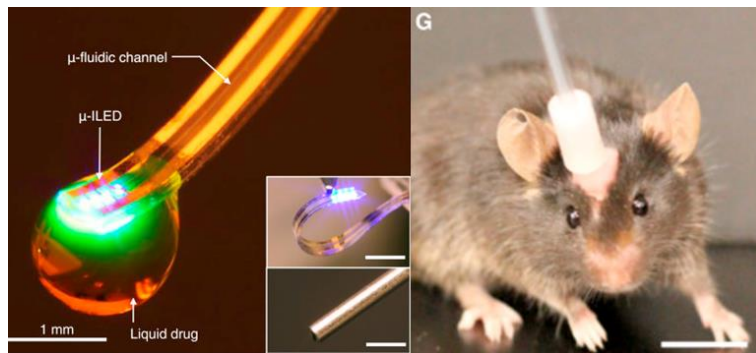


Figure 1-9. Optofluidic neural probe simultaneous drug delivery and photostimulation (left). Mouse with cannula implanted into dorsal striatum, connected to microinfusion pump (right) [33].

1.1.6. Benefits of microscale needle probe in thermal characteristic aspects

Small-scale physics reveals the fundamental benefit of a microneedle thermal probes owing to their size and heat transfer characteristics. The heat capacity of the microscale system is reduced due to its small control volume and mass. Thus the thermal response is quicker and more sensitive in the microscale system [34]. These characteristics would enable rapid thermal measurement reaching to thermal equilibrium with less amount of energy and time. Most importantly, the target temperature rise of the microneedle probe can be substantially lowered.

1.2. Research objective

In this research, a microneedle probe sap flow sensor that can measure sap flow inside plant in a minimally invasive way is presented. Sap flow and internal relative temperature were measured with the sensor. The microneedle probe fabricated with MEMS fabrication process can minimize invasion to plant and wound effect. Robust and reliable measurement is possible with single probe measurement setup. During the course of the research, the design and thermal analysis of the microneedle are performed. Thermal analysis is performed through simulation and experiment. The sensor is fabricated with MEMS fabrication process. A circuit system for measurement and data acquisition is built. Calibration of the sensor and in-vivo measurement in the field environment are performed.

Bibliography

- [1] A. Granier, "Evaluation of transpiration in a Douglas-fir stand by means of sap flow measurements," *Tree physiology*, vol. 3, no. 4, pp. 309-320, 1987.
- [2] P. González-Altozano et al., "Comparative assessment of five methods of determining sap flow in peach trees," *Agricultural Water Management*, vol. 95, no. 5, pp. 503-515, 2008.
- [3] J. Fernández, S. Green, H. Caspari, A. Diaz-Espejo, and M. Cuevas, "The use of sap flow measurements for scheduling irrigation in olive, apple and Asian pear trees and in grapevines," *Plant and Soil*, vol. 305, no. 1-2, pp. 91-104, 2008.
- [4] K. Yadeta and B. Thomma, "The xylem as battleground for plant hosts and vascular wilt pathogens," (in English), *Frontiers in Plant Science*, Review vol. 4, no. 97, 2013.
- [5] *Xylella fastidiosa* pv *oleander* within xylem vessel of an oleander leaf.
Available from: <http://www.genomenetwork.org>
- [6] A. Gould and J. Lashomb, "Bacterial leaf scorch (BLS) of shade trees," *The Plant Health Instructor*, 2007.
- [7] T. Knipfer, J. Fei, G. A. Gambetta, A. J. McElrone, K. A. Shackel, and M. A. Matthews, "Water Transport Properties of the Grape Pedicel during Fruit Development: Insights into Xylem Anatomy and Function Using Microtomography," *Plant Physiology*, 10.1104/pp.15.00031 vol. 168, no. 4, p. 1590, 2015.
- [8] R. W. Johnson, M. A. Dixon, and D. R. Lee, "Water relations of the tomato during fruit growth," *Plant, Cell & Environment*, vol. 15, no. 8, pp. 947-953,

1992.

- [9] B. Hocking, S. D. Tyerman, R. A. Burton, and M. Gilliam, "Fruit calcium: transport and physiology," *Frontiers in plant science*, vol. 7, p. 569, 2016.
- [10] M. J. Clearwater, Z. Luo, M. Mazzeo, and B. Dichio, "An external heat pulse method for measurement of sap flow through fruit pedicels, leaf petioles and other small-diameter stems," *Plant, Cell & Environment*, vol. 32, no. 12, pp. 1652-1663, 2009.
- [11] C. W. Windt, E. Gerkema, and H. Van As, "Most Water in the Tomato Truss Is Imported through the Xylem, Not the Phloem: A Nuclear Magnetic Resonance Flow Imaging Study," *Plant Physiology*, vol. 151, no. 2, pp. 830-842, 2009.
- [12] E. S. Bruno Huber, "Eine Kompensationsmethode zur thermoelektrischen Messung langsamer Saftströme," *Berichte der Deutschen Botanischen Gesellschaft*, vol. 55, no. 9, pp. 514-529, 1937.
- [13] D. C. Marshall, "Measurement of Sap Flow in Conifers by Heat Transport," *Plant Physiology*, vol. 33, no. 6, pp. 385-396, 1958.
- [14] T. Sakuratani, "A Heat Balance Method for Measuring Water Flux in the Stem of Intact Plants," *Journal of Agricultural Meteorology*, vol. 37, no. 1, pp. 9-17, 1981.
- [15] Y. Cohen, M. Fuchs, and G. Green, "Improvement of the heat pulse method for determining sap flow in trees," *Plant, Cell & Environment*, vol. 4, no. 5, pp. 391-397, 1981.
- [16] R. Closs, "The heat pulse method for measuring rate of sap flow in a plant stem," *NZJ Sci.*, vol. 1, pp. 281-288, 1958.
- [17] A. Granier, "Une nouvelle méthode pour la mesure du flux de sève brute dans

le tronc des arbres," *Ann. For. Sci.*, 10.1051/forest:19850204 vol. 42, no. 2, pp. 193-200, 1985.

- [18] T-max probe. Available from: <http://au.ictinternational.com>
- [19] D. McJannet and P. Fitch, *A Flexible and Easily Constructed Heat Pulse System for Monitoring Sapflow in Trees*. Citeseer, 2004.
- [20] HRM sensor. Available from: <http://www.edaphic.com.au>
- [21] HDM sensor. Available from: <https://www.for.gov.bc.ca>
- [22] S. S. Burgess et al., "An improved heat pulse method to measure low and reverse rates of sap flow in woody plants," *Tree Physiology*, vol. 21, no. 9, pp. 589-598, 2001.
- [23] M. Hasanuzzaman, K. Nahar, M. M. Alam, R. Roychowdhury, and M. Fujita, "Physiological, Biochemical, and Molecular Mechanisms of Heat Stress Tolerance in Plants," *International Journal of Molecular Sciences*, vol. 14, no. 5, pp. 9643-9684, 2013.
- [24] A. R. Grayson et al., "A BioMEMS review: MEMS technology for physiologically integrated devices," *Proceedings of the IEEE*, vol. 92, no. 1, pp. 6-21, 2004.
- [25] S. A. Grant, K. Bettencourt, P. Krulevitch, J. Hamilton, and R. Glass, "In vitro and in vivo measurements of fiber optic and electrochemical sensors to monitor brain tissue pH," *Sensors and Actuators B: Chemical*, vol. 72, no. 2, pp. 174-179, 2001.
- [26] J. T. Santini, M. J. Cima, and R. Langer, "A controlled-release microchip," *Nature*, vol. 397, no. 6717, pp. 335-338, 1999.
- [27] D. V. McAllister, M. G. Allen, and M. R. Prausnitz, "Microfabricated microneedles for gene and drug delivery," *Annual Review of Biomedical*

Engineering, vol. 2, no. 1, pp. 289-313, 2000.

- [28] P. K. Campbell, K. E. Jones, R. J. Huber, K. W. Horch, and R. A. Normann, "A silicon-based, three-dimensional neural interface: manufacturing processes for an intracortical electrode array," *IEEE Transactions on Biomedical Engineering*, vol. 38, no. 8, pp. 758-768, 1991.
- [29] G. T. Kovacs et al., "Silicon-substrate microelectrode arrays for parallel recording of neural activity in peripheral and cranial nerves," *IEEE Transactions on Biomedical Engineering*, vol. 41, no. 6, pp. 567-577, 1994.
- [30] S. Royer, B. V. Zemelman, M. Barbic, A. Losonczy, G. Buzsáki, and J. C. Magee, "Multi-array silicon probes with integrated optical fibers: light-assisted perturbation and recording of local neural circuits in the behaving animal," *European Journal of Neuroscience*, vol. 31, no. 12, pp. 2279-2291, 2010.
- [31] J. Chen, K. D. Wise, J. F. Hetke, and S. Bledsoe, "A multichannel neural probe for selective chemical delivery at the cellular level," *IEEE Transactions on Biomedical Engineering*, vol. 44, no. 8, pp. 760-769, 1997.
- [32] E. Jeon, S. Choi, K.-H. Yeo, K. S. Park, M. L. Rathod, and J. Lee, "Development of electrical conductivity measurement technology for key plant physiological information using microneedle sensor," *Journal of Micromechanics and Microengineering*, vol. 27, no. 8, p. 085009, 2017.
- [33] J.-W. Jeong et al., "Wireless optofluidic systems for programmable in vivo pharmacology and optogenetics," *Cell*, vol. 162, no. 3, pp. 662-674, 2015.
- [34] Y. Xuan and W. Roetzel, "Conceptions for heat transfer correlation of nanofluids," *International Journal of heat and Mass transfer*, vol. 43, no. 19, pp. 3701-3707, 2000.

Chapter 2. Methods, Design and Fabrication

2.1. Design of microneedle sap flow sensor probe

2.1.1. Sap flow measurement with heat dissipation method

The heat dissipation method (HDM) for sap flow measurement was introduced by Grainer, A. [1]. The HDM setup consists of two probes that are vertically aligned and radially inserted into the sapwood. The upstream probe has copper-constantan thermocouple and measures unheated temperature. The downstream probe has a coil metal heater and is inserted 10 cm above the upstream probe. Constant power is applied to the wire which is then heated by the Joule effect during which the heated temperature is measured. The temperature difference between the heated probe and the unheated probe is influenced by convective and conductive heat dissipation from the probes. Granier derived an empirical relationship between sap flux density (flow speed) and temperature difference as follows which can also be derived from the King's law for hot wire anemometry [2]:

$$u = a \cdot \left(\frac{\Delta T_M - \Delta T}{\Delta T} \right)^b, \quad (2-1)$$

where u ($\text{m}^3/\text{m}^2\text{s}$) is the sap flux density, ΔT (K) is the temperature difference between the two probes. ΔT_M (K) is the temperature difference obtained when there is no sap flow. 'a' and 'b' are empirical constants based on experimental

regression. It should be emphasized that Granier claimed that these empirical constants are invariant regardless of the type of tree [1]. Total sap flow F (m^3/s) is calculated as:

$$F = u \cdot S_a, \quad (2-2)$$

where S_a (m^2) is the cross-sectional area of the sapwood.



Figure 2-1. HDM probe installed on a tree [3].

2.1.2. Sap flow measurement method with a single thermal probe

Granier's heat HDM has been widely used for tree physiology and hydrologic research due to its simplicity, high degree of accuracy, reliability, and relatively

low cost [4]. However, in order to measure sap flow with HDM, both the heating probe temperature and the unheated probe temperature must be measured. The tree has to be drilled and two or more probes should be installed, which increases invasion to the plant. In addition, since the probe continuously emits heat, it consumes more power and increases thermal damage to the plant. A measurement method using a single probe has been devised for simple and robust setup with minimized invasion on the plant.

In this research, the heated and unheated probe temperatures were measured by turning on and off the power of one probe instead of installing two probes. By measuring sap flow with a single probe, the invasion to plant was minimized. Also power consumption was reduced as the power was turned off for part of the measurement time, which further minimized thermal invasion to plant.

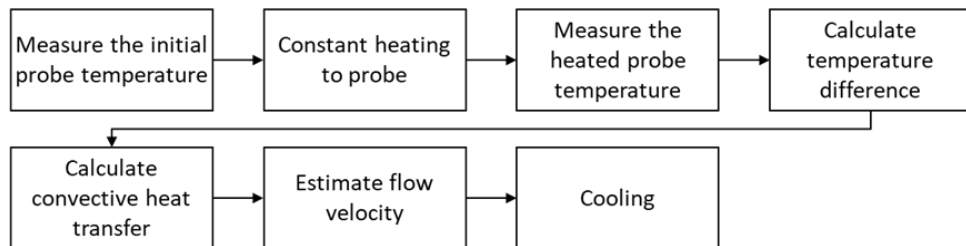


Figure 2-2. Sensor operation flow chart for sap flow measurement.

The following is the measurement procedure:

- (i) A temperature probe measures the internal temperature of the plant in an unheated state.
- (ii) The probe is heated at a constant power.
- (iii) After a certain period of heating, the probe reaches thermal equilibrium

state, and the heated probe temperature is measured.

- (iv) Calculate the temperature difference between the heated and unheated probe.
- (v) Calculate convective heat transfer.
- (vi) Estimate the flow rate from the calculated convective heat transfer.
- (vii) The power to the probe is cut off and the probe is cooled to reach equilibrium with the surroundings for the next measurement.

2.1.3. Determination of T_M

Maximum temperature difference (T_M) is required to obtain the sap flow rate using heat dissipation method. As shown in equation 2-1, the calculated sap flow is dependent on T_M value. T_M occurs at zero flow state. Generally, it is assumed that there is no sap flow during the night because the stomata of a plant are closed and evaporation is minimized. Therefore, the largest ΔT value occurs during the night, and is selected as T_M . Using this method T_M value is updated on a daily basis [1].

However, under certain conditions, sap flow continues during the night [5, 6]. This nocturnal sap flow makes T_M to be underestimated. Underestimation of T_M results in sap flow to be underestimated. Also, by assuming sap flow during the night to be zero, nocturnal sap flow, which is one of the important plant physiological information, comes unavailable. To increase the accuracy of sap flow measurement and to measure the nocturnal sap flow, more reliable T_M determination method is required.

The simplest way to determine the T_M value is the absolute maximum method,

which determines the point at which the largest ΔT is measured over the entire measurement period. This method is relatively accurate when the measurement period is short, but when the measurement period is long, it has a disadvantage that it does not reflect physiological changes in the plant such as the plant growth or the annual cycle.

The next T_M determination method is a daily maximum method in which the T_M of the day is used for that day only. This method is accurate when the diurnal temperature difference is large and the difference of sap flow rate during the daytime and the nighttime is large. However, if hot and dry climate continues during the night time and nocturnal sap flow occurs, the measurement becomes inaccurate.

The moving window method is a compromise between the above two methods. In this method, T_M is determined in dynamic time windows. Within these time windows, the maximum ΔT value within the window is assumed to be T_M value. The length of the moving window can vary from 3 to 15 days. The advantage of moving window method is that it is easy to implement and, due to its dynamic character, capable of compensating for drifts in the data [7].

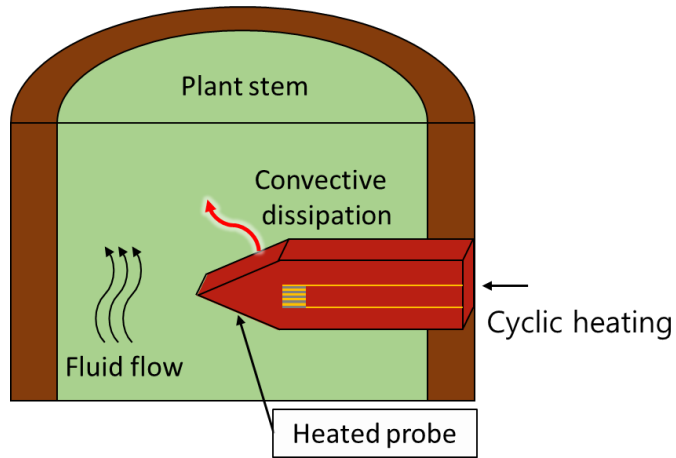


Figure 2-3. Schematic diagram of the method for measuring sap flow in a plant through heat dissipation of a single probe.

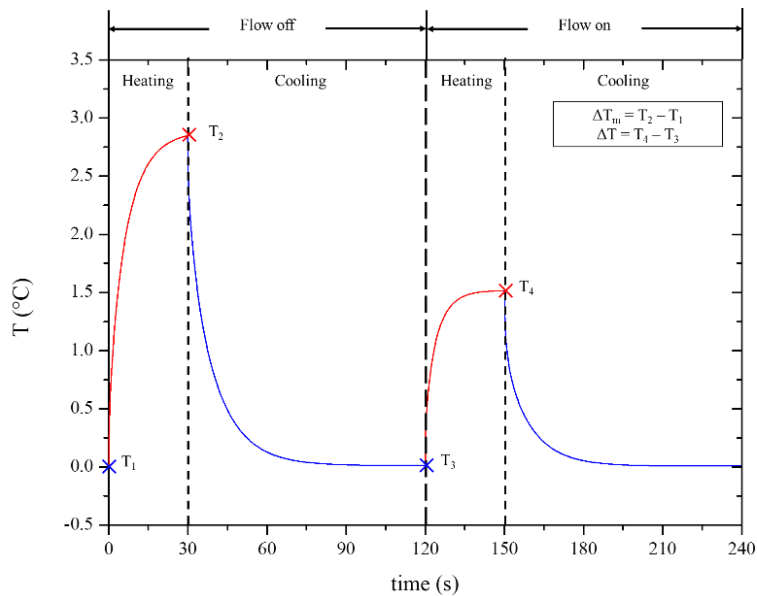


Figure 2-4. Graph of temperature changes in heating and cooling cycles when there is no fluid flow in the conduit (left), and the flow is turned on (right).

2.1.4. Thermal design of microneedle probe

Figure 2-3 shows a single microneedle probe for sap flow measurement. The measurement is based on the HDM principle which was modified to use the single probe configuration. The original HDM measures the temperature difference between two probes, i.e., heated and unheated ones, to correlate the heat dissipation and the flow speed. The heated probe continuously dissipates heat and the temperature values are measured at both probes when a thermal equilibrium is reached. In our approach, on the other hand, the functions of the two probes should be implemented in a single hot wire on a single probe to allow for simple configuration and small form factor. In order to use the single hot wire as both the heated and the unheated probes, the heated and unheated temperatures are measured in sequence. The temperature value is measured by using the metal wiring pattern as the heating element and the temperature sensor simultaneously. For example, a gold wire pattern can be used as a sensor whose temperature coefficient of resistance is 0.0034 K^{-1} .

Figure 2-4 shows the heating cycle in a real test without and with the water flow in a silicone tube. The unheated temperature (T_1) of the probe is measured first, followed by the heated temperature (T_2) after 30 seconds. As shown in Figure 2-4, the heated temperature could not reach the equilibrium temperature. The longer the heating time, the closer it gets to the thermal equilibrium temperature. However, the temperature rise during the 30 seconds of heating was sufficient to distinguish it from other flow rates. The heating time of 30 seconds was used as a compromise between accurate temperature measurement and short measurement interval. This heating period is necessary to reach a quasi-equilibrium state after

heating starts. This measurement will produce $\Delta T_M = T_2 - T_1$ in equation 2-1, the temperature difference when there is no flow. Then the heater is switched off and cooled for a sufficient time, i.e., 90 seconds before the next measurement. Thus, the measurement interval of each cycle is 120 seconds. The same cycle is applied when there is a flow to obtain $\Delta T = T_4 - T_3$ which is lower than ΔT_M because of the flow convection that removes heat from the surface.

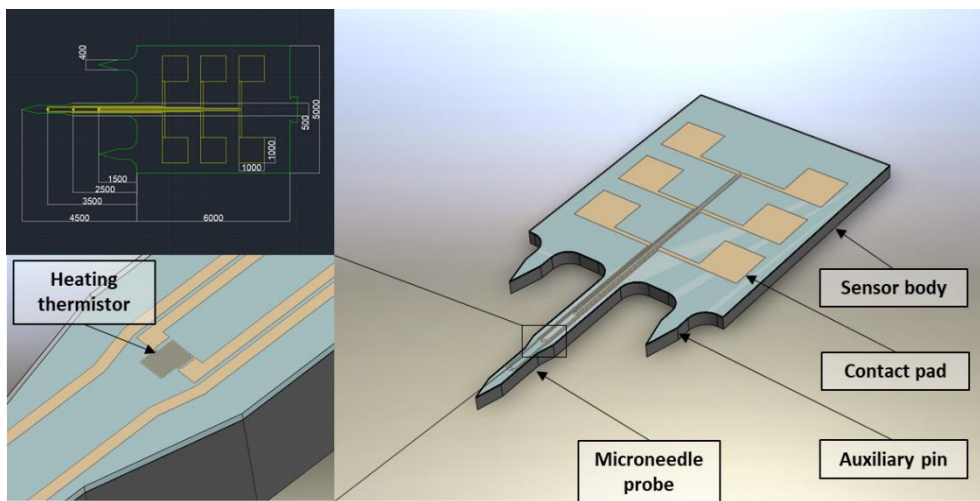


Figure 2-5. Schematic diagram and dimensions of microneedle probe for the sap flow measurement.

2.1.5. Structural design of microneedle probe

Figure 2-5 shows the schematic diagram of a microneedle probe for the sap flow measurement in the stem of a greenhouse plant. The sensor consists of a sensing probe, two auxiliary needles, and contact pads. The sensing probe with multiple heaters (i.e. hot wires) is designed to access the plant xylem. The overall dimensions of the current sensing probe are 5-mm long, 500- μm wide, and 300-

μm thick. The probe tip is sharp enough to penetrate the cortex of the plant stem. The taper angle is 30°, and the tip radius is few micrometers. Three heater patterns are placed on the probe in an array, 1.5, 2.5, 3.5 mm offset from the foot, respectively. Each heater pattern, 300 Ω in resistance, is operated independently, and can be considered as a single hot wire. Two short auxiliary needles grasp the plant skin, and ensure the whole body is firmly attached. The body and the contact pad of the sensor are packaged with a PCB board for signaling and power connections.

2.1.6. Target performance of the sensor

The target performance and design goals of the sensor are presented. First, the measurement flow speed range of the sensor is determined. The maximum ranges of sap flow measured in the previous studies are shown in Table 2-1.

Table 2-1. The maximum sap flow of plants.

Plant species	Measure method	Maximum sap flow speed (mm/s)	Reference
Maple tree	Heat ratio	0.056	[8]
Olive tree	Thermal dissipation	0.083	[9]
American beech tree	Heat field deformation	0.222	[10]

The literatures have confirmed that the sap flow rate does not exceed 0.25 mm/s in most plants. The target measurement range was obtained by multiplying a safety factor of 4 to the maximum sap flow speed from literatures. The target

error range of measurement was set to less than 5% of signal. Thus the target signal to noise ratio (SNR) was above 20. For example, when the measured flow speed is 1 mm/s, the acceptable error of the measurement is below 50 $\mu\text{m/s}$. The measurement range was divided into about 500 steps, and the flow speed resolution was set to 2 $\mu\text{m/s}$. The target measurement performance is shown in the Table 2-2.

Table 2-2. The target performance of sap flow sensor.

Range (mm/s)	Resolution ($\mu\text{m/s}$)	Signal to noise ratio	RMS error ($\mu\text{m/s}$)
0 ~ 1	< 2	> 20	< 50 (at u= 1 mm/s)

2.2. Fabrication of microneedle sap flow sensor

2.2.1. Fabrication process of microneedle sensor

Both surface micromachining and bulk micromachining technology were used for fabrication of microneedle sensor. The fabrication was performed in Inter-University Semiconductor Research Center, Seoul National University, and Korea Advanced Nano Fab Center. Figure 2-6 shows the fabrication process of the microneedle sap flow sensor. P-type silicon, 500- μm thick, 4-inch double side polished (100) wafers were used for substrate (WRS materials). The wafers were prepared with piranha cleaning. 1 μm of silicon oxide film was deposited as a bottom insulation layer with TEOS CVD (P-5000, Applied Material Korea) process (Figure 2-6. (a)). 4000 \AA titanium and 2000 \AA gold layers were deposited with e-gun evaporation (ZZS550-2/D, MAESTECH) method, and patterned with photolithography (MA-6, Karl-suss) and inductive coupled plasma (PlasmaPro ICP System100 Cobra, Oxford instruments) etching process (Figure 2-6. (b)). 3 layers of 2000 \AA silicon nitride film (Ni) and 2 layers of 2000 \AA silicon oxide film (Ox) were alternately deposited (Ni-Ox-Ni-Ox-Ni) as a top insulation layer with a plasma enhanced chemical vapor deposition (VL-LA-PECVD, Unaxis) (Figure 2-6. (c)). 5000 \AA of aluminum masking layer was deposited with sputtering (SRN 120, Sorona) and patterned with wet etching (80wt% phosphoric acid, 5wt% nitric acid, 5wt% acetic acid, and 10wt% deionized water) on backside of wafer. 200 μm of silicon was etched using deep reactive ion etching (DRIE, SLR-770-10R, PLASMA-THERM DRIE) from the back leaving 300 μm of microneedle layer (Figure 2-6. (d)). The pads for electrical connection were opened, and the masking

layer for silicon etching was patterned with the ICP etching process (Figure 2-6. (e)). The rest of silicon substrate was etched and needle structure was formed using DRIE (SLR-770-10R, PLASMA-THERM DRIE) process (Figure 2-6. (f)). After the silicon deep etching process, photoresist masking layer was removed and 100 Å fluorocarbon polymer layer was deposited as a hydrophobic layer (SLR-770-10R, PLASMA-THERM DRIE). Each sensor was detached from the silicon substrate, ready to be assembled (Figure 2-7). 40 sensors were manufactured in a 4-inch wafer. The yield was 95% or more. The main cause of the failure was the mechanical breakage of the sensor during the DRIE process. Due to the small size of features produced by bulk micromachining, stress concentration is likely to occur so that it was easy to break along the single crystal silicon substrate.

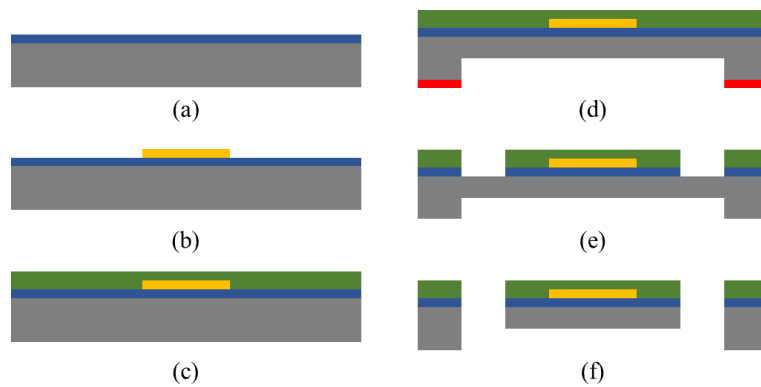


Figure 2-6. Fabrication process of microneedle sap flow sensor. Bottom dielectric deposition (a), electrode patterning (b) top dielectric deposition (c), bottom silicon deep etching (d), dielectric layer patterning (e), top silicon deep etching (f).

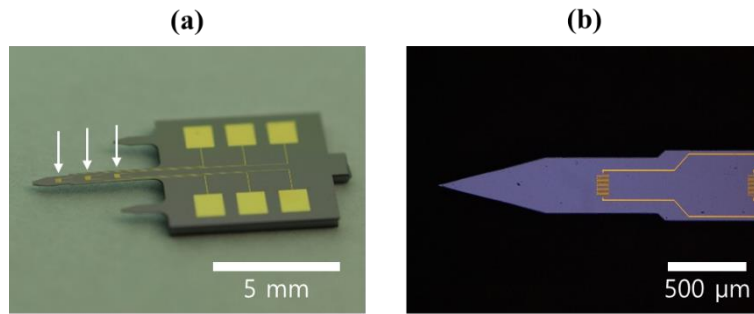


Figure 2-7. Picture of fabricated microneedle sap flow sensor (a), Optical microscope image of needle tip (b).

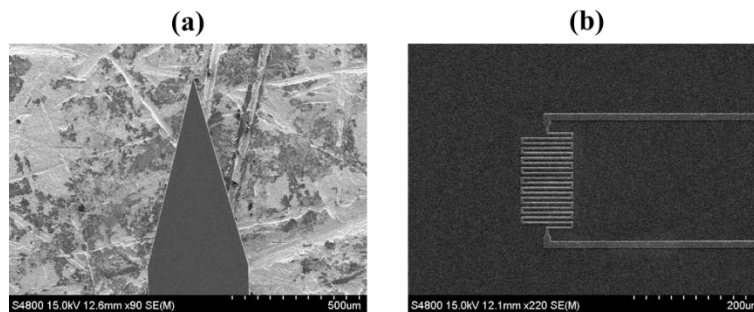


Figure 2-8. SEM image of microneedle tip (a), and heater element (b).

2.2.2. Packaging of the sensor

Packaging of the microneedle sensor was required to protect the sensor from the environment. Sensor packaging consists of a PCB board, wire bonding, and connectors. Small packaging size is preferred to avoid the mechanical breakage. Two kinds of packaging boards were designed for single channel measurement. Figure 2-9 (a) shows ‘A’ type packaging board (10*10 mm) and Figure 2-9 (b) shows ‘B’ type packaging board (7*15 mm). The electrode pads of the device and the PCB are electrically connected via wire bonding. 0.1-mil (25.4-μm) gold wire

was used. IPEX format connectors were used for small size and easy assembly. Packaging board for multiple channel measurement setup was also designed (Figure 2-9 (c, d)). In order to address all three sensing elements, six analog output terminals should be connected to the packaging board. Flexible printed circuit (FPC) connector was used as a flexible multiple channel cable. The entire packaging consists of a sensor packaging board, an FPC connector, an FPC-to-coax conversion board, and a coaxial cable.

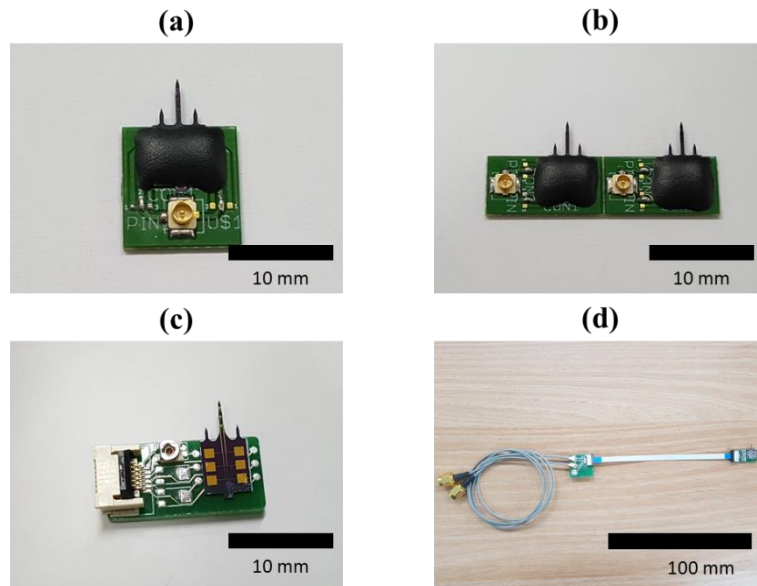


Figure 2-9. Assembled microneedle sensor. Single channel packaging board type A (a), Single channel packaging board type B (b), Packaging for multi-channel measurement (C), multi-channel measurement assembly (d).

2.3. Measurement circuit design and fabrication

2.3.1. Design of measurement circuit

The circuit for measuring the microneedle sap flow sensor signal was designed. Precise measurement of the temperature change is important because the sensor measures the sap flow rate based on the temperature signal. The functional block diagram of the circuit designed for precise measurement is as Figure 2-10. The power applied to the sensor is controlled through the microcontroller unit (MCU). Heat is generated while power is applied to the sensor. As the temperature of the sensor increases, the resistance value of the sensor increases proportional to the temperature change. Using the Wheatstone bridge circuit, the change in resistance of the sensor is converted to an analog voltage signal. The differential amplifier removes the bias from the analog signal and amplifies the signal. The multiple sensor signals are measured simultaneously by the multiplexer. The analog signal is converted with an analog-to-digital converter (ADC) to a digital signal. The digital signal is transmitted to the MCU and transmitted to the PC via serial communication.

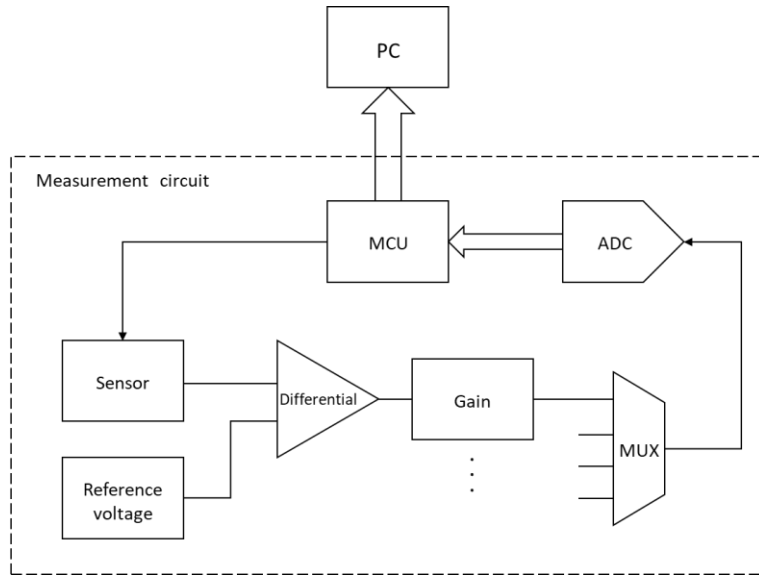


Figure 2-10. Functional block diagram of measurement circuit.

2.3.2. Fabrication of the measurement circuit

Based on the measurement circuit design, the actual measurement circuit was fabricated and evaluated. The microcontroller used was Atmega 328 (Atmel). The IRFZ44N power MOSFET (International Rectifier) was used to control the power applied to the sensor. The AD620ARZ (Analog Devices) was used as a differential amplifier. Atmega328 built-in 10-bit ADC was used for the analog-to-digital conversion. A 15 V constant voltage power supply was used to power the measurement circuit. RG-316 coaxial cable and IPEX / SMA connector were used to receive analog sensor signals (Figure 2-11 (a)).

Also, to improve the existing measurement circuit, a circuit using an ADC with higher resolution was fabricated. The basic circuit configuration was the same, but 16-bit ADS1115IDGS (Texas Instruments), a higher resolution ADC, was used instead of the previous Atmega 328 internal 10-bit ADC. In addition, to improve

input power quality, the LT3092EST (Linear Technology) power regulator was used (Figure 2-11 (b)).

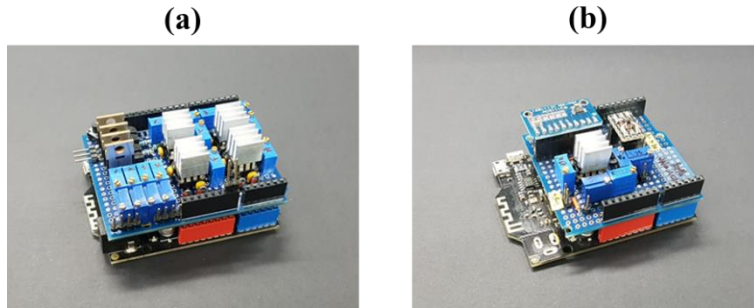


Figure 2-11. Assembled measurement circuit. Circuit with 10-bit Atmega328 internal ADC (a). Circuit with 16-bit ADS1115 ADC (b).

2.3.3. Evaluatoin of measurement system.

The performance of the fabricated 10-bit ADC measurement circuit was evaluated. A precision resistor was connected to the measurement circuit, and the signal value was measured while maintaining a constant temperature. The signal-to-noise ratio of the sensor was measured using the deviation value from 5000 samples (Figure 2-12). The peak signal to noise ratio (PSNR), and signal to noise ratio (SNR) were measured by the following equations:

$$\text{PSNR} = 10 \log_{10} \left(\frac{\text{MAX}_I^2}{\text{MSE}} \right) = 20 \log_{10} \left(\frac{\text{MAX}_I}{\sqrt{\text{MSE}}} \right) \quad (2-3)$$

$$\text{SNR} = \frac{P_{\text{signal}}}{P_{\text{noise}}} \text{ or } \text{SNR}_{\text{db}} = 20 \log_{10} \left(\frac{P_{\text{signal}}}{\sqrt{\text{MSE}}} \right) \quad (2-4)$$

,where MAX_I is maximum intensity of the signal, P_{signal} is intensity of signal, P_{noise} is intensity of noise, and MSE is mean square error:

$$MSE = \frac{1}{n} \sum_i^n (\hat{Y}_i - Y_i)^2 \quad (2-5)$$

The SNR of the circuit was measured as 215. The PSNR of the circuit was measured as 431. Measurement was possible with a 10-bit ADC circuit, but a circuit with a high signal-to-noise ratio was needed for more precise measurement.

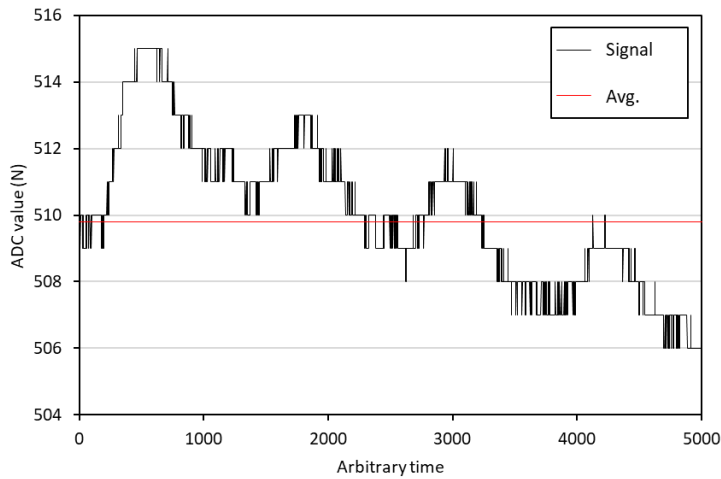


Figure 2-12. Signal-to-noise test of measurement circuit with 10-bit ADC.

The performance of the fabricated 16-bit ADC measurement circuit was evaluated. A precision resistor was connected to the measurement circuit, and the signal value was measured while maintaining a constant temperature. The SNR of

the sensor was measured using the deviation value of the 2000 signal values (Figure 2-13). The SNR of the 16-bit circuit was measured as 1540. The PSNR of the circuit was measured at 4347. As a result of circuit reconstruction, SNR increased by 7 times than the previous 10-bit circuit (Table 2-3).

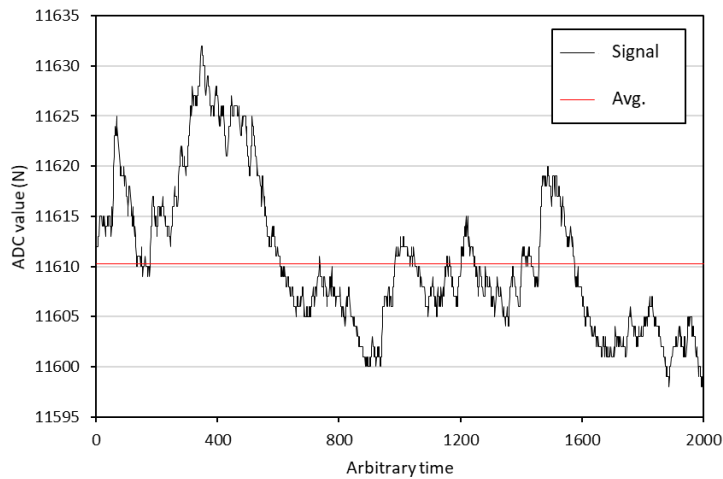


Figure 2-13. Signal-to-noise test of measuring circuit with 16-bit ADC.

Table 2-3. SNR and PSNR comparison between 10-bit and 16-bit circuit.

	SNR (dB)	PSNR (dB)
10-bit circuit	214.7 (46.64)	430.9 (52.69)
16-bit circuit	1540 (63.75)	4347 (72.76)

2.4. Design for electrical breakdown prevention

2.4.1. What is electrical breakdown

Electrical breakdown was observed during testing of the microneedle probe. The electrical breakdown is a phenomenon in which leakage current flows due to the dielectric failure of the insulating layer. In case of the microneedle probe sensor, current flows through the top dielectric layer, resulting in electrochemical corrosion and electrode damage.

2.4.2. Analysis of electrical breakdown phenomena

Gold was used as the electrode material of the microneedle sensor for its high electrical conductivity and chemical inertness. Gold is one of the least reactive metals and stable in natural environments. In general, gold is considered as an ideally inert electrode. It is known that it is susceptible to dissolution in the presence of complexing agents like CN^- , Cl^- or Br^- [11, 12]. The corrosion of gold is accelerated in anodic condition and even can be dissolved into solution [13, 14, 15].

The main cause of electrical breakdown is mechanical failure of the dielectric layer. As shown in Figure 2-14, if the upper dielectric layer is mechanically damaged, the gold electrode is exposed to the solution and then corroded, resulting in open circuit. This problem may be caused by weak adhesion of the insulating layer. Electrical breakdown can also be caused by invisible defects such as pin holes during deposition. As shown in Figure 2-15, in the absence of the mechanical

damage, corrosion and dissolution of gold is observed. The cause of the electrode corrosion is the pinhole defect created during the deposition process of dielectric layer. Corrosion of the electrode is accelerated and propagated by the electrochemical potential even in the presence of invisible defects less than a few nanometers.

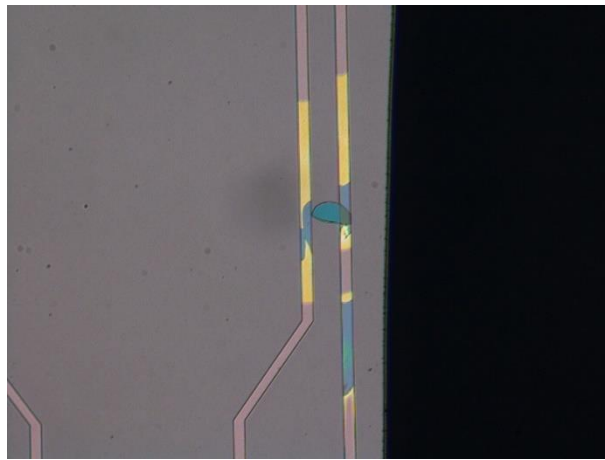


Figure 2-14. Electric breakdown by mechanical defect.

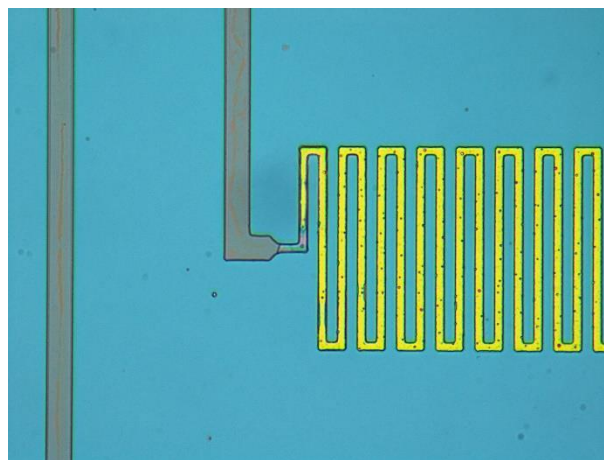


Figure 2-15. Electric breakdown by pinhole defect

2.4.3. Electrode patterning process to minimize electrical breakdown

To more precisely observe the electrical breakdown phenomenon, FE-SEM (Hitachi, S-4800) images of the metal electrode were obtained (Figure 2-16, 17). In the SEM image, a defect protruding from the edge of some electrodes was observed. The height of the defect was less than 1 μm , and the defect deemed the electrode vulnerable to electrical breakdown through the dielectric layer.

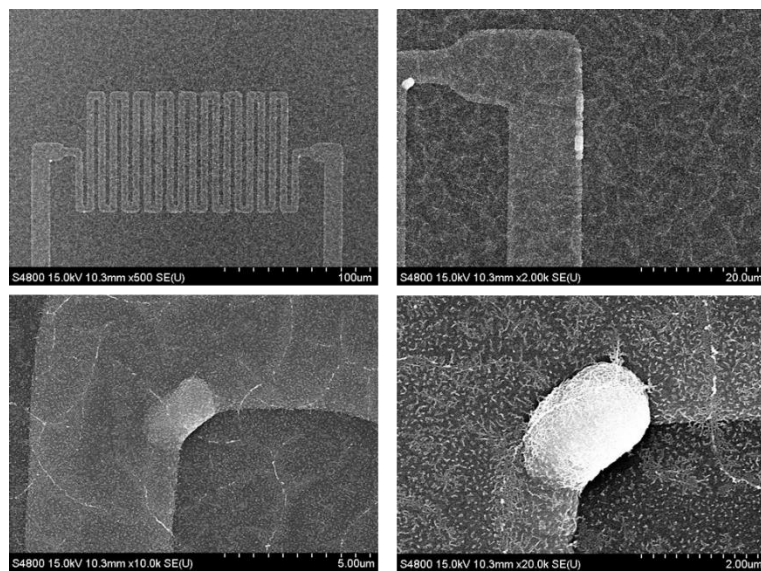


Figure 2-16. FE-SEM image of the fabricated electrode with lift-off process (top view).

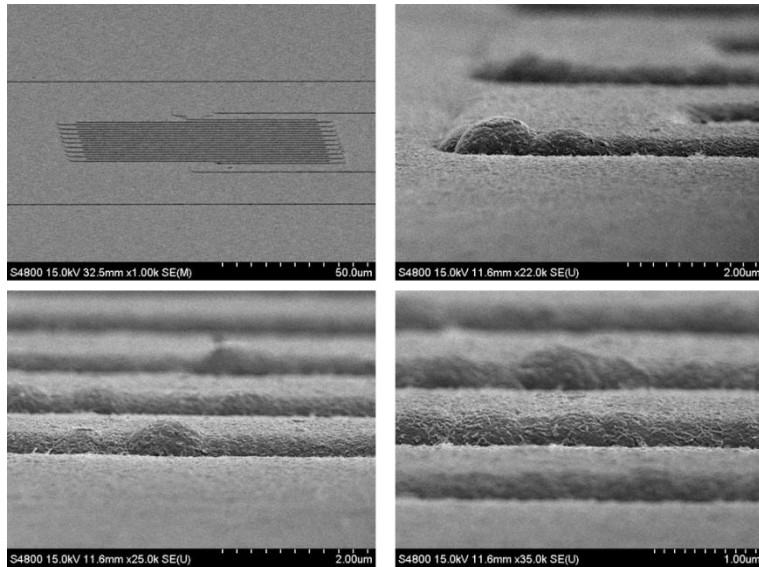


Figure 2-17. SEM image of the fabricated electrode with lift-off process (side view).

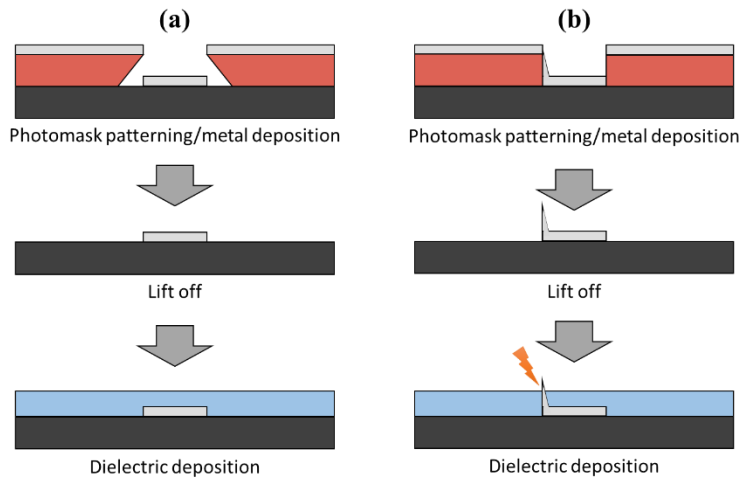


Figure 2-18. Lift-off process flow with dielectric deposition in ideal case (a). Shear fracture and shear lip created during the non-ideal lift-off process (b).

This defect is caused by the lift-off process during the metal patterning process. In a usual lift-off process, patterning with a negative photoresist allows clean patterning as shown in Figure 2-18 (a). However, when undercut angle of photomask pattern is insufficient or sidewall deposition occurs as shown in Figure

2-18 (b), shear fracture occurs during the lift-off process. This causes a shear lip to break through the insulating layer and cause electrical breakdown. This problem was solved by using dry etching process instead of lift-off process for metal patterning (Figure 2-19). Shear lip was not observed from SEM image of the electrode patterned by dry etching process (Figure 2-20).

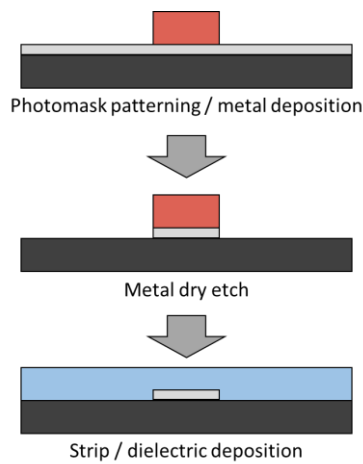


Figure 2-19. Process flow of electrode patterning with dry etch process.

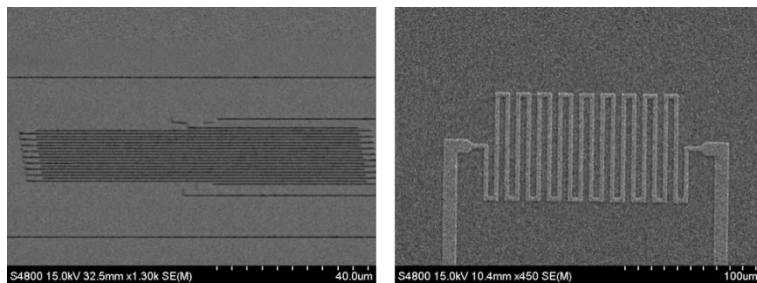


Figure 2-20. SEM image of the fabricated electrode with dry etch process.

2.4.4. Composite dielectric layer process to minimize electrical breakdown

During the deposition of the insulating layer, formation of defects such as pin holes or nano-cracks is inevitable. These defects are not visible in optical microscope, nonetheless ionic solution penetrates and causes electrode breakdown. Generally, the size of the pinhole defect decreases with the increase of the layer thickness resulting in enhanced barrier properties. However, if the thickness of the insulating layer exceeds a certain thickness, the insulating effect does not increase significantly since the defects tend to grow in single-component layers [16]. A multilayer or composite thin film layer can cover the defects and better dielectric property can be expected [16, 17].

A multilayer of silicon nitride, silicon oxide, and fluorocarbon polymer was used as the insulating layer of the microneedle probe (Figure 2-21). 5 layers of intervening 2000 Å silicon nitride layers and 2000 Å silicon dioxide layers were deposited via High Density Plasma Chemical Vapor Deposition (HDPCVD, BMR, HiDep). 100 Å of fluorocarbon layer was deposited with deep reactive-ion etching machine (PLASMA-THERM, SLR-770) for additional hydrophobic layer and defect filling.

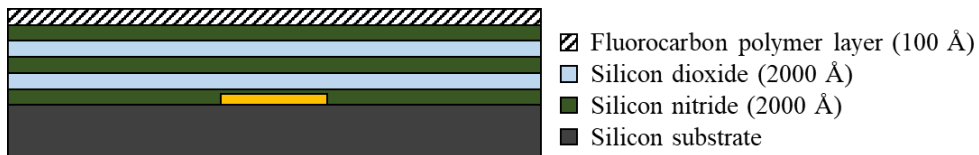


Figure 2-21. Multilayer composite dielectric layer.

2.4.5. Negative voltage driving to minimize electrical breakdown

The heating thermistor in microneedle probe is operated at a negative potential in order to minimize electrochemical corrosion. If the electrode is exposed to the surrounding solution during the operation, the electrode and surrounding solution become an electrochemical cell. The sap in vascular bundle or cytoplasm in plant cells are electrically grounded. If the heating thermistor is operated at a positive voltage, the potential of the electrode is relatively higher than the electrolyte and becomes anode. Thus operating the heating thermistor with a positive voltage accelerates the corrosion process. On the other hand, if the heating thermistor is operated at a negative voltage, the exposed electrode becomes cathode and the corrosion process is inhibited (Figure 2-22). Figure 2-23 shows the results of accelerated corrosion test for comparison between positive and negative voltage operation. The electrode operated at a negative voltage was intact after 24 hours of operation while the electrode operated at a positive voltage had dialectical failure within 1 hour of operation.

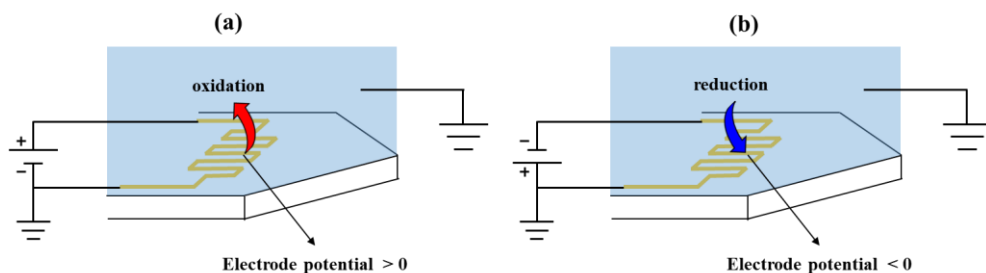


Figure 2-22. Microneedle probe operation in ionic solution. Oxidation from electrode in positive voltage driving (a). reduction from electrode in negative voltage driving (b).

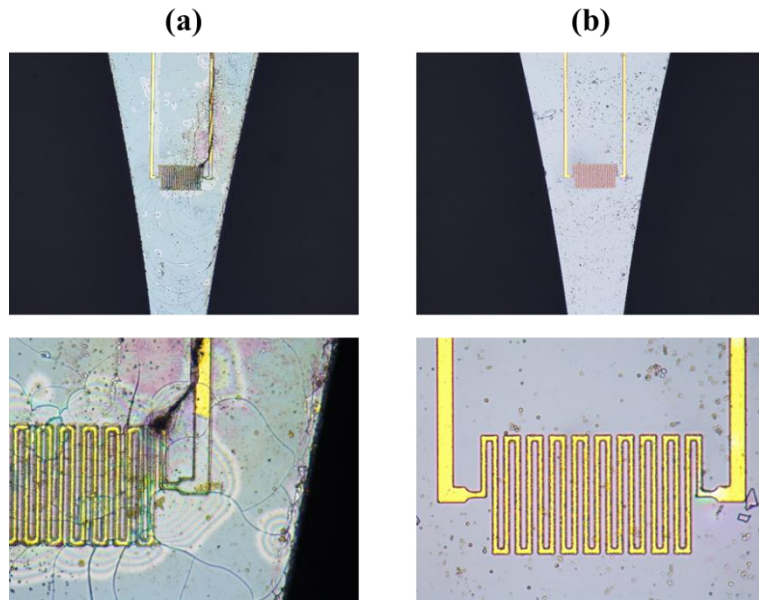


Figure 2-23. Optical microscope image of heating thermistor electrode after accelerated corrosion test. Electrode after 1 hour of operation at +10 V (a). Electrode after 24 hours of operation at -10 V (b).

2.5. Configuration of complete measurement system

The entire measurement system consists of a sensor packaging board, a measurement circuit, a power supply, and a PC for data acquisition (Figure 2-24 (b)). The sensors were installed in the radial direction on the stem of the plant (Figure 2-24 (a)). The sensor packages were connected to the measurement circuit with IPEX MHF (IPEX) connector and RG-316 coaxial cable with SMA extension. The MCU of the measurement circuit was driven by the Arduino boot loader. A firmware was custom designed using Arduino Integrated Development Environment (ARDUINO, version 1.6.7). The measured digital signal was converted from UART serial to USB protocol. The data was sent to the PC through either wired RS 232, RS 485, or wireless Bluetooth communication. The data was transmitted to PC and stored using custom designed DAQ program using Processing IDE (PROCESSING, version 3.0.1). The stored data was converted to sap flow data using Matlab (MathWorks).

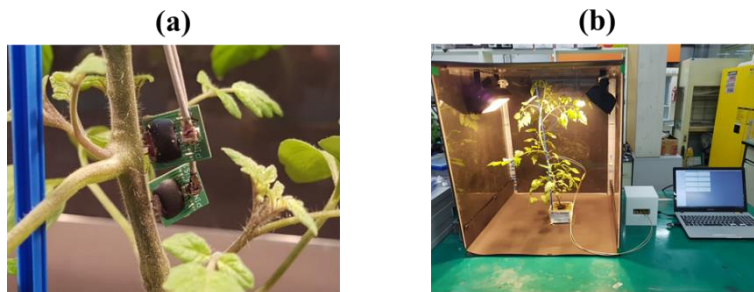


Figure 2-24. Sap flow sensor installed on plant stem (a), Entire measurement system (b).

2.6. Performance specification of the measurement system

The performance evaluation results of the fabricated sensor system are as follows. The electrical and thermal properties of the sensor meet the initially set points (Table 2-4, 5). The performance of the flow rate measurement satisfies the target performance (Table 2-6).

Table 2-4. Electric properties of measurement system.

	resistance (Ω)	operating voltage (V)	power consumption (mW)	voltage resolution (mV)	RMS voltage error (mV)	SNR of voltage
Target	200 ~ 300	< 5	< 100	< 1	< 5	> 1000
Result	240 ~ 270	4.5	67.5	0.153	1.14	1540

Table 2-5. Thermal properties of measurement system.

	Operating temperature ($^{\circ}\text{C}$)	Measureable temperature range (K)	Heating temperature (K)	Temperature resolution (mK)	RMS temperature error (mK)
Target	-10~40	> ± 5	< 3	< 3	< 15
Result	-10~40	± 8.6	2.5	0.522	3.9

Table 2-6. Performance of measurement system at $u=1$ mm/s.

	Measurable flow range (mm/s)	Flow speed resolution ($\mu\text{m/s}$)	SNR of flow speed	RMS error of flow speed ($\mu\text{m/s}$)
Target	0 ~ 1	< 2	> 20	< 50
Result	0 ~ 4	1.80	73.8	13.6

2.7. Conclusion

Microneedle probe sensor for fluid flow measurement was designed and fabricated with MEMS process. The measurement method for sap flow with minimal invasion using a single microneedle probe was designed. Microneedle sensors were fabricated using MEMS fabrication technology. A system for signal measurement and data acquisition of sensors was configured and evaluated. Software for data collection using open source IDEs were designed. Various designs were adopted to minimize the breakdown phenomenon of the sensor. Finally, a complete measurement system for the flow measurement of the plant was built (Figure 2-25).

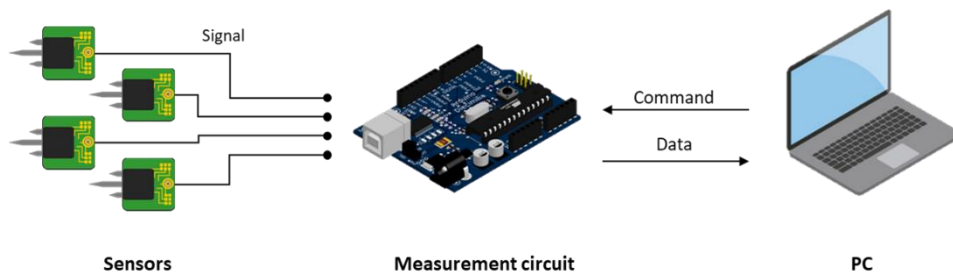


Figure 2-25. Diagram of the entire measurement system.

Bibliography

- [1] A. Granier, "Une nouvelle méthode pour la mesure du flux de sève brute dans le tronc des arbres," in *Annales des Sciences forestières*, vol. 42, no. 2, pp. 193-200, 1985.
- [2] L. V. King, "On the Convection of Heat from Small Cylinders in a Stream of Fluid: Determination of the Convection Constants of Small Platinum Wires with Applications to Hot-Wire Anemometry," *Philosophical Transactions of the Royal Society of London. Series A, Containing Papers of a Mathematical or Physical Character*, vol. 214, pp. 373-432, 1914.
- [3] Sap flow sensor. Available from: <http://www.ecotechnic.be>
- [4] P. Lu, L. Urban, and P. Zhao, "Granier's thermal dissipation probe (TDP) method for measuring sap flow in trees: theory and practice," *ACTA BOTANICA SINICA-ENGLISH EDITION*-, vol. 46, no. 6, pp. 631-646, 2004.
- [5] M. J. Daley and N. G. Phillips, "Interspecific variation in nighttime transpiration and stomatal conductance in a mixed New England deciduous forest," *Tree Physiology*, vol. 26, no. 4, pp. 411-419, 2006.
- [6] N. G. Phillips, J. D. Lewis, B. A. Logan, and D. T. Tissue, "Inter-and intra-specific variation in nocturnal water transport in *Eucalyptus*," *Tree Physiology*, vol. 30, no. 5, pp. 586-596, 2010.
- [7] I. Rabbal, B. Dieckkrüger, H. Voigt, and B. Neuwirth, "Comparing ΔT_{max} Determination Approaches for Granier-Based Sapflow Estimations," *Sensors*, vol. 16, no. 12, p. 2042, 2016.
- [8] T. W. Davis, C.-M. Kuo, X. Liang, and P.-S. Yu, "Sap flow sensors: construction, quality control and comparison," *Sensors*, vol. 12, no. 1, pp. 954-

971, 2012.

- [9] M. Masmoudi, I. Mahjoub, J.-P. Lhomme, and N. B. Mechlia, "Sap flow measurement by a single thermal dissipation probe in transient regime: implementation of the method and test under field conditions," *Annals of forest science*, vol. 69, no. 7, pp. 773-781, 2012.
- [10] K. Steppe, D. J. W. De Pauw, T. M. Doody, and R. O. Teskey, "A comparison of sap flux density using thermal dissipation, heat pulse velocity and heat field deformation methods," *Agricultural and Forest Meteorology*, vol. 150, no. 7, pp. 1046-1056, 2010.
- [11] S. Cherevko, A. A. Topalov, A. R. Zeradjanin, I. Katsounaros, and K. J. Mayrhofer, "Gold dissolution: towards understanding of noble metal corrosion," *Rsc Advances*, vol. 3, no. 37, pp. 16516-16527, 2013.
- [12] A. D. Bas, E. Ghali, and Y. Choi, "A review on electrochemical dissolution and passivation of gold during cyanidation in presence of sulphides and oxides," *Hydrometallurgy*, vol. 172, pp. 30-44, 2017.
- [13] K. Cathro and D. Koch, "The anodic dissolution of gold in cyanide solutions," *Journal of The Electrochemical Society*, vol. 111, no. 12, pp. 1416-1420, 1964.
- [14] Y. Ling, J. C. Elkenbracht, W. F. Flanagan, and B. D. Lichter, "The Electrochemical Oxidation of Gold in 0.6 M NaCl and 0.3 M Na₂ SO₄ Solutions," *Journal of The Electrochemical Society*, vol. 144, no. 8, pp. 2689-2697, 1997.
- [15] S. Zhang and M. Nicol, "An electrochemical study of the dissolution of gold in thiosulfate solutions Part I: Alkaline solutions," *Journal of Applied Electrochemistry*, vol. 33, no. 9, pp. 767-775, 2003.
- [16] J. G. Lee, H. G. Kim, and S. S. Kim, "Defect-sealing of Al₂O₃/ZrO₂

multilayer for barrier coating by plasma-enhanced atomic layer deposition process," *Thin Solid Films*, vol. 577, pp. 143-148, 2015.

[17] E. Harkonen et al., "Sealing of hard CrN and DLC coatings with atomic layer deposition," *ACS applied materials & interfaces*, vol. 6, no. 3, pp. 1893-1901, 2014.

Chapter 3. Theory and Analysis

3.1. Thermal analysis of microneedle probe

3.1.1. Theoretical background and assumptions

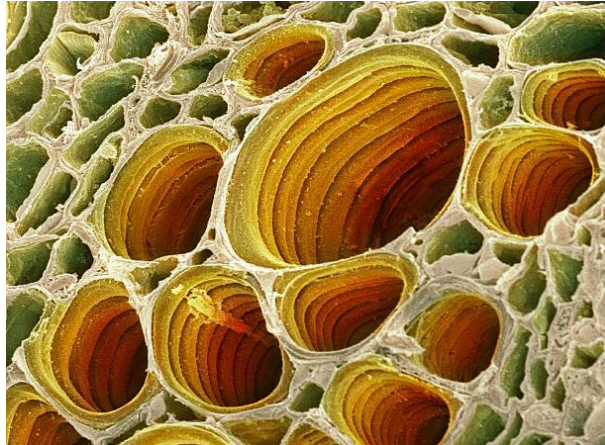


Figure 3-1. SEM image of the vascular bundle [1].

The water transport of the vascular plant stem is carried out through a xylem. The xylem is composed of tracheid and vessel elements which are bundles of thin tubes (Figure 3-1). Passive transport of water and inorganic minerals takes place through xylem by water potential gradient. The diameter of each vascular tubes in xylem is $10 \sim 100\mu\text{m}$. In xylem, a conjugated heat transfer occurs where convection and conduction are combined. This complex in vivo flow and heat transfer can be modeled as heat transfer in a porous medium [2].

3.1.2. Energy equation for conjugated heat transfer in porous media

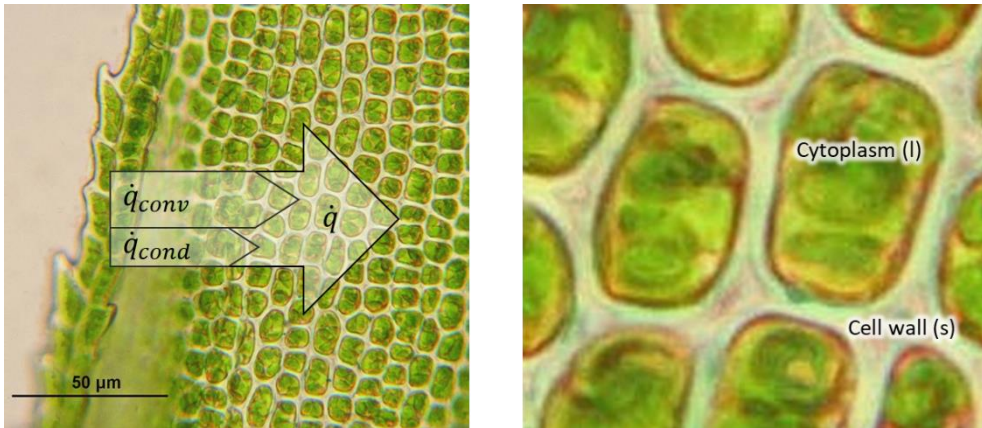


Figure 3-2. Heat transfer modes in porous plant tissues (left). Cytoplasm and cell wall (right).

Assume heat transfer in a porous medium with isotropic thermal properties. Convective heat transfer by the fluid phase and conductive heat transfer by the solid phase occur simultaneously in the porous medium (Figure 3-2). The energy equation in the medium can be expressed as:

For solid phase:

$$(1 - \phi)(\rho c)_s \frac{\partial T_s}{\partial t} = (1 - \phi) \nabla \cdot (k_s \nabla T_s) + (1 - \phi) q_s''' \quad (3-1)$$

For fluid phase:

$$\phi(\rho c_p)_f \frac{\partial T_f}{\partial t} + (\rho c_p)_f \mathbf{v} \cdot \nabla T_f = \phi \nabla \cdot (k_f \nabla T_f) + \phi q_f''' \quad (3-2)$$

[3].

Suppose that the solid phase and fluid phase are in a local thermal equilibrium state. So that, $T_s = T_f = T$, From equations (3-1) and (3-2), we have:

$$(\rho c) \frac{\partial T}{\partial t} + (\rho c)_f \mathbf{v} \cdot \nabla T = \nabla \cdot (k \nabla T) + q''', \quad (3-3)$$

where $(\rho c) = (1 - \varphi)(\rho c)_s + \varphi(\rho c_p)_f$, $k = (1 - \varphi)k_s + \varphi k_f$, $q''' = (1 - \varphi)q_s''' + \varphi q_f'''$.

And, φ is porosity. $(\rho c)_s$, $(\rho c_p)_f$, (ρc) are specific heat of solid, specific heat of fluid at constant pressure, averaged specific heat. $\mathbf{v} = (u, v, w)$ is average of fluid velocity. T_s , T_f , T are temperature of solid, fluid, averaged. k_s , k_f , k are heat conductivity of solid, fluid, averaged. q_s''' , q_f''' , q''' are heat generation of solid, fluid, averaged.

3.1.3. Lumped capacitance method

The convective heat transfer phenomenon can be simplified through the lumped capacitance method. It is necessary to check whether the lumped capacitance method can be applied to the heat transfer in the microneedle probe. If the Biot number, the ratio between the conduction heat transfer through the solid and the convective heat transfer in the fluid, is less than 0.1, the thermal resistance to conduction in the solid is much smaller than the convective heat resistance across the fluid boundary layer and the temperature distribution inside the solid can be assumed to be uniform [4].

$$\text{Bi} = \frac{hL}{k} \sim \frac{100 * 0.5 * 10^{-3}}{130} = 3.8 * 10^{-4} \ll 1 \quad (3-4)$$

The calculation result shows that when the flow rate is in mm/s range, the Biot number of the microneedle probe using the silicon substrate is calculated to be smaller than 0.1 (Equation 3-4). Therefore, it can be concluded that the use of the lumped capacitance method is valid. Now, each term in the energy equation (Equation 3-3) can be expressed as lumped capacitance model as follows.

$$C \frac{\partial T}{\partial t} + \phi h A (T - T_0) + \frac{k}{L} A (T - T_0) = q''', \quad (3-5)$$

where ϕ is porosity. k is thermal conductivity of porous media. L is conduction length. k_f is thermal conductivity of fluid. C is heat capacitance.

3.1.4. Comparison between convective heat transfer versus conduction heat transfer in conjugate heat transfer.

The heat transfer in plant tissue is assumed to be the conjugate heat transfer which is the sum of convective heat transfer in cytoplasm and conduction heat transfer in cell wall. The contribution of each heat transfer modes were evaluated. The ratio between convective heat transfer and conductive heat transfer was defined as follows:

$$K = \frac{\varphi h}{k} L = \varphi \frac{L}{k} \frac{k_f}{x} Nu, \quad (3-6)$$

where, φ is porosity of surrounding media. k is thermal conductivity of porous media. L is conduction length across the probe. k_f is thermal conductivity of fluid. X is characteristic length of the probe. Nu is Nusselt number.

The following assumptions were made:

$$k = (1 - \varphi)k_{wood} + \varphi k_{water}, \quad (3-7)$$

where φ is porosity of medium ($\varphi = 0.5$), k is thermal conductivity of porous media.

$$L = \delta \sim \left(\frac{\alpha_m x}{u} \right)^{1/2} = 3 * 10^{-4} \text{ m}, \quad (3-8)$$

from local thermal equilibrium assumption, (conduction length) = (boundary layer thickness) = δ , α_m is thermal diffusivity of porous media. x is characteristic length of probe = 0.5 mm.

$$\alpha_m = \frac{\varphi k_f + (1 - \varphi)k_s}{\varphi(\rho c_p)_f + (1 - \varphi)(\rho c)_s} \quad (3-9)$$

A circular orthogonal flow was assumed for heat transfer for microneedle probe. Hilpert's empirical correlation equation was used to estimate the Nusselt

number:

$$Nu = 0.989 * Re^{0.33} Pr^{1/3} \quad (3-10)$$

[4].

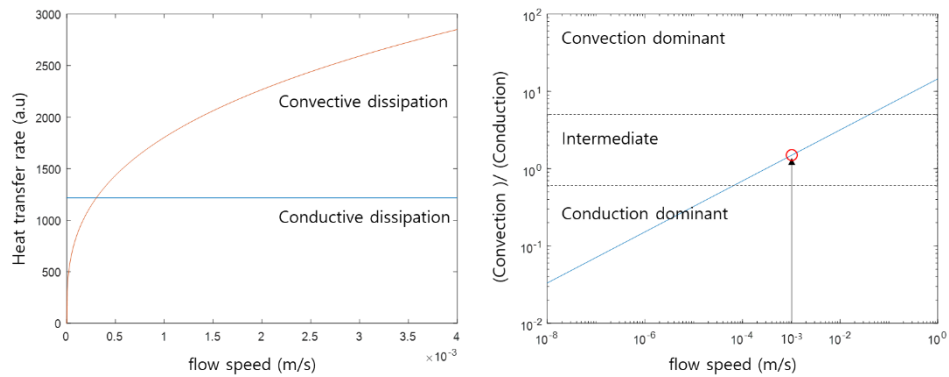


Figure 3-3. Plot of convective heat dissipation and conductive heat dissipation (left), plot of heat dissipation ratio between conduction and convection (right).

Based on these assumptions, the convective and conductive heat fluxes are compared. The convective heat transfer and the conductive heat transfer according to the flow rate were compared. The results show that if the flow velocity is very slow ($u < 10^{-7}$ m/s), the conductive heat transfer is dominant. Convective heat transfer increased as the flow rate increased. At a flow rate in the range of 1 mm/s, which we are aiming to measure, convective heat transfer and conductive heat transfer are within a similar range. Thus, the convective and conductive heat transfer should be considered together. From equation 3-5, if we define the overall heat dissipation constant by convection and conduction as D, the following relation is obtained:

$$C \frac{\partial T}{\partial t} + D(T - T_0) = q''', \quad (3-11)$$

where $D (= \phi hA + \frac{k}{L}A)$ is overall heat dissipation constant.

3.1.5. Single component lumped capacitance model, transient state response

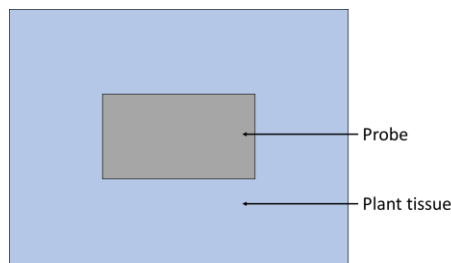


Figure 3-4. Simplified 2D single component heat transfer model.

To predict the phenomenon when steady state heat transfer from heated probe to plant tissue occurs, the needle model is simplified (Figure 3-4). The microneedle is assumed to be an infinitely long rectangular column with uniform thermal properties. The microneedle is wrapped with plant tissue and temperature is maintained at T_0 . There is no heat transmitted through the length of the needle. The fluid flow direction is perpendicular to the needle. The initial temperature of the micro needle is T_0 , the heat capacity is C , and the convective heat transfer coefficient between the micro needle and the surroundings is h . The microneedle is heated by Joule heating (P_E), and the temperature rises to $T_0 + T$. The heat stored in the microneedle is defined as follows.

$$q_{\text{store}}' = C \frac{d}{dt}(T + T_0) \quad (3-12)$$

The heat transferred from the microneedles to the surroundings by convection can be expressed as

$$q_{\text{dissipation}}' = -hA(T_0 - (T + T_0)) \quad (3-13)$$

The thermal equilibrium of the needle during heating can be expressed as

$$P_E = q_{\text{store}}' + q_{\text{dissipation}}' \quad (3-14)$$

Therefore, the correlation of the temperature of the microneedle with respect to time can be expressed as follows:

$$P_E = C \frac{d}{dt}T + hAT \quad (3-15)$$

Solving the above 1st order ODE yields

$$T = \frac{P_E}{hA} \left(1 - e^{-\frac{hA}{C}t} \right) \quad (3-16)$$

3.1.6. Steady state response of single component lumped capacitance model

Let's take a look at the heat transfer at steady state in the model above. Since the heat generation of probe is equal to the convective heat dissipation, equation 3-14 becomes

$$P_E = q_{\text{dissipation}}' \quad (3-17)$$

and

$$P_E = hAT = \frac{\text{Nu} \cdot k}{l} AT \quad (3-18)$$

In 1914, King derived a solution for the heat transfer from an infinite cylinder in an incompressible low Reynolds number flow that may be written as

$$\text{Nu} = A_1 + B_1 \cdot \text{Re}^n = A_1 + B_1 \left(\frac{\rho u l}{\mu} \right)^n = A' + B' \cdot u^n \quad (3-19)$$

Therefore, the correlation between the flow velocity and the convective heat transfer coefficient is as follows:

$$h = \frac{\text{Nu} \cdot k}{l} = \frac{k}{l} (A' + B' \cdot u^n) = h_0 (1 + \alpha u^\beta), \quad (3-20)$$

where, $h_0 = \frac{kA'}{l}$, $\alpha = \frac{B'}{A'}$, $\beta = n$.

The correlation between flow velocity and steady-state temperature is:

$$T = \frac{P_E}{hA} = \frac{P_E}{h_0A} (1 + \alpha u^\beta)^{-1} \quad (3-21)$$

Expressing for u:

$$\alpha u^\beta = \frac{P_E}{h_0AT} - 1 = \frac{1}{T} \left(\frac{P_E}{h_0A} - T \right) \quad (3-22)$$

$\frac{P_E}{h_0A}$ is the temperature $T_{u=0}$ so it can be written as follows:

$$\alpha u^\beta = \frac{1}{T} \left(\frac{P_E}{h_0A} - T \right) = \frac{1}{T} (T_{u=0} - T) \quad (3-23)$$

For u, we obtain the following equation. For convenience, if we assume that

$\frac{T_{u=0}-T}{T}$ is non-dimensional flow index K, we obtain:

$$u = \left(\frac{1}{\alpha} \frac{T_{u=0} - T}{T} \right)^{\frac{1}{\beta}} = a \left(\frac{T_{u=0} - T}{T} \right)^b = aK^b, \quad (3-24)$$

where $a = \alpha^{-\frac{1}{\beta}}, b = \beta^{-1}, K = \frac{T_{u=0}-T}{T}$.

3.1.7. Multi component lumped capacitance model

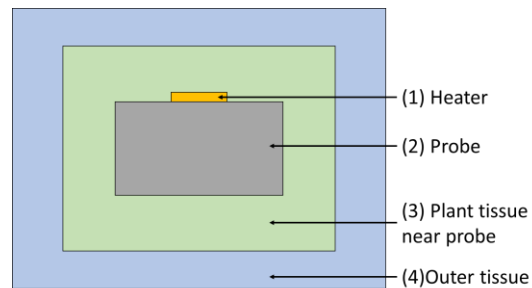


Figure 3-5. Simplified 2D multi component heat transfer model

The heat transfer model of the microneedle is shown in more detail as follows. Micro-needles in plants can be divided into three components (Figure 3-5); heating element, needle probe and plant tissue surrounding heating element and needle probe. And they are wrapped with plant stem with constant temperature. It is assumed that each component is isotropic and has uniform thermal properties. In the heating element, it is assumed that Joule heating occurs at constant power P_E . The initial temperature value of each component is T_0 , and the temperature increase amount of each component over time is expressed as T_1 , T_2 , and T_3 . It is assumed that the ambient temperature T_4 is constant at T_0 . The heat capacity of each component is C_1 , C_2 , and C_3 respectively. Heat transfer occurs by convection and conduction between each component, and the ratio between the sum of the heat transfer due to conduction and convection to the temperature difference is assumed to be the heat transfer coefficient dissipation factor D .

The heat balance equation for each component is as follows:

(1) heater:

$$P_E = q_{s,1} + q_{12} + q_{13} \quad (3-25)$$

(2) probe body:

$$q_{12} = q_{s,2} + q_{23} \quad (3-26)$$

(3) plant tissue near probe:

$$q_{23} + q_{13} = q_{s,3} + q_{34} \quad (3-27)$$

The energy stored in each component are as follows:

$$\begin{aligned} q_{s,1} &= C_1 \frac{dT_1}{dt} \\ q_{s,2} &= C_2 \frac{dT_2}{dt} \\ q_{s,3} &= C_3 \frac{dT_3}{dt} \end{aligned} \quad (3-28)$$

The amount of heat transfer in each component is as follows:

$$\begin{aligned} q_{12} &= -D_{12}(T_2 - T_1) \\ q_{13} &= -D_{13}(T_3 - T_1) \\ q_{23} &= -D_{23}(T_3 - T_2) \\ q_{34} &= -D_{34}(T_4 - T_3) \end{aligned} \quad (3-29)$$

From the equations 3-25 to 29, the heat balance equation can be expressed by the equation for temperature to obtain the following inhomogeneous linear systems of ODE:

(1) heater:

$$P_E = C_1 \frac{dT_1}{dt} - D_{12}(T_2 - T_1) - D_{13}(T_3 - T_1) \quad (3-30)$$

(2) probe body:

$$-D_{12}(T_2 - T_1) = C_2 \frac{dT_2}{dt} - D_{23}(T_3 - T_2) \quad (3-31)$$

(3) plant tissue near probe:

$$-D_{23}(T_3 - T_2) - D_{13}(T_3 - T_1) = C_3 \frac{dT_3}{dt} = -D_{34}(T_4 - T_3) \quad (3-32)$$

These are expressed in a matrix form as follows:

$$\begin{bmatrix} \frac{d}{dt} T_1 \\ \frac{d}{dt} T_2 \\ \frac{d}{dt} T_3 \end{bmatrix} = \begin{bmatrix} -\frac{D_{12} + D_{13}}{C_1} & \frac{D_{12}}{C_1} & \frac{D_{13}}{C_1} \\ \frac{D_{13}}{C_2} & -\frac{D_{12} + D_{23}}{C_2} & \frac{D_{23}}{C_2} \\ \frac{D_{13}}{C_3} & \frac{D_{23}}{C_3} & -\frac{D_{13} + D_{23} + D_{34}}{C_3} \end{bmatrix} \begin{bmatrix} T_1 \\ T_2 \\ T_3 \end{bmatrix} + \begin{bmatrix} P_E \\ 0 \\ 0 \end{bmatrix} \quad (3-33)$$

The general solution to the above equation is:

$$T = \mathbf{c}_1(1 - e^{-\lambda_1 t}) + \mathbf{c}_2(1 - e^{-\lambda_2 t}) + \mathbf{c}_3(1 - e^{-\lambda_3 t}) \quad (3-34)$$

If we assume that the maximum temperature is T_M , and the time constants are τ_1 , τ_2 , and τ_3 , we get:

$$T = T_M - A_1 e^{-t/\tau_1} - A_2 e^{-t/\tau_2} - A_3 e^{-t/\tau_3} \quad (3-35)$$

3.2. Simulation analysis of microneedle probe

3.2.1. Simulation method

Simulation analysis was performed based on the designed microneedle probe. The purpose of the simulation was to determine the feasibility of the design, to verify that the thermal analysis of the microneedle probes was appropriate, and to predict the thermal response during sensor operation. COMSOL multiphysics (COMSOL, version 5.3) was used for the simulation. The simulation model assumes sensors installed into the flow of water at a constant flow rate in a circular tube. The dimensions of the sensor and electrode were the same as those of the mask design. The resistance of the sensor is $300\ \Omega$ and it is assumed that a constant voltage of $4.5\ \text{V}$ is applied to generate $67.5\ \text{mW}$ of heat. The sensor was installed on a $12 * 12 * 0.6\ \text{mm}$ PCB board and was fixed using epoxy resin. It is assumed that a sensor is installed at the center of the $30\ \text{mm}$ long, $2\ \text{mm}$ internal diameter conduit. The flow condition in conduit was assumed to be fully developed internal pipe flow. The temperature change of the heating thermistor was simulated for 30 seconds at different subject flow rates: 0, 1, 2, 3, 4 mm/s (Figure 3-6).

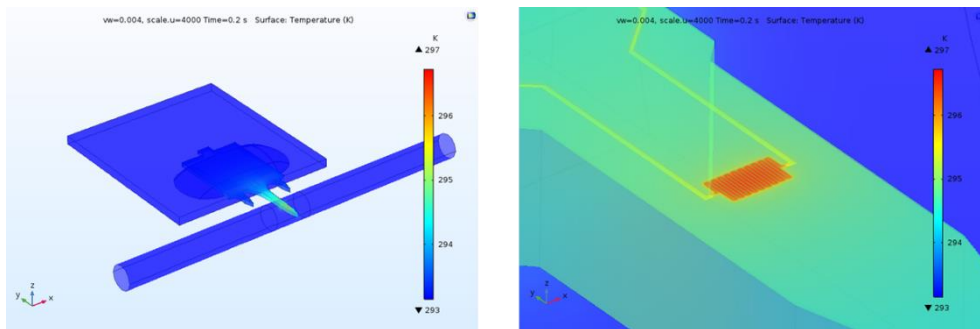


Figure 3-6. COMSOL simulation model. Full model image (left), image of heating thermistor in simulation (right).

3.2.2. Transition heat transfer simulation

First, the temperature change of the heating thermistor was calculated during the heating time for 30 seconds when there was flow in the conduit. As a result, the shape of the temperature change was in the form of exponential decay (Figure 3-7). As expected, the temperature rise of the probe decreased as the flow rate increased. Also, as the flow rate increased, the probe temperature quickly converged to the steady state temperature.

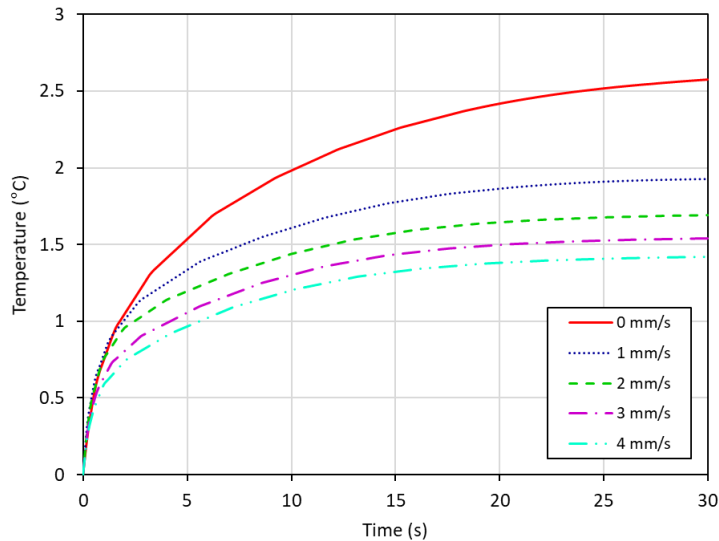


Figure 3-7. Temperature change of heating probe by flow speed from simulation.

The curve fitting of the temperature-time graph was performed based on the 3-component lumped capacitance model obtained from Equation 3-35 to analyze a more detailed thermal phenomenon. Table 3-1 shows the results of curve fitting of the time-temperature graph obtained from the simulation to the 3-component lumped capacitance model ($T = T_M - A1e^{-t/\tau_1} - A2e^{-t/\tau_2} - A3e^{-t/\tau_3}$). As the

flow rate increases, the steady state heating temperature T_M decreases. This is explained by Equation 3-16 that the convective heat transfer coefficient increases and the steady state heating temperature decreases as the flow rate increases. In addition, the time constant τ_1 , τ_2 , and τ_3 decrease as the flow rate increases. This can be explained from Equation 3-16 that the time constant value is inversely proportional to the convective heat transfer coefficient h . The R^2 value in Table 3-1 means the coefficient of determination of the curve fitting. As the coefficient of determination values for curve fitting were larger than 0.999, the 3-component lumped capacitance model was well applied to the simulation.

Table 3-1. curve fitting result of time-temperature graph of heat dissipating probe by flow speed from simulation and 3-component lumped capacitance model.

Flow (mm/s)	T_M (°C)	A1 (°C)	τ_1 (s)	A2 (°C)	τ_2 (s)	A3 (°C)	τ_3 (s)	R^2
0	2.69	0.391	0.401	0.486	1.52	1.81	10.49	0.99994
1	1.97	0.221	0.163	0.602	0.76	1.15	8.51	0.99982
2	1.72	0.073	0.118	0.675	0.55	0.98	8.05	0.99969
3	1.56	0.059	0.087	0.528	0.48	0.98	7.54	0.99975
4	1.44	0.045	0.005	0.473	0.46	0.92	7.38	0.99981

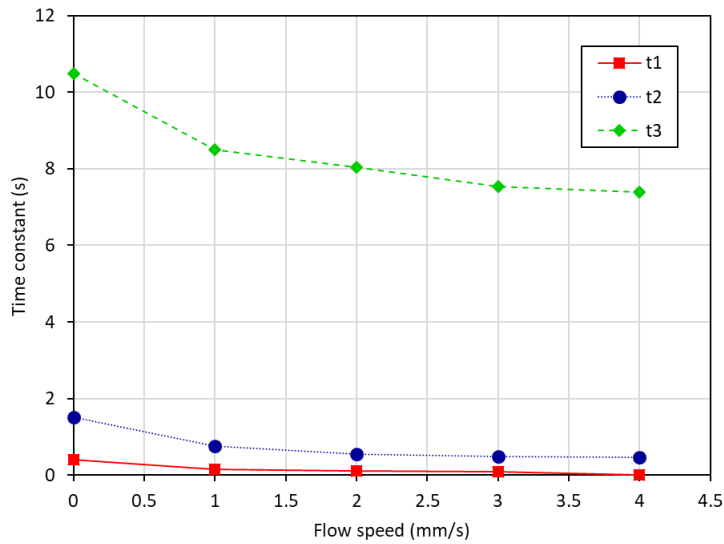


Figure 3-8. Flow speed – exponential dissipation time constant plot from simulation.

3.2.3. Steady-state heat transfer simulation

A simulation was performed when the temperature of the probe reached a steady state or quasi-steady state after a certain period of time had elapsed with the heating. After heating for 30 seconds, the correlation between the temperature change value T and the flow rate was calculated. The simulation results were fitted on the basis of Equation 3-21. The correlation between the flow velocity and the steady-state temperature was predicted with the lumped capacitance model based on Equation 3-35.

The quasi-steady state heated temperature of probe decreased as the flow rate increased. The fitting results were also consistent with the simulation results (Equation 3-36). The correlation between temperature and flow velocity based on simulation and curve fitting is shown in Figure 3-9.

$$T_{simul,u} = (0.388 + 0.131 \cdot u^{0.634})^{-1} \text{ (}^\circ\text{C)} \quad (3-36)$$

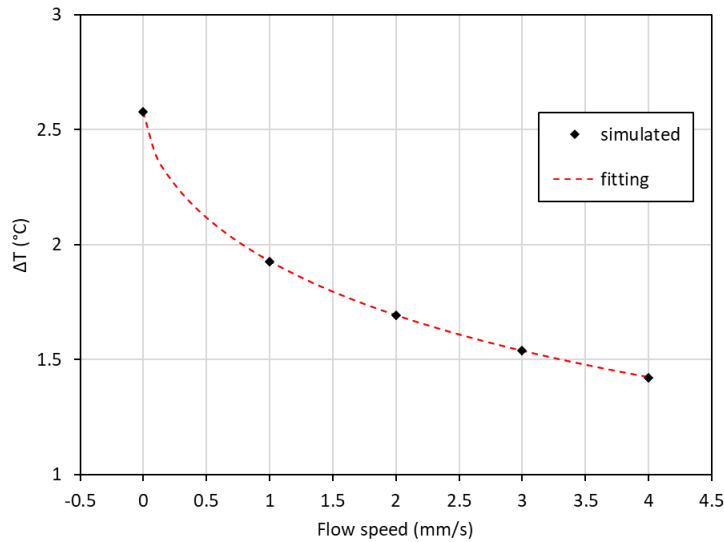


Figure 3-9 . Obtained flow speed-temperature difference plot from simulation result and curve fitting based on Equation 3-36.

In the actual measurement, we know the temperature change value when the flow rate is zero, and estimate the flow rate by evaluating an arbitrary temperature change value. For the flow rate calculation, the temperature change was converted to a flow index ($\frac{T_{u=0}-T}{T}$). Based on the temperature-flow rate relationship in Equation 3-24, the curve fitting between the flow index and the flow velocity was performed (Equation 3-37). The fitting results are in good agreement with the simulation results. The results are shown in Figure 3-10. The simulation confirmed the feasibility of our assumption of the heat transfer model and confirmed that the flow rate can be estimated through the temperature change of probe.

$$u = 5.53 \cdot \left(\frac{T_{u=0} - T}{T} \right)^{1.57} \quad (\text{mm/s}) \quad (3-37)$$

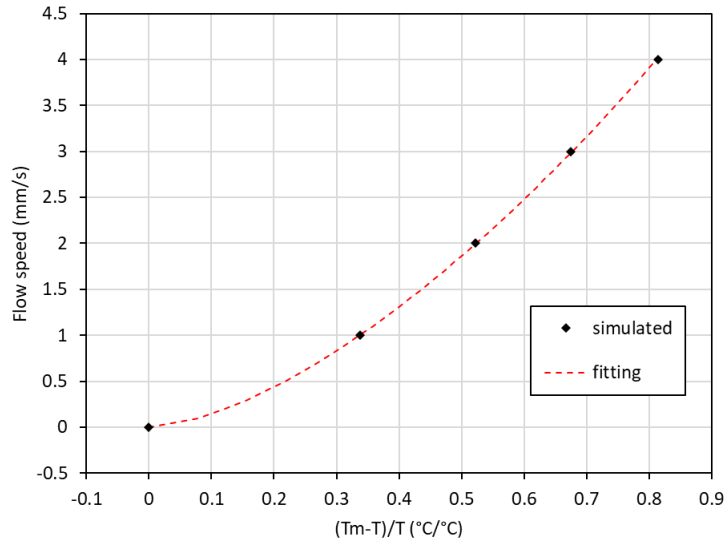


Figure 3-10. Obtained flow index-flow speed plot from simulation result and curve fitting based on Equation 3-24.

3.3. Conclusion

The thermal characteristics of the microneedle probes were analyzed and verified by simulation. The heat transfer in plant tissue was assumed as conjugated heat transfer in porous media. The steady state and transient thermal response of microneedle probe was predicted with analytical model and confirmed with multiphysics simulation. The simulation result showed a consistent thermal response and predicted the thermal characteristic of sensor.

Bibliography

- [1] SEM image of vascular bundle. Available from:
<http://www.sciencephoto.com>.
- [2] A. R. A. Khaled and K. Vafai, "The role of porous media in modeling flow and heat transfer in biological tissues," *International Journal of Heat and Mass Transfer*, vol. 46, no. 26, pp. 4989-5003, 2003.
- [3] D. A. Nield, A. Bejan, and Nield-Bejan. *Convection in porous media*. Springer, 2006.
- [4] T. L. Bergman and F. P. Incropera, *Introduction to heat transfer*. John Wiley & Sons, 2011.

Chapter 4. Thermal Characterization and Calibration

4.1. Analysis of thermal characteristics by heating power

4.1.1. Basic thermal property of microneedle probe

Before applying the fabricated sensor to actual measurement, the basic performance of the sensor was evaluated and calibrated. The evaluation of the sensor was made by measuring the initial resistance value, measuring the temperature change during heating, calibrating the flow in a pipe, and calibrating the flow in a plant stem. The target resistance value at the design stage was 240 Ω and the resistance value range was measured between 240 Ω and 270 Ω . The deviation of the initial resistance value of the sensor was within about 10%, which is affected by the uniformity in the processes such as photomask patterning, thin film deposition, and etching. If the acceptable resistance variation range is $\pm 5\%$, the sensor yield is over 95%. The characteristics of the sensor can be different for each batch and for individual wafers. However, wafers fabricated in the same batch had relatively uniform characteristics. Since the heating power of the resistor is determined by the resistance, a uniform heat characteristic is expected from a uniform resistance value.

4.1.2. Heating power of microneedle probe

The thermal properties of the fabricated sensor according to the heating power were evaluated. The sensor was driven at a constant power and the temperature difference is measured. A sensor with 240 Ω resistance was used for the experiment. The microneedle probe was inserted into a tomato plant stem about 1.5 cm in diameter. The sensor was connected to the measurement circuit and the signal was measured while the power was applied for a fixed period of time. The temperature was measured every 200 ms with heating for 30 seconds. The heating power was increased from 10 mW to 120 mW at intervals of 10 mW.

Table 4-1. Table of operating voltage, resolution, ADC value change, temperature change by the driving power of microneedle probe.

Power (mW)	Voltage (V)	Resolution (K)	ADC value change	ΔT (K)
10	1.55	0.001518	240	0.364
20	2.19	0.001073	760	0.816
30	2.68	0.000876	1195	1.047
40	3.1	0.000759	1843	1.399
50	3.46	0.000679	2657	1.803
60	3.79	0.00062	3599	2.23
70	4.1	0.000574	4061	2.33
80	4.38	0.000537	5137	2.756
90	4.65	0.000506	6431	3.254
100	4.9	0.00048	7471	3.586
110	5.14	0.000458	8138	3.724
120	5.37	0.000438	9259	4.057

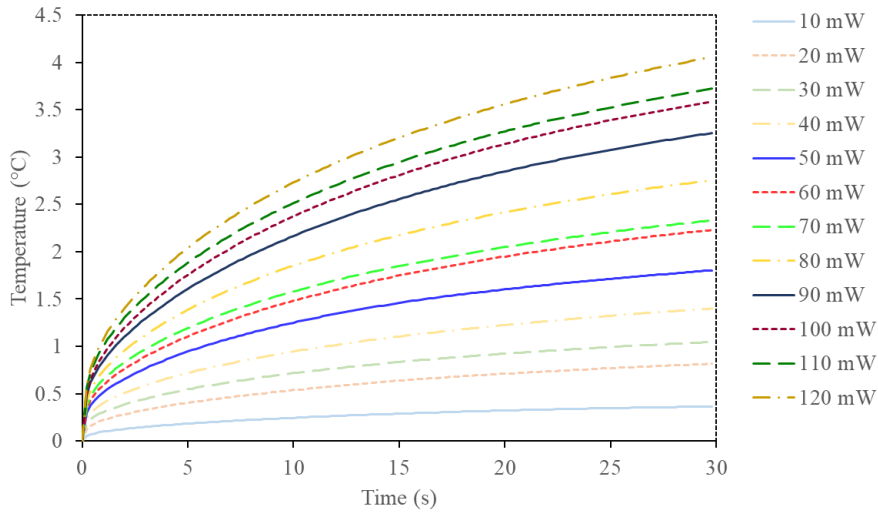


Figure 4-1. Temperature graph of microneedle probe while heating.

The experimental results are shown in Figure 4-1 and Table 4-1. The temperature change graph during heating of the microneedle probe was similar to that of an exponential decay. This result is consistent with Equation 3-16, which predicts the thermal properties of the probe using a lumped capacitance model. Also, it was confirmed that the rising temperature increases as the heating power increases. Table 4-1 shows the detailed experimental conditions and results for each heating power. For example, to drive a sensor with a resistance of 240 Ω to 10 mW, 1.55 V of driving voltage is required. At this time, the minimum temperature change that can be measured using the ADC is 0.00152 K. After heating for 30 seconds, the change in measured value at ADC is 240. ADC value change times resolution is the temperature change after heating. In 10 mW case, the temperature change after heating was 0.364 K. The experiment was repeated while increasing the driving power. The driving voltage needs to be increased as the driving power increases. Lower driving voltage is preferred because the

dielectric layer of the microneedle probe is more vulnerable to electrical breakdown at high driving voltage. Also, the operating voltage of the Wheatstone bridge is twice the voltage supplied to the sensor. Therefore, higher operating voltage requires high performance power supply. The desirable operating voltage was below 5 V. The temperature resolution of the electronics was decreased as the driving voltage increased. Temperature resolution of 1 mK or below was required for accurate measurement. Changes in the ADC value and temperature increased as the operating power increased. Higher ADC value change is desirable in order to increase SNR. Higher temperature and ADC value change also increases the resolution and precision of the measurement. However, the measurable range of ADC value is limited by the electronics. Also, in order to minimize thermal invasion to plant tissue, the maximum operating temperature difference was limited to 2.5 K. Taking all of the above into account, the desirable operation power was set to 70 mW.

4.1.3. Analysis of the experimental result with lumped capacitance model

In chapter 3, the thermal response of microneedle probe is studied with lumped capacitance model. In this experiment, a 3-element lumped capacitance model (Equation 3-35) was used for analysis of heating temperature response of a microneedle probe. Figure 4-2 shows the temperature change of the probe while the heating at 40 mW for 30 seconds as an example. The curve was fitted using the lumped capacitance model. The graph shows that the curve fitting results match the actual measurement results. The fitting result can be expressed as

$$T = 1.67 - 0.261e^{-t/0.133} - 0.228e^{-t/2.23} - 1.18e^{-t/20.5}, \quad (4-1)$$

where T is temperature change and t is time after heating. The coefficient of determination was 0.99996. The results for the rest of the drive power were also curve fit in the same way.

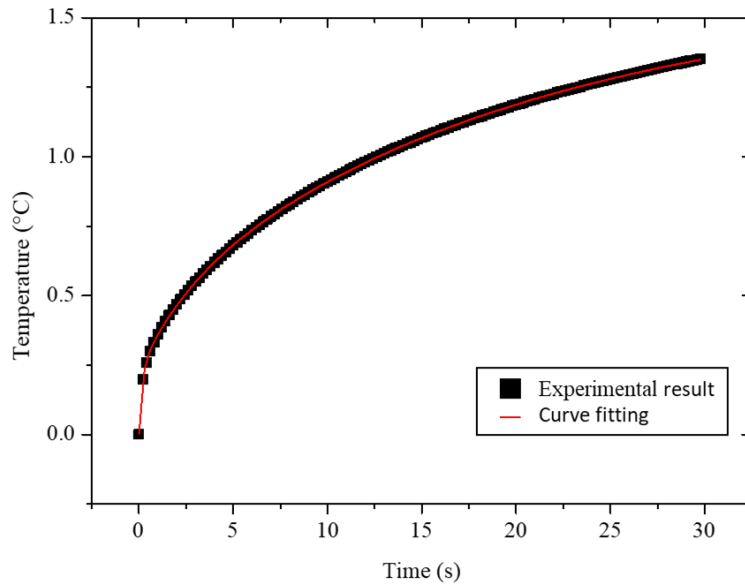


Figure 4-2. Curve fitting result of the temperature change graph of the probe heated to 40 mW for 30 seconds.

Table 4-2 shows the result of curve fitting of the probe temperature variation graph according to the driving power. In the curve fitting results, y_0 represents the temperature rise of the probe when the heating time is infinite. As shown in Figure 4-3, the temperature rise is linearly proportional to the heating power. This is the same result as expected from Equation 3-16. Figure 4-4 shows the change of time constant due to the driving power. There were three time constants (τ_1 , τ_2 , τ_3) in the curve fitting. The shortest time constant (τ_1) is expected to be related to heat

transfer between heater element and probe body which is the fastest thermal equilibrium process. Likewise, τ_2 is expected to be related to heat transfer between probe body and surrounding plant tissue. The longest time constant (τ_3) is expected to be related to thermal dissipation of plant tissue. It was shown that the driving power of microneedle probe does not affect the time constant during transient heat dissipation. The average time constant value of τ_1 , τ_2 , and τ_3 were 0.14, 2.26, and 19.0 s respectively. The coefficient of determinations for curve fitting were above 0.9999 for all cases.

Table 4-2. Temperature change curve of probe according to heating power.

Power (mW)	y0 (K)	A1 (K)	τ_1 (s)	A2 (K)	τ_2 (s)	A3 (K)	τ_3 (s)	R ²
10	0.42	0.059	0.121	0.049	1.69	0.31	17.3	0.9999
20	0.96	0.135	0.126	0.109	1.73	0.72	19.1	0.99995
30	1.22	0.203	0.132	0.162	2.24	0.86	19	0.99996
40	1.67	0.261	0.133	0.228	2.23	1.18	20.5	0.99996
50	2.04	0.341	0.148	0.295	2.66	1.4	17.1	0.99992
60	2.64	0.372	0.14	0.323	2.15	1.95	19.3	0.99997
70	2.76	0.424	0.151	0.388	2.48	1.94	19.7	0.99996
80	3.27	0.476	0.155	0.454	2.55	2.34	19.9	0.99996
90	3.83	0.54	0.148	0.467	2.33	2.82	18.9	0.99997
100	4.2	0.556	0.15	0.497	2.08	3.15	18.4	0.99998
110	4.37	0.638	0.15	0.6	2.4	3.13	19	0.99996
120	4.79	0.689	0.166	0.68	2.57	3.42	19.6	0.99996

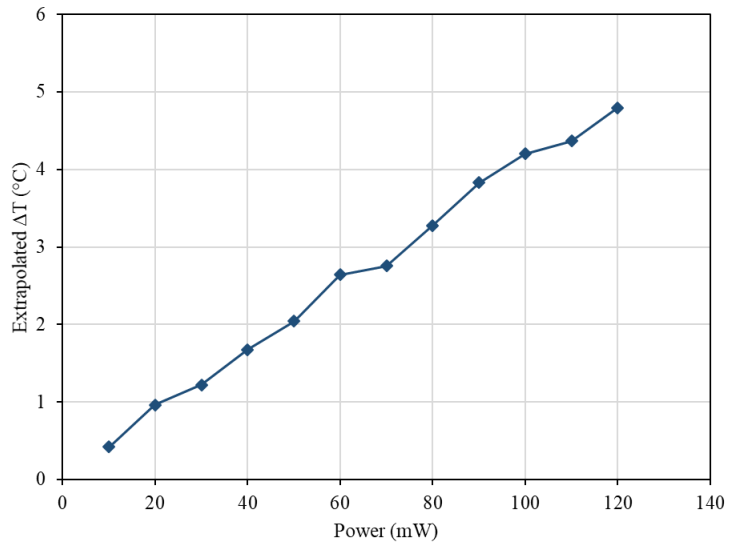


Figure 4-3. Steady state probe temperature according to heating power.

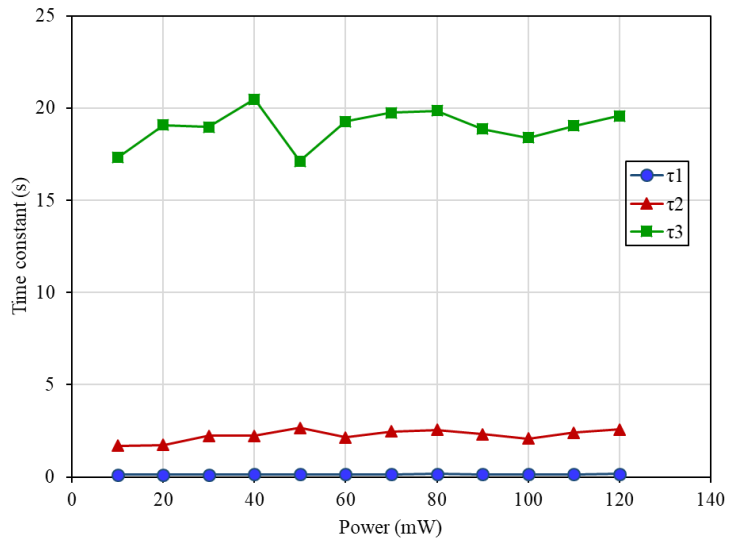


Figure 4-4. Change of time constant according to heating power.

4.2. Thermal characterization and calibration of microneedle

4.2.1. Calibration of microneedle probe

Thermal analysis and calibration of fabricated microneedle sensor for pipe flow and xylem flow were performed. A sensor was installed into the conduit, and the sensor signal was measured during water flow. The resistance of the sensor was 300 Ω , and a constant voltage of 4.5 V was applied to heat for 30 seconds at 67.5 mW. The correlation between the flow rate and the probe temperature was obtained using the lumped capacitance model (Equation 3-35). The curve fitting between the experimental results and the model was made using the least square method.

4.2.2. Pipe flow: calibration method

The correlation between measured signal and flow speed through a test tube was obtained to confirm that the sensor can quantitatively measure the flow rate in the pipe. Figure 4-5 shows the calibration setup for the microneedle sensor to measure the flow in a test tube. A precision syringe pump (KDS-100, KD Scientific) was used for controlling volumetric flow rate. The average flow speed inside the pipe was obtained from the applied volumetric flow rate. A silicone tube with 2 mm inner diameter was connected to the pump. The microneedle sensor was inserted radially into the tube. The position of the microneedle probe was manually adjusted. A 1.25-mm thick spacer was used to adjust vertical position of the sensor. The center of the pipe and the midplane of the sensor were aligned

(Figure 4-5 (b)). Isotonic saline water for plant sap (40 mOsm/L) was used as the calibration solution. The measured signals at known values of flow speed were fitted to obtain the parameters of the Equation 3-19.

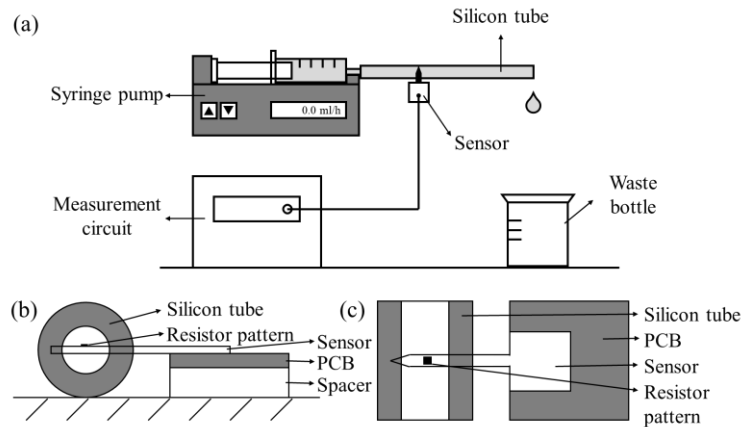


Figure 4-5. Calibration setup for microneedle sap flow sensor to measure the flow in the test tube (a). Position of sap flow sensor probe for pipe flow calibration. Vertical cross section view (b). Horizontal cross section view (c).

4.2.3. Pipe flow: thermal characterization

The thermal properties of the probe for pipe flow were evaluated. The flow rate was generated at 0, 1, 2, 3, 4 mm/s in a 2-mm inner diameter silicon tube using a syringe pump. The temperature of the probe was measured while the probe was generating heat at a constant power (Figure 4-6). Experimental results show that as the flow rate increases, the temperature rise of the probe decreases. As the flow rate increased, the probe temperature quickly converged to the steady-state temperature.

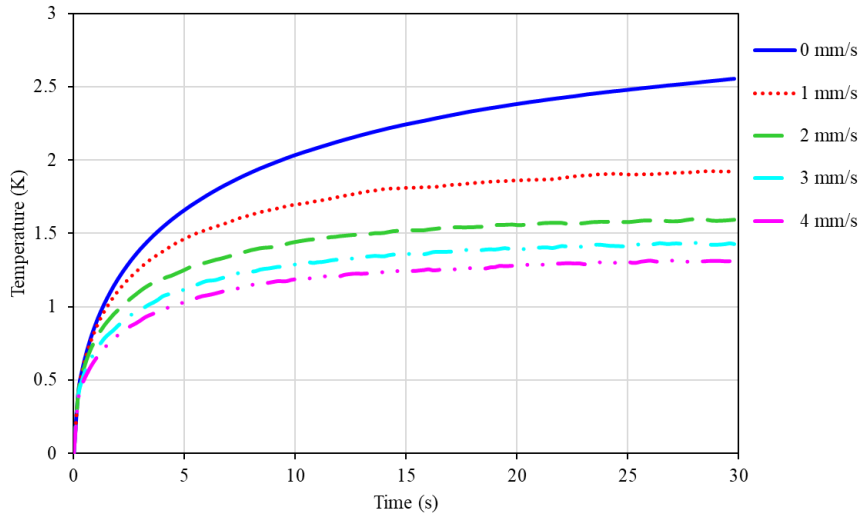


Figure 4-6. . Temperature change of heating probe for pipe flow by the flow speed.

For a more detailed analysis of the thermal phenomena, curve fitting of the temperature-time graph was performed based on the 3-component lumped capacitance model. Table 4-3 shows the result of curve fitting using Equation 3-35. As the flow rate increases, the steady-state heating temperature (T_M) decreases (Figure 4-7). Also, as the flow rate increases, the time constants τ_1 , τ_2 , and τ_3 decrease (Figure 4-8). The results were consistent with the correlation between the flow rate and probe temperature obtained from Equation 3-16. As supported by the coefficient of correlation, the curve fitting results were well fitted with the 3-component lumped capacitance model and simulation results.

Table 4-3. Curve fitting result of time-temperature graph of heating probe in pipe flow by flow speed based on 3-component lumped capacitance model.

Flow (mm/s)	T_M (°C)	A1 (°C)	τ_1 (s)	A2 (°C)	τ_2 (s)	A3 (°C)	τ_3 (s)	R^2
0	2.69	0.462	0.195	0.832	2.02	1.39	13.3	0.99993
1	1.94	0.440	0.173	0.686	1.60	0.814	8.39	0.99969
2	1.60	0.410	0.145	0.494	1.23	0.694	6.89	0.99976
3	1.40	0.380	0.123	0.342	1.06	0.679	5.58	0.99978
4	1.27	0.324	0.092	0.295	0.85	0.655	4.93	0.99986

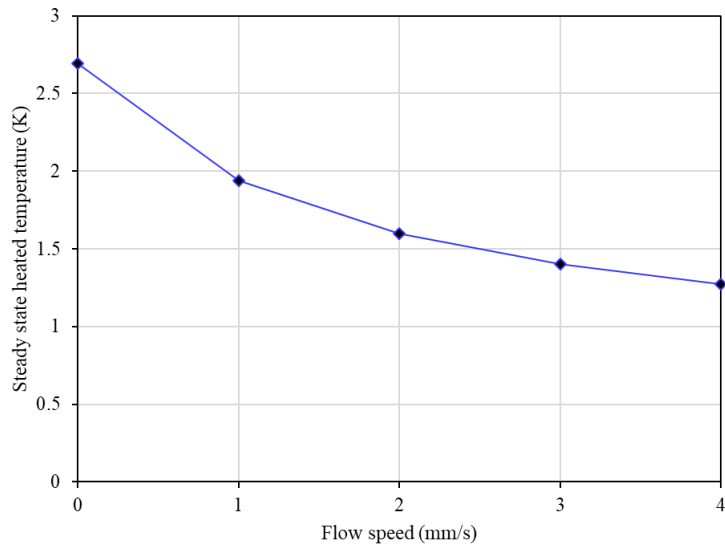


Figure 4-7. Flow speed – steady state heated temperature graph for pipe flow.

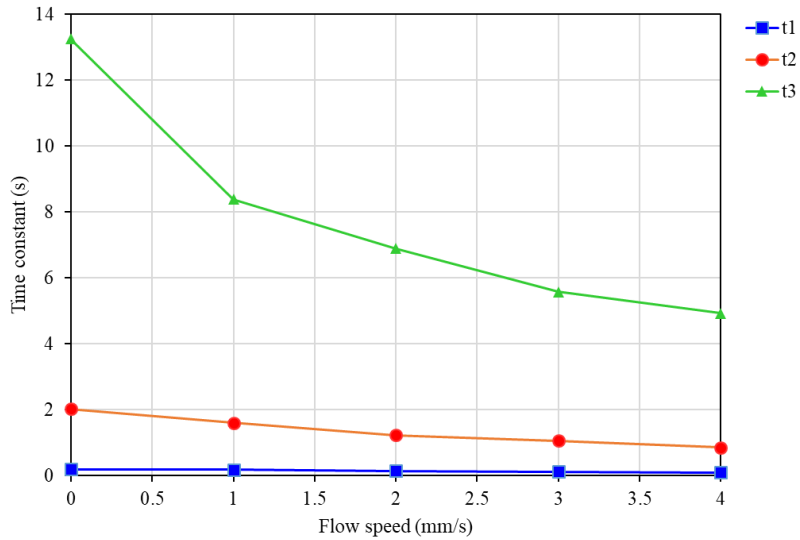


Figure 4-8. Flow speed–exponential dissipation time constant graph for pipe flow.

4.2.4. Pipe flow: calibration result

The sensor signal was measured while the average flow speed inside the tube was varied from 0 to 4 mm/s in five steps. The measurement was repeated 10 times per each flow speed step. The temperature difference, ΔT , between the heated and the unheated state, was measured. Figure 4-9 shows the temperature difference (ΔT) with flow rate. Equation 4-2 is the result of curve fitting using Equation 3-21 for the correlation between flow velocity and temperature change.

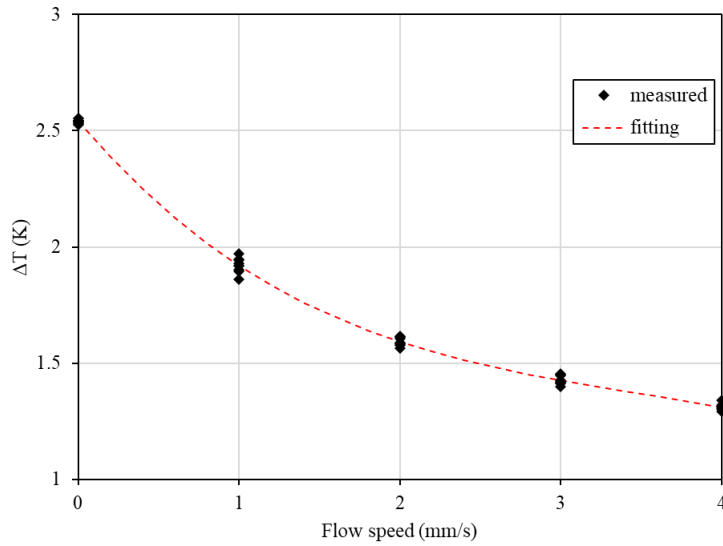


Figure 4-9. Relation between flow speed and temperature difference of probe (ΔT) in pipe flow.

$$T_{pipe,u} = (0.394 + 0.132 \cdot u^{0.763})^{-1} \text{ (}^\circ\text{C)} \quad (4-2)$$

Then a dimensionless flow index, $\frac{\Delta T_M - \Delta T}{\Delta T}$, was obtained where ΔT_M was the temperature difference at zero flow speed. Figure 4-10 shows the relationship between the flow speeds and the flow indices. This relationship was fitted to Equation 3-24 to obtain the following equation:

$$u_{pipe} = 4.28 \cdot \left(\frac{T_{u=0} - T}{T} \right)^{1.39} \text{ (mm/s)} \quad (4-3)$$

The coefficient of determination (adjusted R^2) for this fitting was 0.993.

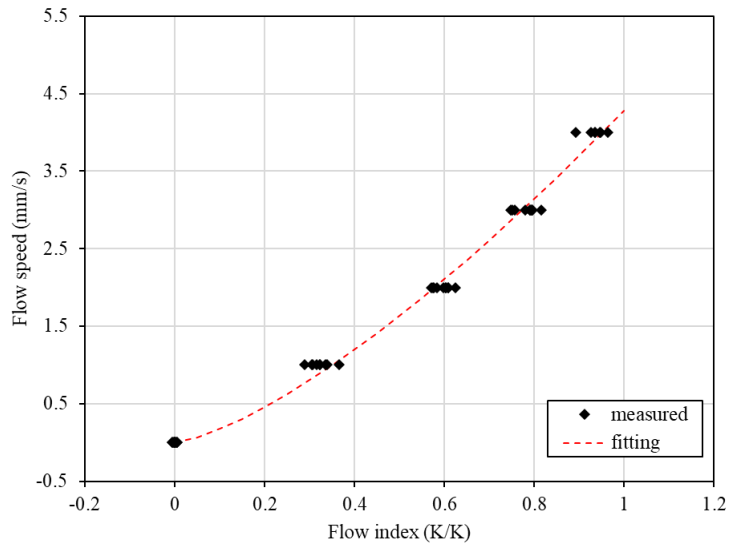


Figure 4-10. Relation between flow index $\left(\frac{\Delta T_M - \Delta T}{\Delta T}\right)$ and flow speed in pipe flow.

To verify the calibration results (Equation 4-3), the flow rates of the pipe flows were measured and compared to known flow rates (Figure 4-11). The microneedle sensor was able to measure the instant change in flow rate for the flow in the conduit. The the flow rate applied to the pipe using a syringe pump and the flow rate measured using a microneedle sensor were compared (Figure 4-12). As a result of the comparison, it was confirmed that the flow velocity and the measured flow velocity coincided with each other. The root mean square error of the measured flow speed was 0.115 mm/s in the tested range. It is postulated that the error was influenced by factors such as short-term ambient temperature fluctuation and inaccuracy in microneedle insertion depth.

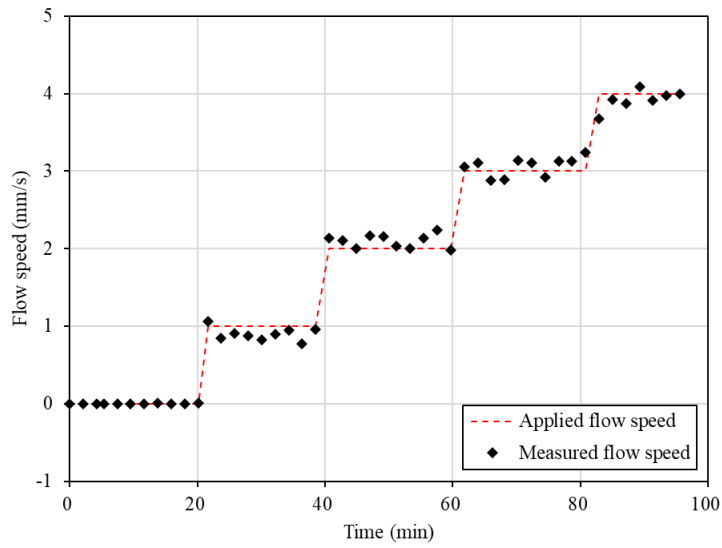


Figure 4-11. The response of microneedle sap flow sensor to the applied pipe flow speed.

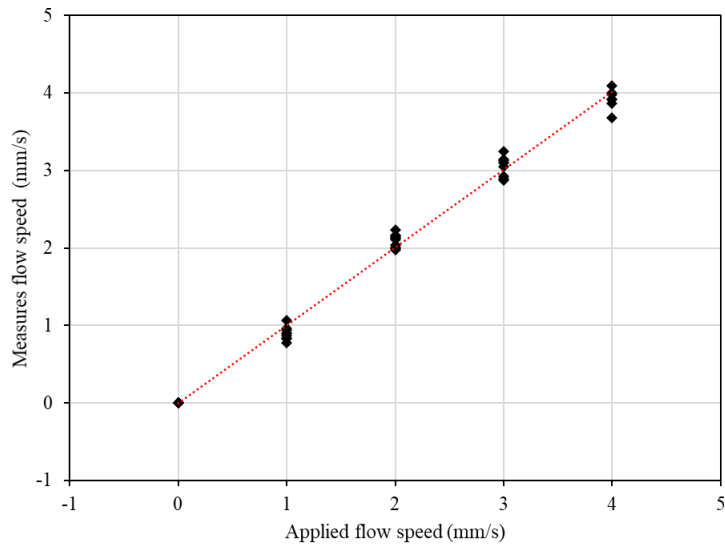


Figure 4-12. Comparison between the applied water flow speed in pipe and measured flow speed from sap flow sensor.

4.2.5. Xylem flow: calibration method

The response of the sensor to the xylem flow was expected to be different from the response to the pipe flow because the heat transfer in the plant xylem is a conjugated heat transfer where conduction and convection occur simultaneously in the vascular bundles. The calibration procedure was applied to a plant stem to analyze the correlation between the measured signal and the xylem flow (Figure 4-13). A tomato stem sample of 5 cm in length and 2 cm in diameter was collected from a greenhouse. A Mariotte-based test system was used for the calibration [1]. The Mariotte's bottle connected to the stem segment delivered a constant flow. An isotonic saline solution (40 mOsm/L NaCl solution) was prepared and used to prevent xylem bundle deformation due to osmotic pressure during the testing [2]. Two glass columns were inserted into an Erlenmeyer flask. One of the columns was connected the plant segment through a silicon tubing. The column and the tubing were filled with the solution and functioned as a siphon. The height of the Erlenmeyer flask was adjusted to control the hydraulic pressure applied to the plant segment, resulting in varied flow rate. The weight of solution flown through the plant segment was measured with a digital scale (HS-400L, Hansung). The xylem was stained with 0.1 wt.% crystal violet solution [3] after the whole measurement to obtain the cross-sectional area. The picture of stem cross section was taken with a digital camera and the area of the xylem was obtained with image processing program (ImageJ, NIH) (Figure 4-14). The gravimetric mass flow rate through plant stem is obtained from the weight increase of scale per unit time. The average flow speed of xylem flow is obtained by dividing the mass flow rate by the density of solution and cross-sectional area of xylem. The average xylem flow

speed is used as the calibration standard.

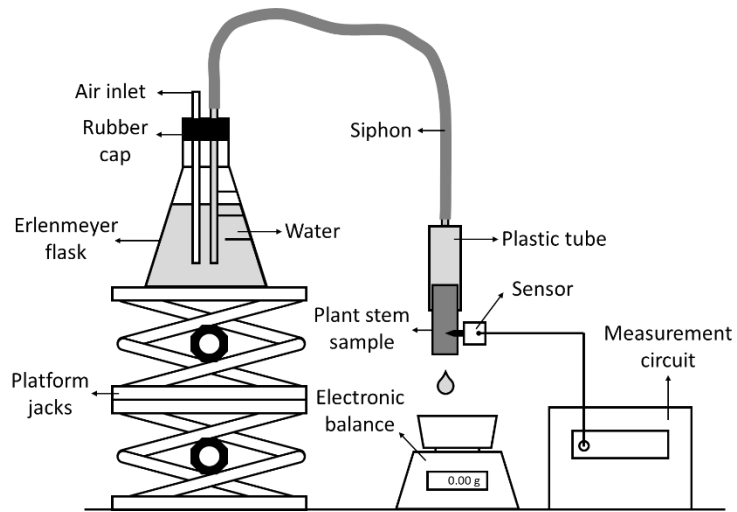


Figure 4-13. Calibration setup of microneedle sap flow sensor for xylem flow.



Figure 4-14. Cross section of tomato plant stem. The xylem is stained with crystal violet solution.

4.2.6. Xylem flow: thermal characterization

The thermal properties of the probe for flow in the xylem were evaluated. Hydrostatic pressure was applied with Mariotte's bottle into a tomato stem sample of 5 cm in length and 2 cm in diameter. The hydrostatic pressure applied to the sample was increased from 0 cmH₂O to 60 cmH₂O in 10 cmH₂O interval. The temperature of the probe was measured while the probe was generating heat at a constant power (Figure 4-15). Experimental results show that as the flow rate increases, the temperature rise of the probe decreases. As the flow rate increased, the probe temperature quickly converged to the steady-state temperature.

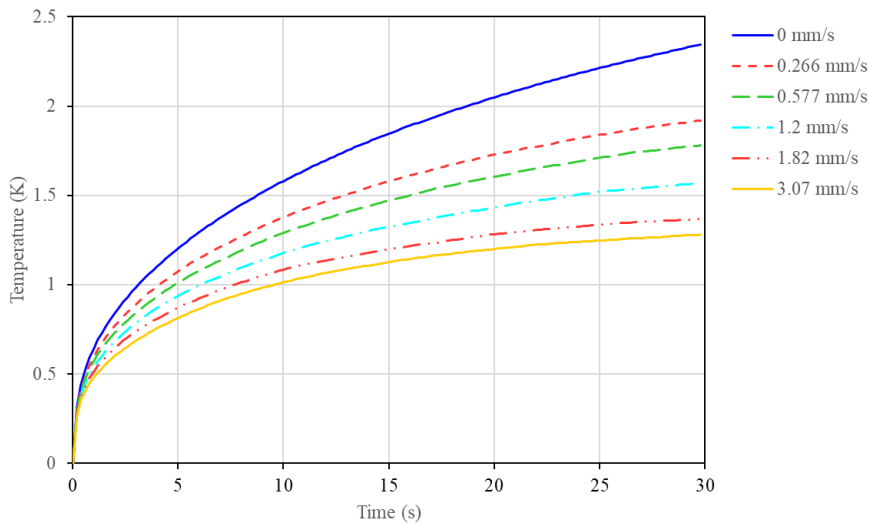


Figure 4-15. Temperature change of heating probe in xylem flow by flow speed.

Based on the 3-component lumped capacitance model obtained from Equation 3-35, the curve fitting of the temperature-time graph was performed. Table 4-4 shows the curve fitting result of time-temperature graph and the 3-component lumped capacitance model. As the flow rate increases, the steady-state heated

temperature decreases (Figure 4-16). As the flow rate increases, the time constants τ_1 , τ_2 , and τ_3 decrease (Figure 4-17). When the flow rate was 0.266 mm/s, the time constant was lower than the time constant when the flow rate was 0.577 mm/s, which was judged to be an error caused by the change in ambient temperature. The curve fit results were consistent with the 3-component lumped capacitance model and simulation results.

Table 4-4. Curve fitting result of time-temperature graph of heating probe in xylem flow by flow speed based on 3-component lumped capacitance model.

Flow (mm/s)	T_M (°C)	A1 (°C)	τ_1 (s)	A2 (°C)	τ_2 (s)	A3 (°C)	τ_3 (s)	R^2
0	2.85	0.399	0.217	0.445	2.33	2.00	21.7	0.99997
0.266	2.16	0.356	0.194	0.380	1.91	1.42	16.7	0.99997
0.577	2.01	0.366	0.195	0.352	2.11	1.29	17.2	0.99996
1.2	1.74	0.342	0.190	0.356	2.17	1.04	16.2	0.99999
1.82	1.45	0.342	0.186	0.299	2.18	0.80	12.6	0.99986
3.07	1.33	0.318	0.172	0.243	2.00	0.77	11.4	0.99995

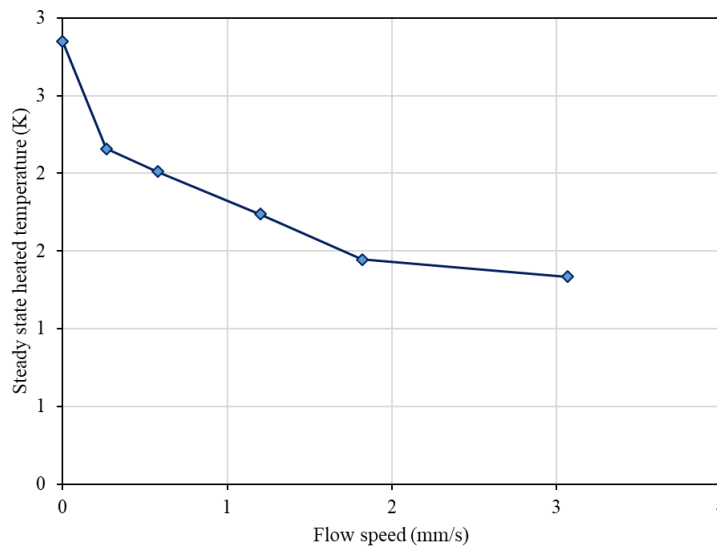


Figure 4-16. Flow speed – steady state heated temperature for xylem flow.

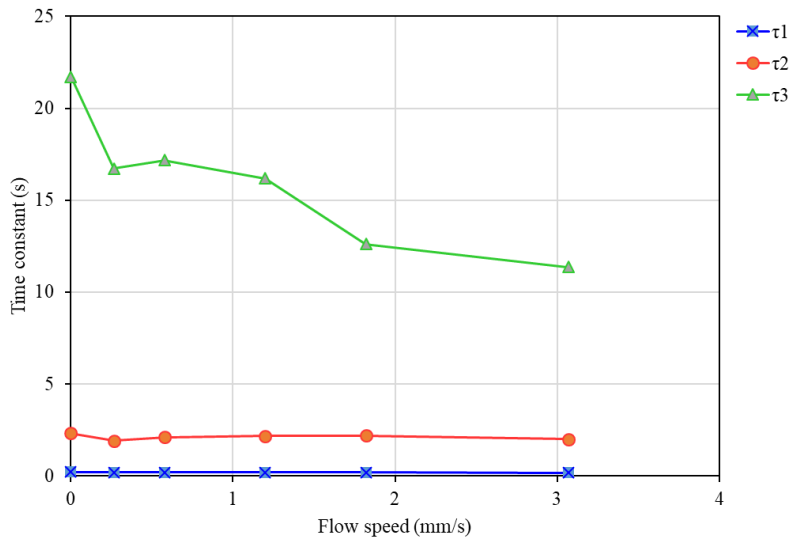


Figure 4-17. Flow speed – exponential dissipation time constant plot for xylem flow.

4.2.7. Xylem flow: calibration result

The measurement was carried out at six different flow speeds from 0 to 3.07 mm/s. Each measurement was repeated 30 times for each flow speed. The temperature difference between the heated and the unheated state (ΔT) was measured. Figure 4-18 shows the temperature difference (ΔT) according to the flow rate. Equation 4-4 is the result of curve fitting for the correlation between flow velocity and temperature change using Equation 3-21.

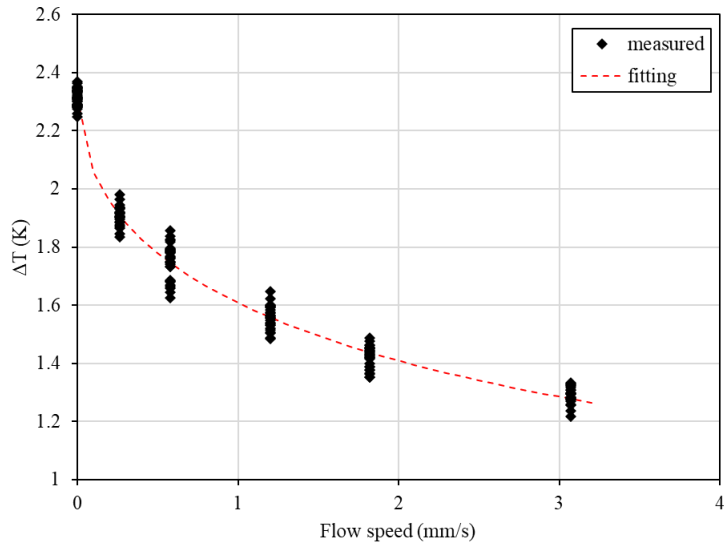


Figure 4-18. Relationship between flow speed and temperature difference of probe (ΔT) in xylem flow.

$$T_{xylem,u} = (0.432 + 0.190 \cdot u^{0.546})^{-1} \text{ (}^\circ\text{C)} \quad (4-4)$$

The measured signal was converted to the dimensionless flow index (Figure 4-19). We obtained the correlation between the xylem flow speed and the flow index as follows:

$$u_{xylem} = 4.46 \cdot \left(\frac{T_{u=0} - T}{T} \right)^{1.83} \text{ (mm/s)} \quad (4-5)$$

The adjusted R square value for fitting was 0.967.

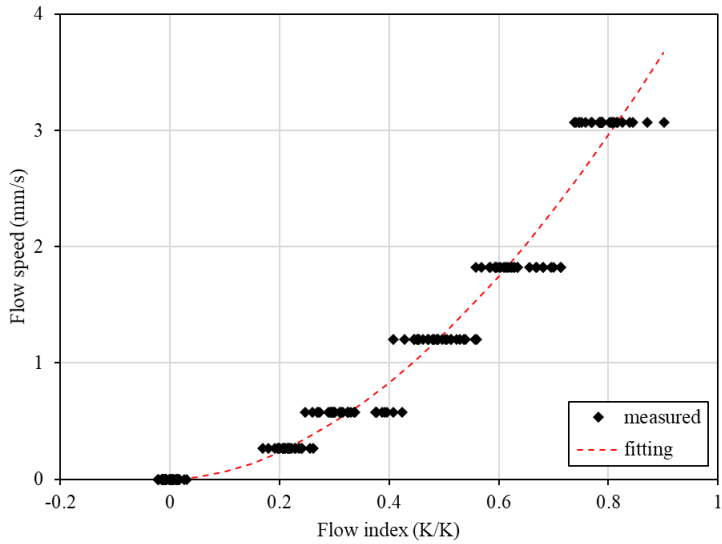


Figure 4-19. Relation between flow index $\left(\frac{\Delta T_M - \Delta T}{\Delta T}\right)$ and flow speed in xylem flow.

The flow speed inside xylem was estimated using Equation 4-5 and compared with the actual flow speed (Figure 4-19). The root mean square error of measured flow speed was 0.128 mm/s in the tested range.

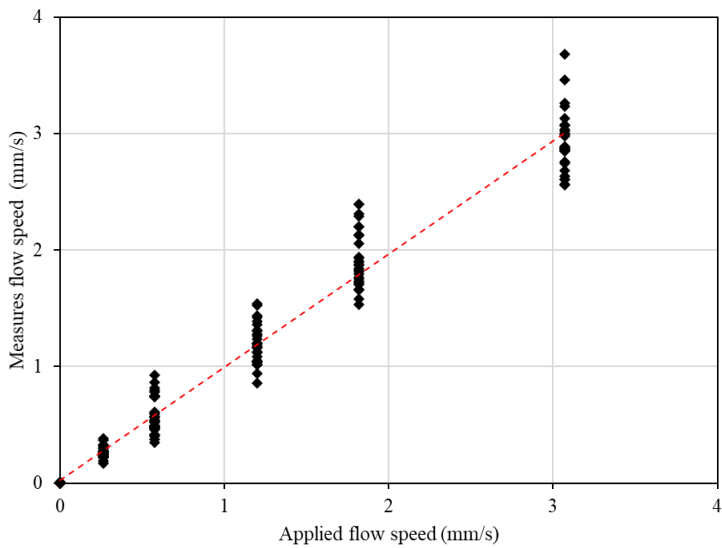


Figure 4-20. Comparison between the applied water flow speed in xylem and measured flow speed from sap flow sensor.

4.2.8. Comparison between calibration for pipe and calibration for xylem flow

The calibrations with the silicone tube and the plant xylem resulted in some discrepancy in parameters as in Equation 4-3 and Equation 4-5. The major contribution to this discrepancy comes from the different modes of heat transfer in the tube and in the xylem. The probe inserted into the silicone tube is completely surrounded by the fluid flow, and the convective heat transfer was dominant. On the other hand, the probe in the xylem is in contact with the plant tissue, and some conductive heat “leakage” should occur. The convection signal correlated with the flow is affected by this uncorrelated background conduction. This effect is more pronounced at lower flow speeds as evidenced by the graphs in Figure 4-10 and Figure 4-18. The flow speed tends to be overestimated at low values, e.g., ~ 1 mm/s, when the xylem calibration is compared with that of the tube.

There are additional uncertainties that contribute to the inaccuracies in the xylem flow measurement. The xylem consists of many vessel bundles with different sizes and connections that are subject to non-uniform flow speed as discussed in previous works [4]. The sensor pattern can be placed in different parts of the stem and the xylem bundle, leading to flow variations. In an extreme case, the pattern can contact either the pith or the phloem where the flows are very weak or uncorrelated with the xylem sap. Even in the xylem such flow will not remain exactly the same across the whole area. The xylem structure will be different among different species as well. Granier proved that the same calibration model can be used for different species of similar stem tissues with a reasonable scattering as far as the probe accessed the xylem area [5].

4.3. Conclusion

The accuracy of the sensor was confirmed and quantitated from the pipe flow calibration with well-defined system. The thermal characteristic and calibration curve of microneedle sap flow sensor was obtained for pipe flow. The thermal characteristic of microneedle was well fitted with that transfer model. The adjusted R^2 value with our pipe calibration was 0.993. The root mean square error of the measured flow speed was 0.115 mm/s.

In order to measure the sap flow of a 'real plant', additional calibration for xylem flow was necessary for field application. The plant xylem consists of many vascular bundles that is substantially different in heat transfer compared with a simple plastic tube. Thus the response of the sensor to the xylem flow should be different from the response to the pipe flow. The thermal characteristic and calibration curve of microneedle sap flow sensor were obtained for xylem flow. The heat transfer parameters and calibration curve of the sensor in xylem flow were different from those in pipe flow, and the difference was explained in terms of heat transfer model.

Bibliography

- [1] K. Steppe, D. J. W. De Pauw, T. M. Doody, and R. O. Teskey, "A comparison of sap flux density using thermal dissipation, heat pulse velocity and heat field deformation methods," *Agricultural and Forest Meteorology*, vol. 150, no. 7, pp. 1046-1056, 2010.
- [2] B. J. Atwell, *Plants in action: adaptation in nature, performance in cultivation*. Macmillan Education AU, 1999.
- [3] S. E. Ruzin, *Plant microtechnique and microscopy*. Oxford University Press New York, 1999.
- [4] A. E. Dimond, "Pressure and Flow Relations in Vascular Bundles of the Tomato Plant," *Plant Physiology*, vol. 41, no. 1, pp. 119-131, 1966.
- [5] A. Granier, "Une nouvelle méthode pour la mesure du flux de sève brute dans le tronc des arbres," *Ann. For. Sci.*, vol. 42, no. 2, pp. 193-200, 1985.

Chapter 5. In-Vivo Measurement of Microneedle Sap Flow Sensor

5.1. Measurement of sap flow by artificial light

5.1.1. Artificial light experiment method

To determine whether the sensor was able to measure the sap flow of a real plant, and to confirm the short-term measurement result, the response of the sap flow of a tomato plant to the artificial light was measured. The experiment was made in the Gwanak greenhouse (Figure 5-1). Tomato seeds were sown on a rock wool cube and grown for over 60 days. The plant was installed in an artificial light experiment chamber. The size of experiment setup was 60 * 60 * 120 cm. Two 300 W halogen lamps were installed at 100 cm height. During the experiment, the temperature was maintained at 21°C and the humidity was maintained at 40%. The sensor was installed 10 cm above the ground. The sap flow of tomato and internal relative temperature of tomato stem were measured with the microneedle sensor. The process of turning on and off the lamp for a total of 12 hours of experiment was repeated three times. The light was illuminated three times during a total of 12 hours of experimentation.



Figure 5-1. Experiment setup for artificial light illumination test.

5.1.2. Result of artificial light experiment

Experimental results showed that the relative temperature inside the plant and sap flow in the plant have a direct and immediate response to artificial light irradiation (Figure 5-2, 3). At the start of the experiment, and the external light was blocked for about two hours. During this time, the plant's transpiration by the light discontinued and the sap flow was stabilized at about 0.25 mm/s to 0.1 mm/s. The experiment was carried out in the covered artificial light box in the first trial. Two lamps were turned on at 14:00. The relative temperature of the plant rose rapidly as the lamp was turned on (Figure 5-2). One hour after the lamp was turned on, the temperature in the plant rose by 3°C. The sap flow rate of the plant began to increase after about 5 minutes of light illumination (Figure 5-3). The sap flow was initially at 0.0 mm/s and reached the maximum sap flow rate of 0.5 mm/s after

one hour. The cover was removed and the lamp was turned off at 15:00. The temperature in the plant began to decrease rapidly. The temperature in the plant returned to its original temperature in one hour. The sap flow rate simultaneously decreased to 0.0 mm/s. An unusual phenomenon was observed during the sap flow measurement. After the lamp was turned on, the sap rate dropped for about 5 minutes. And after the lamp was turned off the sap flow rate spiked for about 5 minutes. This phenomenon is contributed to the artificial temperature gradient (ATG) due to the external temperature change. The detailed description is covered later in Chapter 6. In the second trial, the lamp was irradiated after the cover was removed. The plant's internal temperature increased by 2.5°C within 30 minutes of irradiation. The maximum temperature was lower than the first trial because the cover was removed and ventilation was done. The sap flow rate increased from 0 mm/s to 0.2 mm/s. The artificial light was radiated for about two hours. Then the lamp was turned off and the temperature and sap flow of the plant decreased. After one hour, the temperature returned to its original temperature and the sap flow dropped to 0.0 mm/s. The artificial effect of the ATG was observed as in the first trial. A slight amount of sap flow was observed even after turning off the lights. During the artificial light illumination experiment, some degree of wilting was observed in the plant leaves due to sudden high energy radiation. It was judged that sap flow occurred to recover and hydrate the withered leaves. After a sufficient time, the third irradiation was carried out. The temperature increased by about 2.5°C and the sap flow increased from 0 mm/s to 0.2 mm/s. The lamps were turned off and the temperature and sap flow rate returned to the origin in an hour.

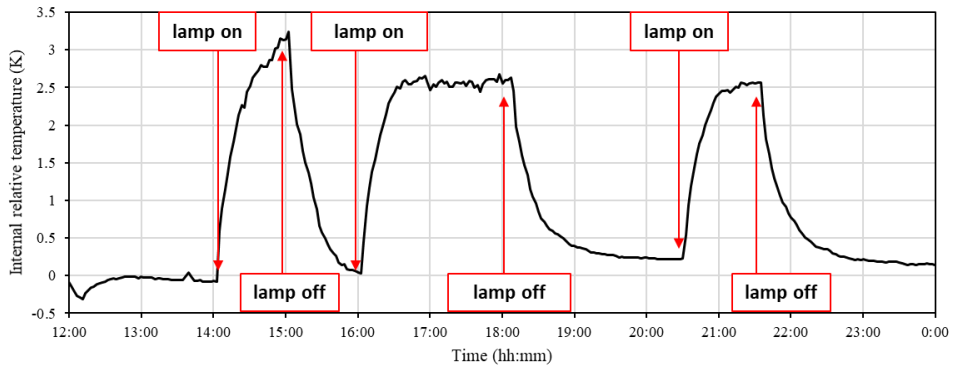


Figure 5-2. Measured internal relative temperature of tomato stem during the artificial light illumination test.

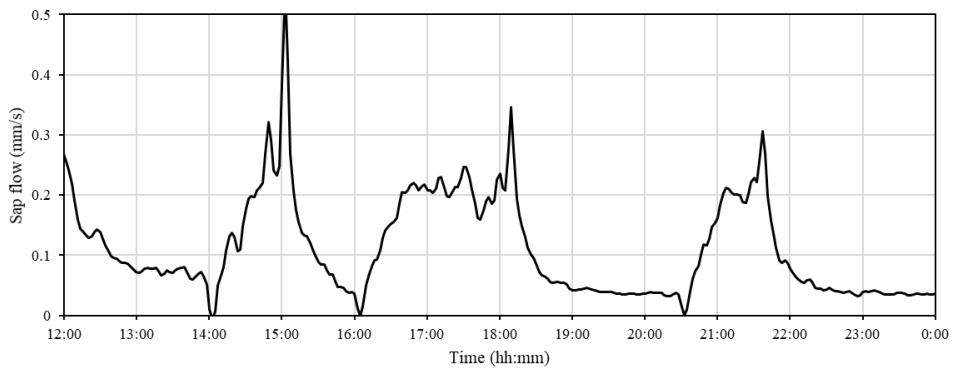


Figure 5-3. Measured sap flow of tomato stem during the artificial light illumination test.

5.1.3. Conclusion of artificial light experiment

The artificial light experiment confirmed that the microneedle flow sensor can measure the instantaneous bio signal change of a living plant. Immediate temperature changes within the plant were measured during the experiment. The instantaneous response of sap flow to the artificial light radiation was observed in

real-time. The response of the plant to the external light source occurred within 30 minutes, during which the sap flow rate varied from 0 mm/s to 0.2 mm/s. When the external light source was removed, the plants quickly regained their original state within an hour. Measurement errors in sap flow due to ATG effect were observed which will be covered later in Chapter 6.

5.2. In-vivo measurement of tomato plant

5.2.1. Field measurement method for tomato plant

The sap flow speeds of tomato plants were measured in a greenhouse. The test period was from June of 2016 to March of 2018 (Table 5-1). During the test period, 181 sensors were installed and total duration was 352 days. The experiment was undertaken in a glass greenhouse at the Protected Horticulture Research Institute, Haman, Gyeongsangnam-do, South Korea, located at latitude of 35°24'N and longitude of 128°42'E (Figure 5-4). Tomato seeds ('Dafnis', Synzenta Seeds) were sown in rockwool trays on May 20, 2017, and January 10, 2017. The seedlings with two to three leaves were planted in rockwool cubes (10 × 10 × 6.5 cm, UR Rockwool, Korea) sufficiently saturated with the standard nutrient solution for tomato plants (Glasshouse Crops Research and Experiment Station at Naaldwijk, Netherlands). The composition of the nutrient solution was as follows: 13.8 me l⁻¹ nitrate nitrogen (NO₃-N), 1.25 me l⁻¹ ammonium nitrogen (NH₄-N), 3.75 me l⁻¹ phosphorous (P), 8.75 me l⁻¹ potassium (K), 8.5 me l⁻¹ calcium (Ca), 4.0 me l⁻¹ magnesium (Mg), 7.5 me l⁻¹ sulfur (S), 0.84 ppm iron (Fe), 0.55 ppm manganese (Mn), 0.33 ppm zinc (Zn), 0.05 ppm copper (Cu), 0.33 ppm Boron (B), and 0.05 ppm molybdenum (Mo). The tomato seedlings were transplanted on February 8, 2017, in each rock-wool slab (100 × 20 × 10 cm, UR rock-wool, Korea) and were grown at a plant density of 1.3 m between rows and 0.25 m within-row spacing (3.08 plants m⁻²). A nutrient solution was supplied through a proportional control method of integrated solar radiation using a drip irrigation system (Netajet, Netafim Korea, Korea) after transplantation. Irrigation on and off hours were

modified depending on the daily sunrise and sunset times; irrigation began one hour after sunrise, and ended 1.5–2 hour before sunset. The volumetric water contents in the coir substrates was maintained between 60%–80% by managing the irrigation amounts per day and the nutrient solution was supplied at the EC of 2.3–2.5 mScm⁻¹ over the growing period. The environmental conditions, the temperature (°C), relative humidity (RH, %), vapor pressure deflection (VPD, kPa), solar radiation (Wm⁻²), and photosynthetically active radiation (PAR, μmolm⁻²s⁻¹) were monitored with sensors whose values were continually recorded every 10 min with the data logger (CR1000, Campbell Scientific, USA) located inside the greenhouse. The internal temperature in the greenhouse was maintained from 15°C to 29°C by hot water circulation of 80°C during the night and ventilation of top window by data logger (CR1000, Campbell Scientific, USA). Sensors were implanted into the tomato stems ~ 30 cm above the roots (Figure 5-4). The target depth of the installed sensors was 2.5 mm. The sap flow and internal relative temperature of tomato plants were measured from the microneedle sensor.



Figure 5-4. Picture inside the greenhouse at the Protected Horticulture Research Institute (left). Microneedle sap flow sensor installed on tomato plant stem (right).

Table 5-1. List of field experiments of microneedle sap flow sensor for tomato plant.

Subject	Period	Duration	# of sensors	Place
Tomato	2016-06-07 ~ 2016-06-16	10	8	Haman
Tomato	2016-10-25 ~ 2016-11-03	10	4	Haman
Tomato	2016-11-03 ~ 2016-11-14	12	4	Haman
Tomato	2016-12-06 ~ 2016-12-08	3	3	Haman
Tomato	2017-02-02 ~ 2017-02-05	4	4	Haman
Tomato	2017-03-02 ~ 2017-04-07	37	4	Haman
Tomato	2017-05-09 ~ 2017-06-11	34	12	Haman
Tomato	2017-07-25 ~ 2017-08-10	17	4	Haman
Tomato	2017-08-11 ~ 2017-08-29	19	32	Gwanak
Tomato	2017-09-22 ~ 2017-10-18	27	8	Haman
Tomato	2017-09-19 ~ 2017-11-10	53	32	Gwanak
Tomato	2017-09-30 ~ 2017-10-10	11	2	Gwanak
Tomato	2017-11-29 ~ 2018-01-31	64	32	Gwanak
Tomato	2018-02-01 ~ 2018-03-23	51	32	Gwanak

5.2.2. Long-term measurement of tomato plant in greenhouse

A long-term measurement experiment of microneedle sap flow sensor was conducted. The experimental period lasted from March 2nd to April 7th for 37 days. The purpose of the experiment was to verify the long-term measurement capability of the sensors installed on tomato plants. 16 sensors were installed on 8 tomato trees. Temperature, humidity, solar radiation, sap flow, and relative temperature in the plant were measured.

5.2.3. Result of long-term measurement of tomato plant in greenhouse.

Total 16 sensors were implanted and operated for 37 days. About 50% of

sensors survived during the test period. 6 out of 16 sensors survived throughout 36 days of experiment period. 7 out of 16 sensors failed due to mechanical breakage. The other 3 sensors failed due to the electrical breakdown. Figure 5-5, 6 shows the sap flow speed and internal relative temperature measured with one of the sensors in comparison with other environmental variables (Figure 5-7~9). Figure 5-10~14 shows enlarged measurement result for 5 days. One day's measurements in the second week of March were lost due to the communication failure. The sap flow speed directly reflects the diurnal cycle of the plant according to the air temperature and the solar radiation. After the sunrise on a sunny day, the sap flow rapidly rises as the solar radiation and air temperature increase. The sap flow reaches the maximum value at noon. The sap flow decreases as the sun sets around 6 p.m. A small amount of sap flow is visible during the night, driven by osmosis. The sap flow was low during cloudy and rainy days. It also represents the fine fluctuation of the solar radiation as well as the long-term increase as the plant grows and the solar radiation becomes stronger. When the sap flow is integrated over time for a day and multiplied by the annular area of the stem cross section, the daily transpiration of the plant is obtained. The internal temperature of the stem was affected by the external one as shown in Figure 5-6 and Figure 5-8. However, the internal temperature fluctuation was kept 1/10 of the external variation. This reveals the homeostatic behavior of the plant against the environmental impact.

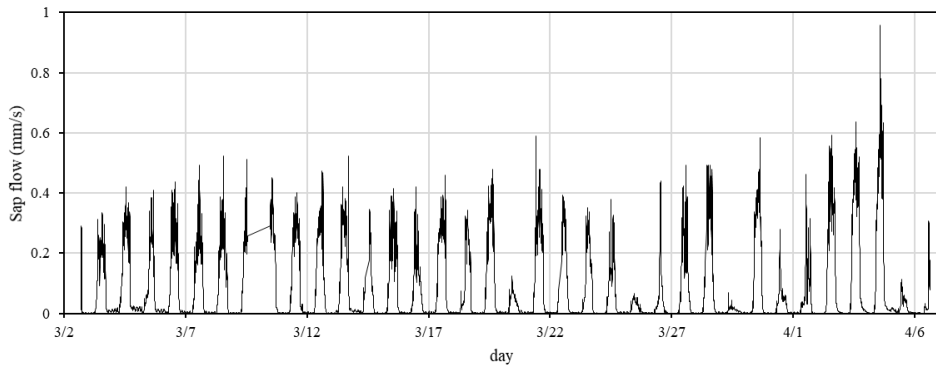


Figure 5-5. Sap flow speed of tomato stem during the long-term field measure test.

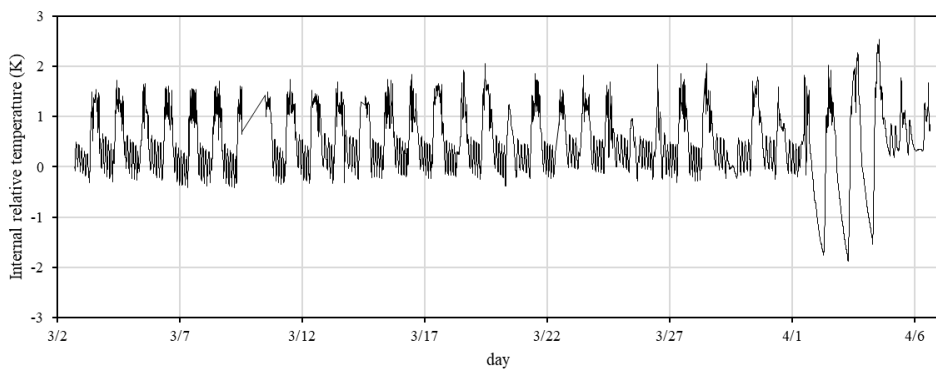


Figure 5-6. Internal relative temperature of tomato stem during the long-term field measure test.

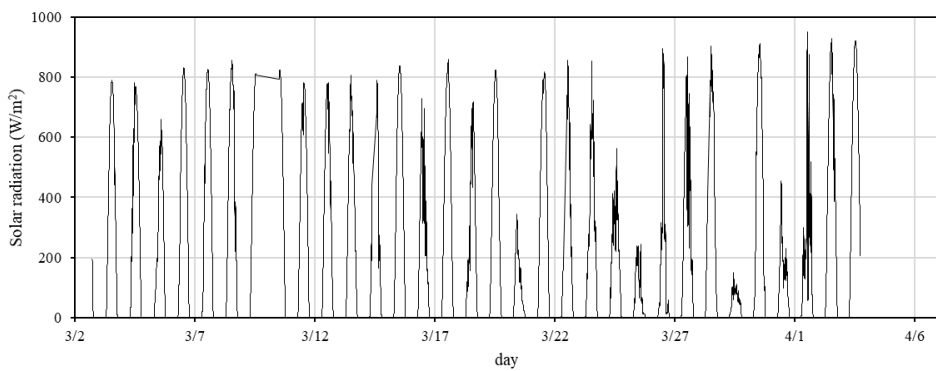


Figure 5-7. Solar radiation intensity inside the greenhouse during the long-term field measure test.

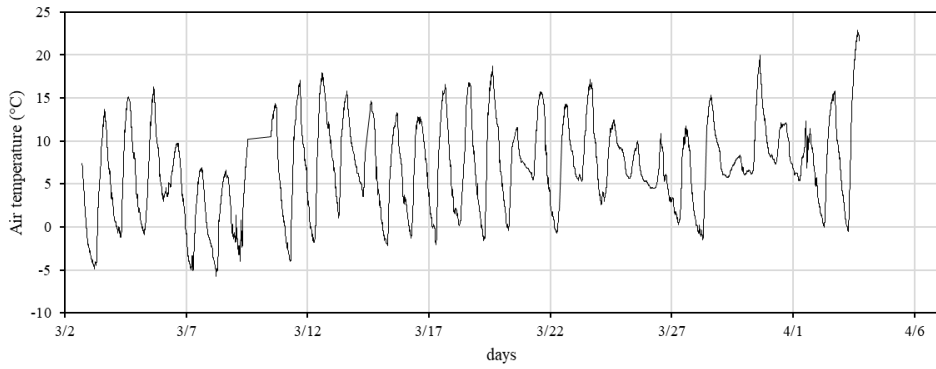


Figure 5-8. Ambient temperature inside the greenhouse during the long-term field measure test.

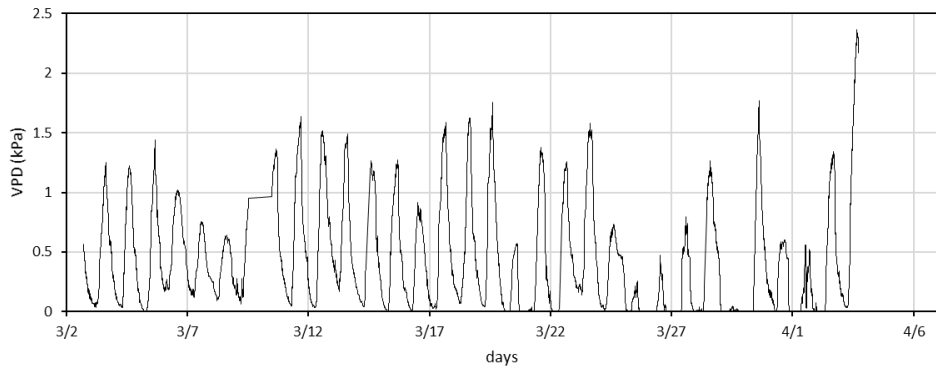


Figure 5-9. Vapor pressure deficit inside the greenhouse during the long-term field measure test.

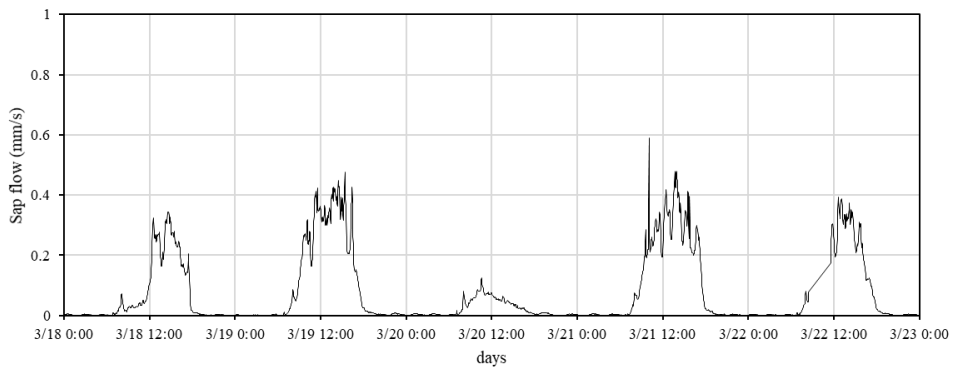


Figure 5-10. Sap flow speed of tomato stem from Mar. 18th to Mar. 23rd.

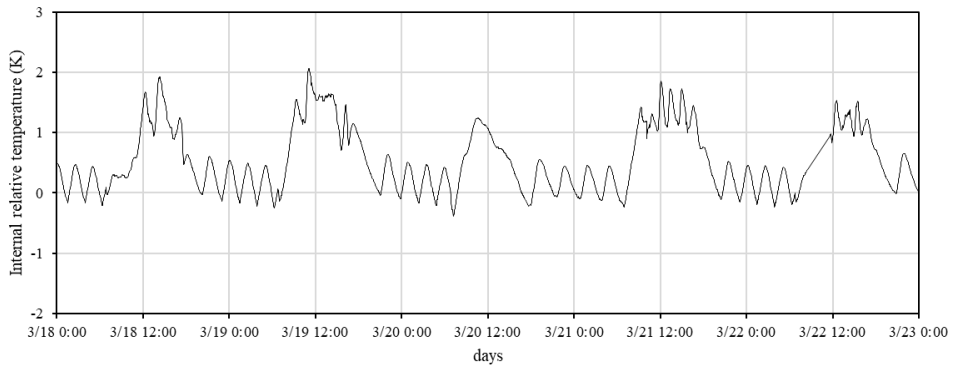


Figure 5-11. Internal relative temperature of tomato stem from Mar. 18th to Mar. 23rd.

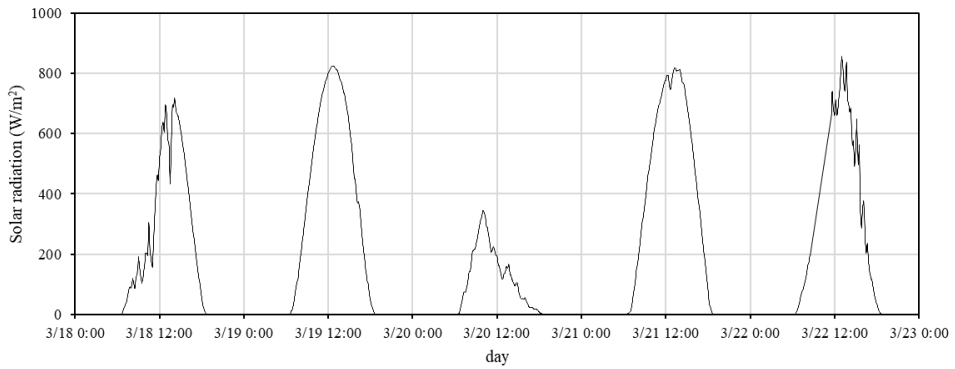


Figure 5-12. Solar radiation intensity inside the greenhouse from Mar. 18th to Mar. 23rd.

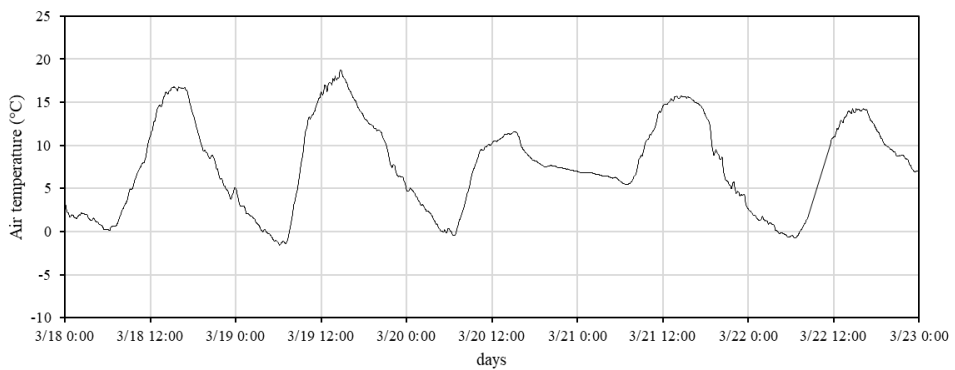


Figure 5-13. Ambient temperature inside the greenhouse from Mar. 18th to Mar. 23rd.

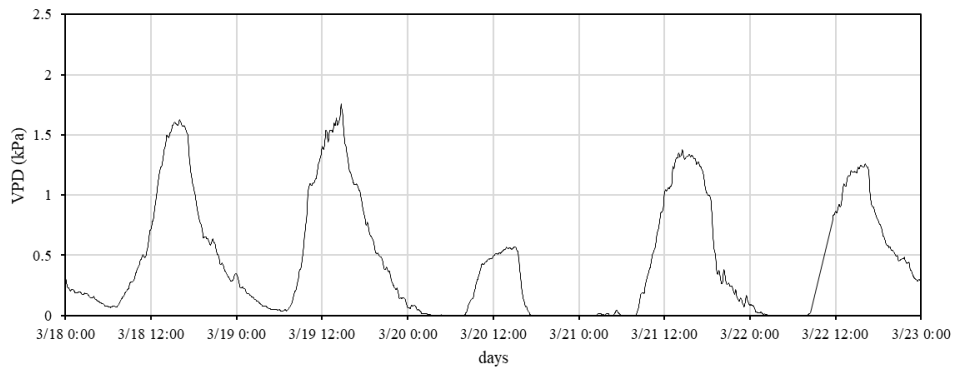


Figure 5-14. Vapor pressure deficit inside the greenhouse from Mar. 18th to Mar. 23rd.

5.2.4. Comparison between environmental variables and sap flow

Experiments were conducted to clarify the relationship between sap flow and environmental parameters. During the 34-day measurement from 2017 May 9th to June 11th, sap flow, relative temperature and light intensity, temperature, and VPD were measured and compared. 12 sensors were installed on 6 tomato trees.

5.2.5. Result of comparison between environment variables and sap flow

Figure 5-15 to 19 show enlarged measurement data on May 20th. As shown in the graph, the magnitude of the sap flow was closely correlated with the amount of light, temperature, and vapor pressure deficit (VPD).

However, in the time domain graph, the correlation between these variables is limited, and the environmental variables such as light quantity, temperature and humidity which are entangled with each other, which makes analysis difficult. Rather than analyzing the temporal variation in sap flow and environmental

variables, the correlation between environmental variables and sap flow at each time was directly analyzed.

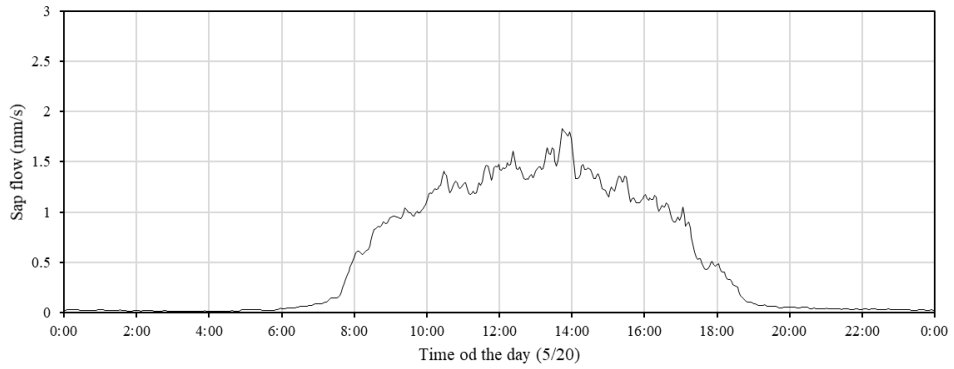


Figure 5-15. Sap flow speed of tomato stem on May 20th.

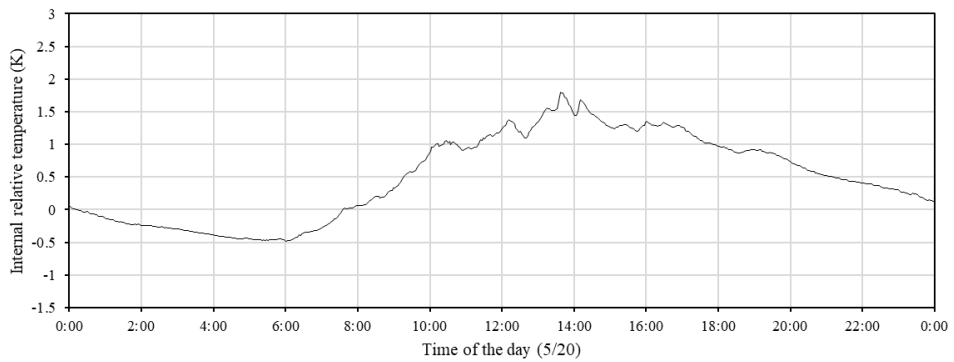


Figure 5-16. Internal relative temperature of tomato stem on May 20th.

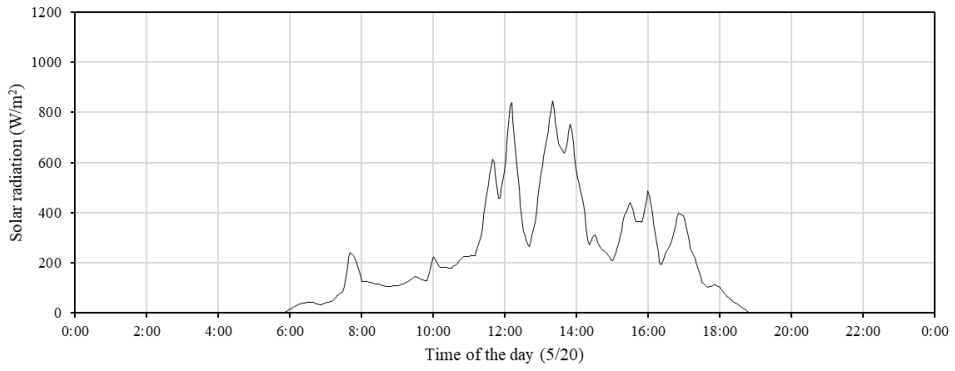


Figure 5-17. Solar radiation intensity inside the greenhouse on May 20th.

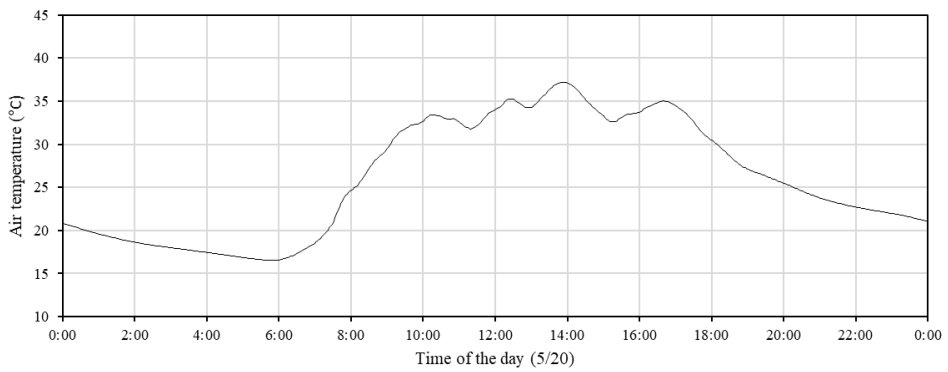


Figure 5-18. Ambient temperature inside the greenhouse on May 20th.

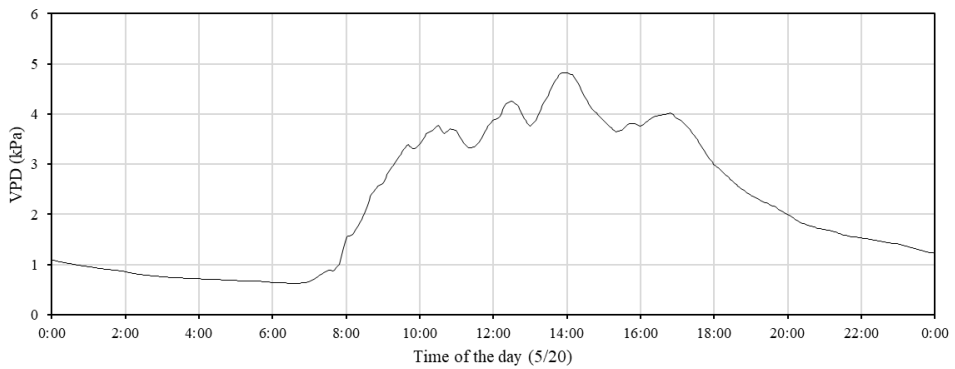


Figure 5-19. Vapor pressure deficit inside the greenhouse on May 20th.

Figures 5-20 ~ 22 show the changes in sap flow according to environmental variables. First, the correlation between fluid flow and solar radiation (Figure 5-

20) shows that the fluid flow is positively correlated with the solar intensity. In addition, the increase in sap flow tends to saturate as the solar radiation increases. Figure 5-21 shows the correlation between sap flow and air temperature. As the air temperature increases, the sap flow rate increases. However, when the air temperature decreases, the sap flow drops faster. Because of this, a hysteresis was observed in which the trajectory for the sap flow rise and the trajectory for the sap flow descend are different from each other. Correlation between sap flow and VPD also showed similar correlation with sap flow and air temperature (Figure 5-22). The correlation between sap flow and VPD was positively, and hysteresis of sap flow and VPD was observed.

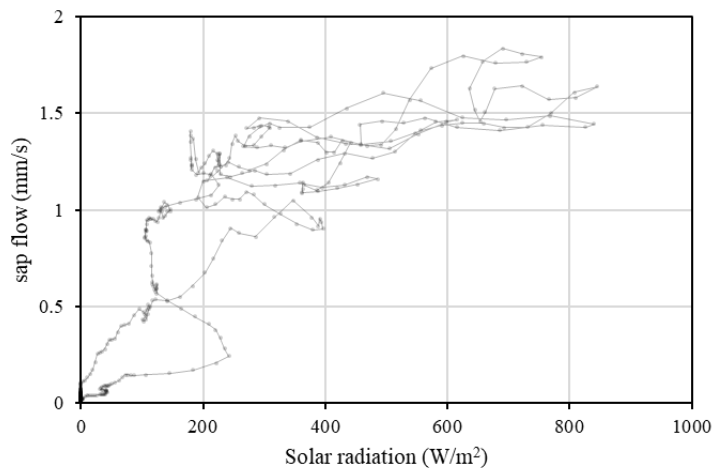


Figure 5-20. Comparison between solar radiation and sap flow on May 20th.

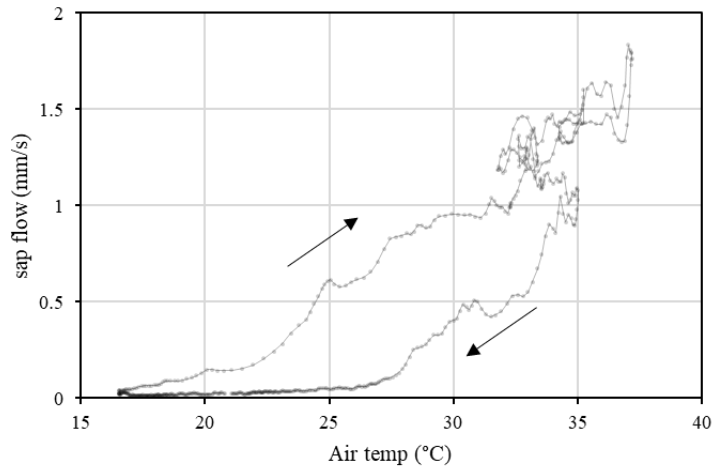


Figure 5-21. Comparison between air temperature and sap flow on May 20th.

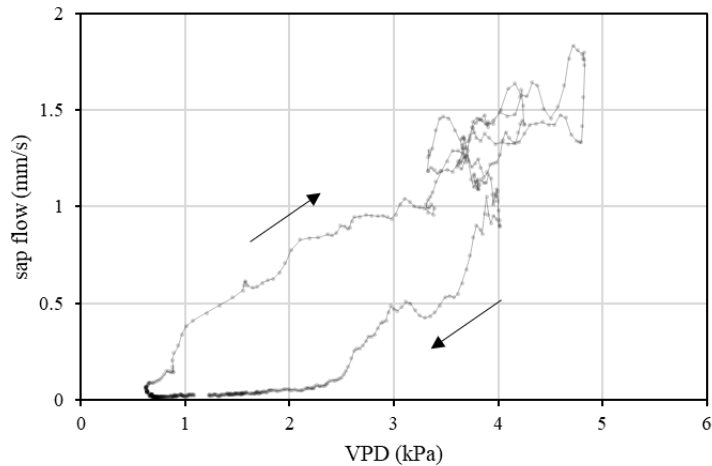


Figure 5-22. Comparison between vapor pressure deficit and sap flow on May 20th.

Two weeks of sap flow rate data and environment data were compared. The the environmental variables and the sap flow at each time is indicated by a dot (Figure 5-23 ~ 25). The data was compiled for two weeks from May 13th to May 26th. Interesting results were observed in the correlation between the sap flow and solar radiation (Figure 5-23). Sap flow rate rapidly increased when the solar radiation was 100 W/m^2 . The sap flow velocity did not exceed 1.5 mm/s even at

higher solar radiation. The graph shows that 100 W/m^2 is the threshold for transpiration and 1.5 mm/s is the upper limit of sap flow. the hysteresis of sap flow and air temperature was shown in Figure 5-24. Figure 5-25 shows that the slope of the sap flow is constant when the VPD increases. Hysteresis of sap flow by VPD was also observed.

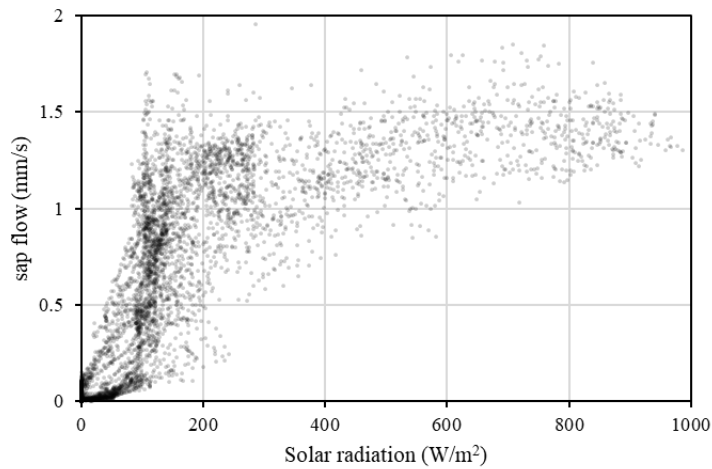


Figure 5-23. Comparison between solar radiation and sap flow from May 13th to May 26th.

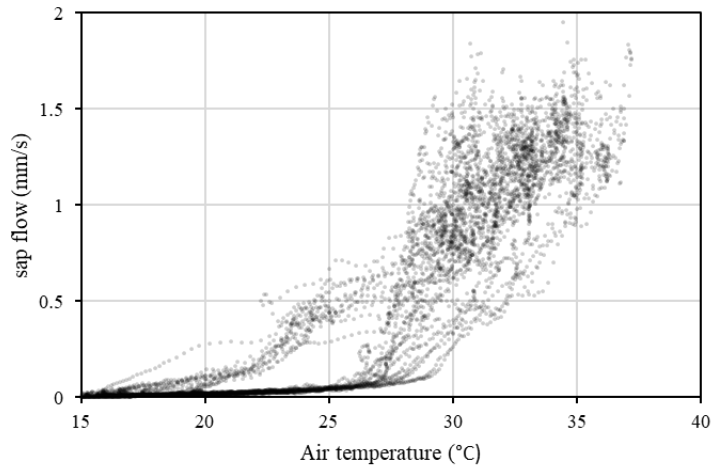


Figure 5-24. Comparison between air temperature and sap flow from May 13th to May 26th.

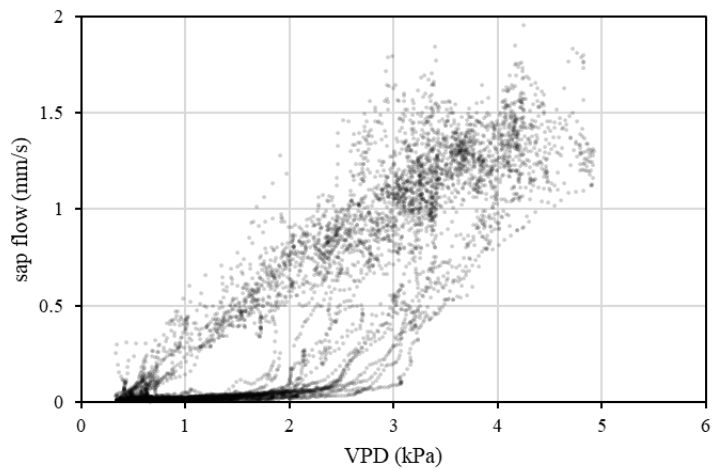


Figure 5-25. Comparison between VPD and sap flow from May 13th to May 26th.

5.2.6. Irrigation cut test

An irrigation cut-off experiment was conducted to observe the reaction of sap

flow when the irrigation was stopped during the plant cultivation. The experiment period was from 2017 September 22nd to October 18th. The interruption of the irrigation took place on October 1st. The interruption of the irrigation was done by removing the irrigation tube from the culture medium. Eight sensors were installed on four tomato plants. Irrigation of two tomato plants was interrupted. The other two tomato plants were control subjects with regular irrigation. Biometric information and environmental parameters of the plant were measured during the experiment.

5.2.7. Result of irrigation cut test

Figure 5-26 shows the sap flow rate in a tomato plant with irrigation cut. The amount of sap flow has decreased since October 1st, when irrigation has been cut. Figure 5-27 shows the sap flow of the control subject. The amount of sap flow rate of the control subject was relatively larger than the result of Figure 5-26. Figures 5-28 and 5-29 show the solar radiation and air temperature during the measurement period.

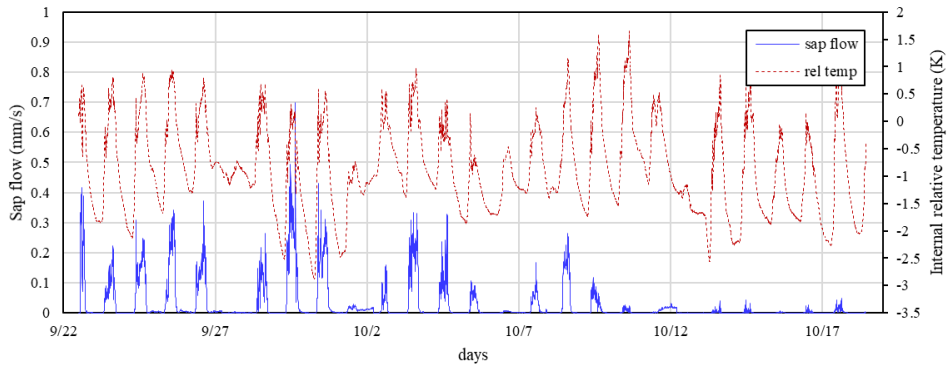


Figure 5-26. Sap flow and internal relative temperature of experimental group. The irrigation was cut on Oct. 1st.

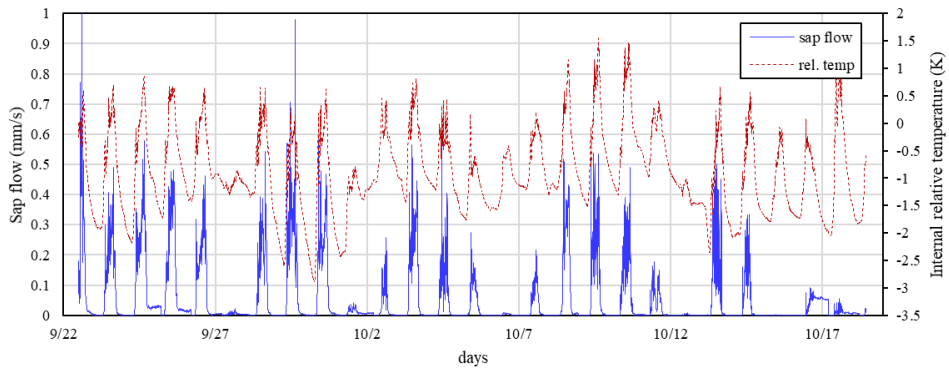


Figure 5-27. Sap flow and internal relative temperature of control group.

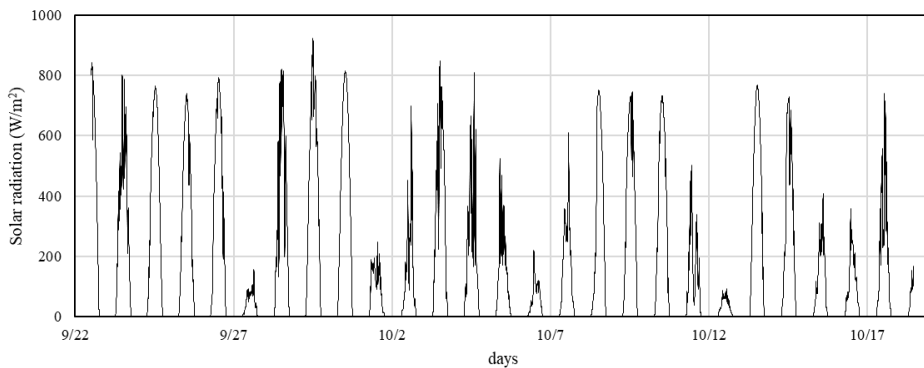


Figure 5-28. Solar intensity inside the greenhouse during the experiment period.

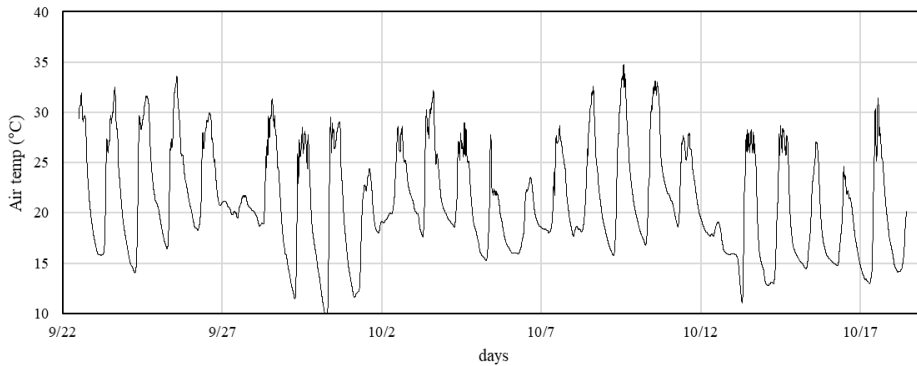


Figure 5-29. Air temperature inside the greenhouse during the experiment period.

Since the amount of sap flow is affected not only by the amount of irrigation but also by the solar radiation, the amounts of solar radiation and sap flow are compared for accurate analysis. The integrated value of sap flow amount per day (daily watering) and the daily integrated solar radiation (daily solar) were compared. The amount of daily watering was proportional to the amount of daily solar when regular irrigation occurred. However, after the irrigation cut, daily watering dropped regardless of the daily solar (Figure 5-30). On the other hand, the amount of daily watering was proportional to the daily solar radiation for the control subject (Figure 5-31).

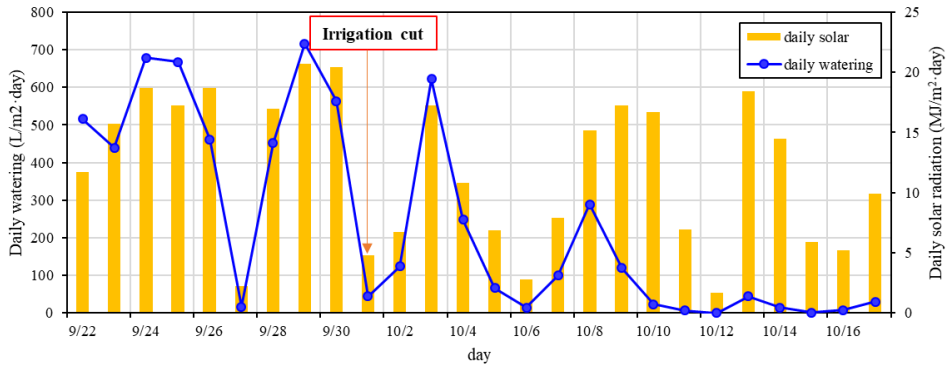


Figure 5-30. Comparison between daily watering and daily integrated solar radiation for experimental group.

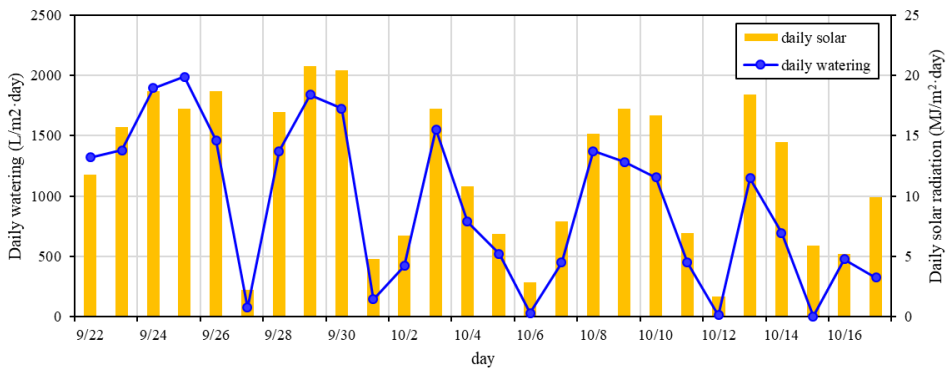


Figure 5-31. Comparison between daily watering and daily integrated solar radiation for control group.

5.2.8. Mass population measurement of sap flow signal

In order to observe the distribution of the sensor signals when more than 32 sensors are installed and to observe the sensor signals statistically, a mass measurement of sap flow was made. The experimental period was from 2018

February 1st to March 23rd, 51 days. 32 sensors were installed on 32 tomato plants.

Figure 5-32 shows the measured 32 sensor signals simultaneously.

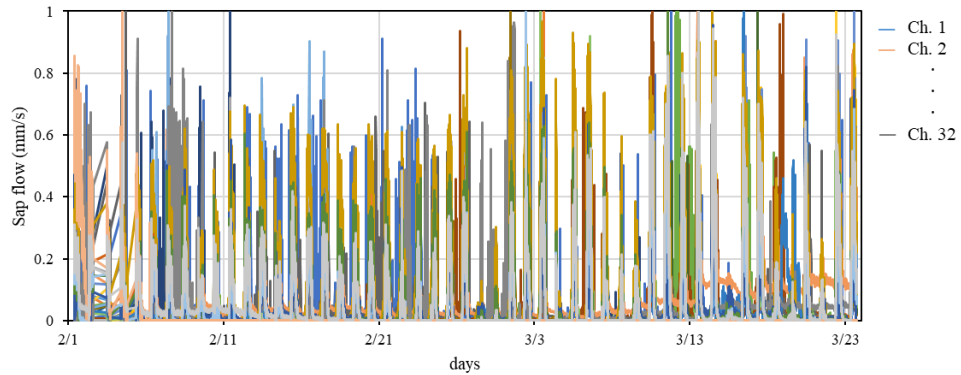


Figure 5-32. Measured sap flow signal from 32 tomato plants.

5.2.9. Statistical use of sap flow signal

The average of all sap flow signals was obtained. Figure 5-33 shows the average of 32 sensor signals between February 11th and February 16th. The change in the standard deviation of these signals is shown in Figure 5-34. The standard deviation appeared to be proportional to the averaged sap flow. Figure 5-35 shows the coefficient of variation of sap flow. Coefficient of variation was obtained by dividing the standard deviation by the mean value. This normalized standard deviation value was found to be larger at night with less sap flow than at day.

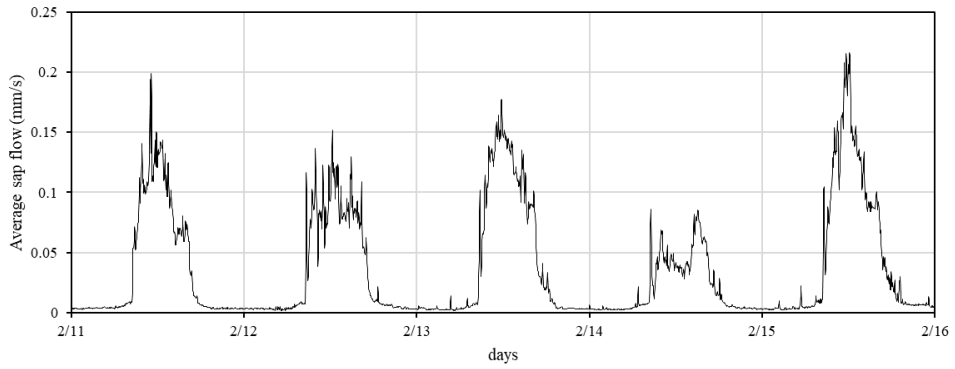


Figure 5-33. Average of 32 channels of sap flow signal.

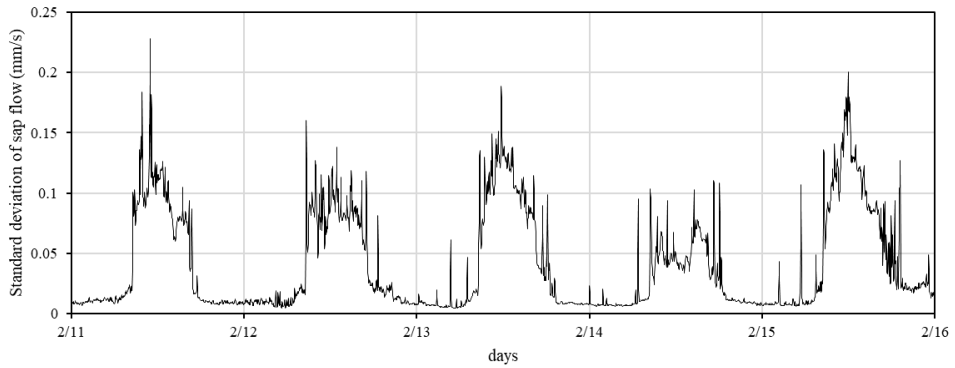


Figure 5-34. Standard deviation of 32 channels of sap flow signal.

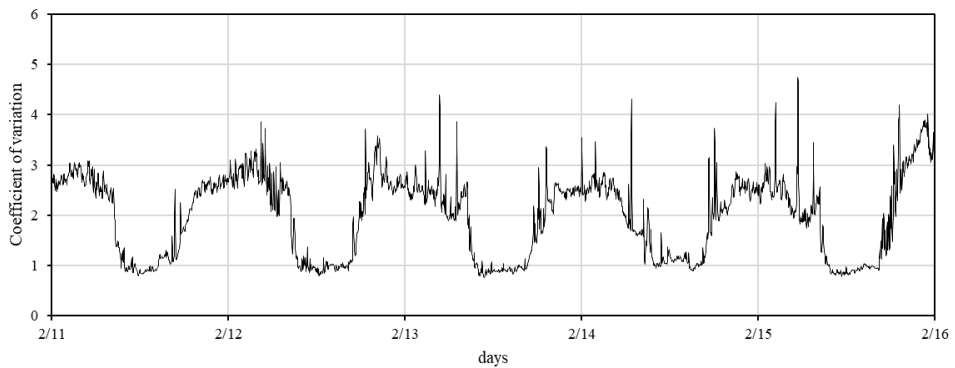


Figure 5-35. Coefficient of variation of 32 channels of sap flow signal.

A comparison was made between the mean value of the 32 sensor signals and the signal values of the individual sensors. Figure 5-36 shows the correlation between the averaged sensor signal value and the signal value of Ch.1. Figure 5-37 is the graph of Ch.1 sap flow value divided by averaged sap flow value. The graph shows that the sap flow rate of Ch.1 is about twice as high as the average.

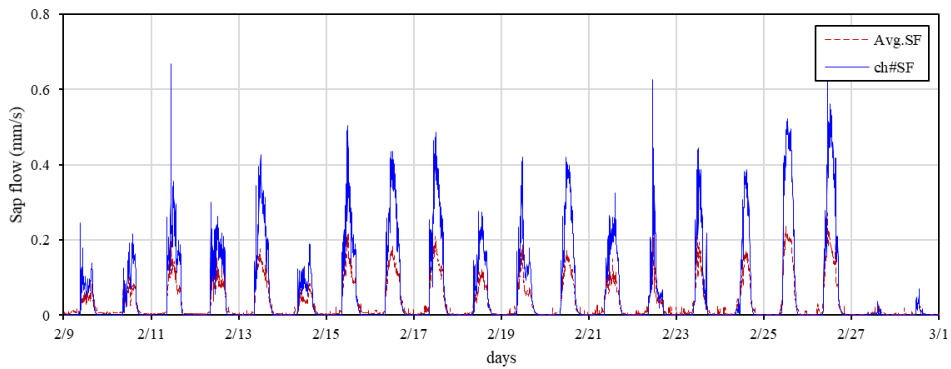


Figure 5-36. Comparison between the sap flow signal of Ch.1 and the averaged sap flow signal.

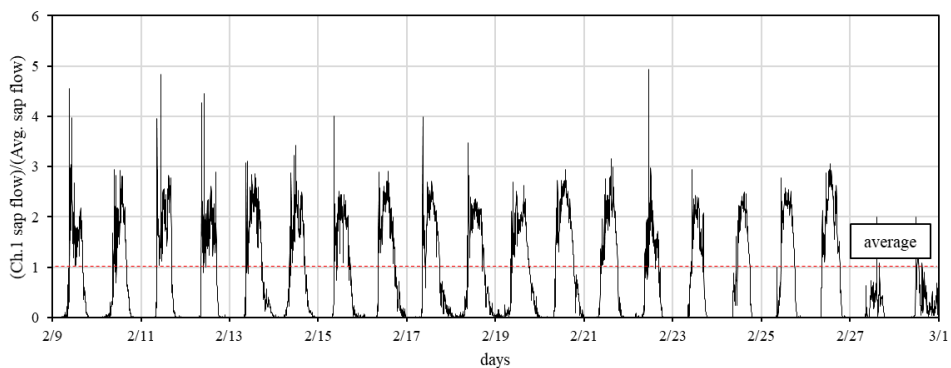


Figure 5-37. Graph of the sap flow rate of Ch.1 divided by the average sap flow rate.

On the other hand, Figure 5-38 and Figure 5-39 show the correlation between the averaged sap flow rate and sap flow rate value of Ch.11. The signal of Ch.11 shows an abnormal signal with high noise for the first 5 days. After 6 days, sap flow value is similar to the averaged sap flow value. The sap flow value of Ch.11 then decreased compared to the average. From the result, it is possible to deduce that the amount of sap flow in Ch.11 plants is decreasing compared to other plants.

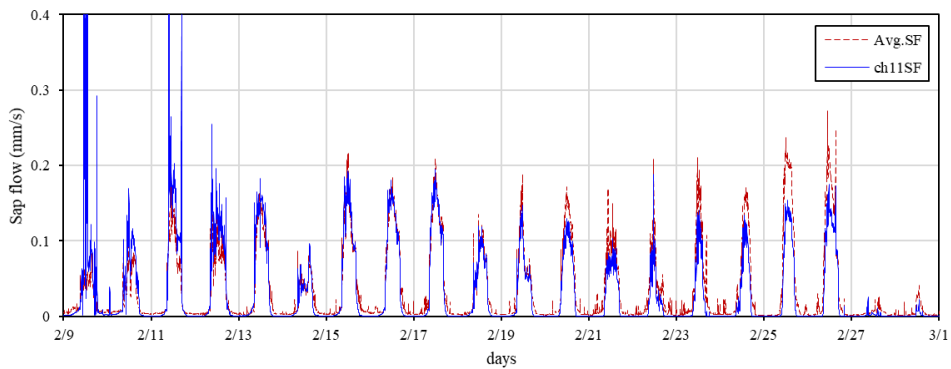


Figure 5-38. Comparison between the sap flow signal of Ch.11 and the averaged sap flow signal.

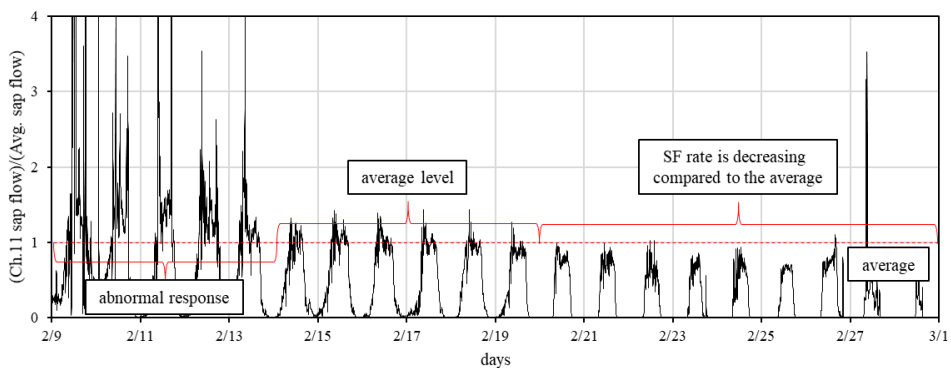


Figure 5-39. Graph of the sap flow rate of Ch.11 divided by the average sap flow rate.

Figure 5-40 is bar graphs showing the sap fluid rate of 32 sensors at one hour interval from 7:00 am to 6:00 p.m. on February 13th. The graph shows that the sap flow rate measured from each sensor is different at each time. The sap flow rate is also shown by histogram (Figure 5-41). The histogram of sap flow shows wide distribution. It was found that the biometric information individual plants have wide distribution.

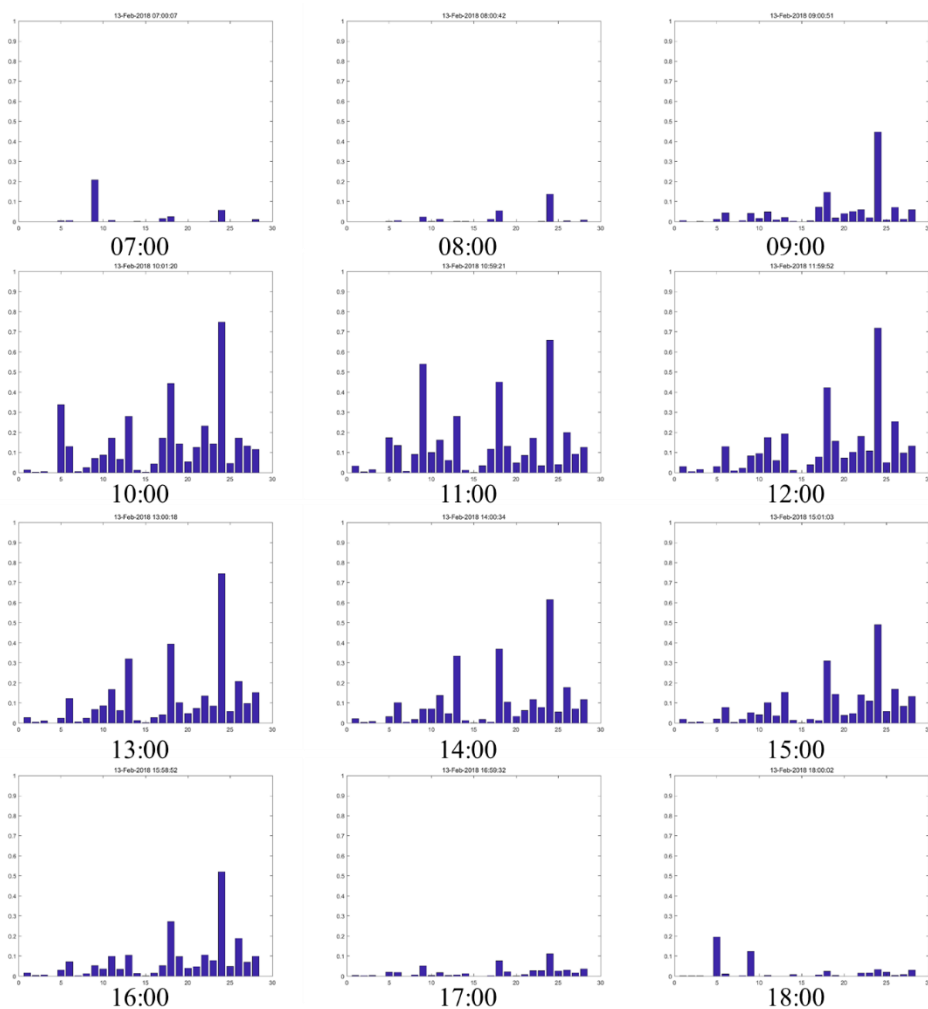


Figure 5-40. Bar graph of 32 channels of sap flow rate on Feb. 13th (x-axis: number of channel, y-axis: sap flow (mm/s)).

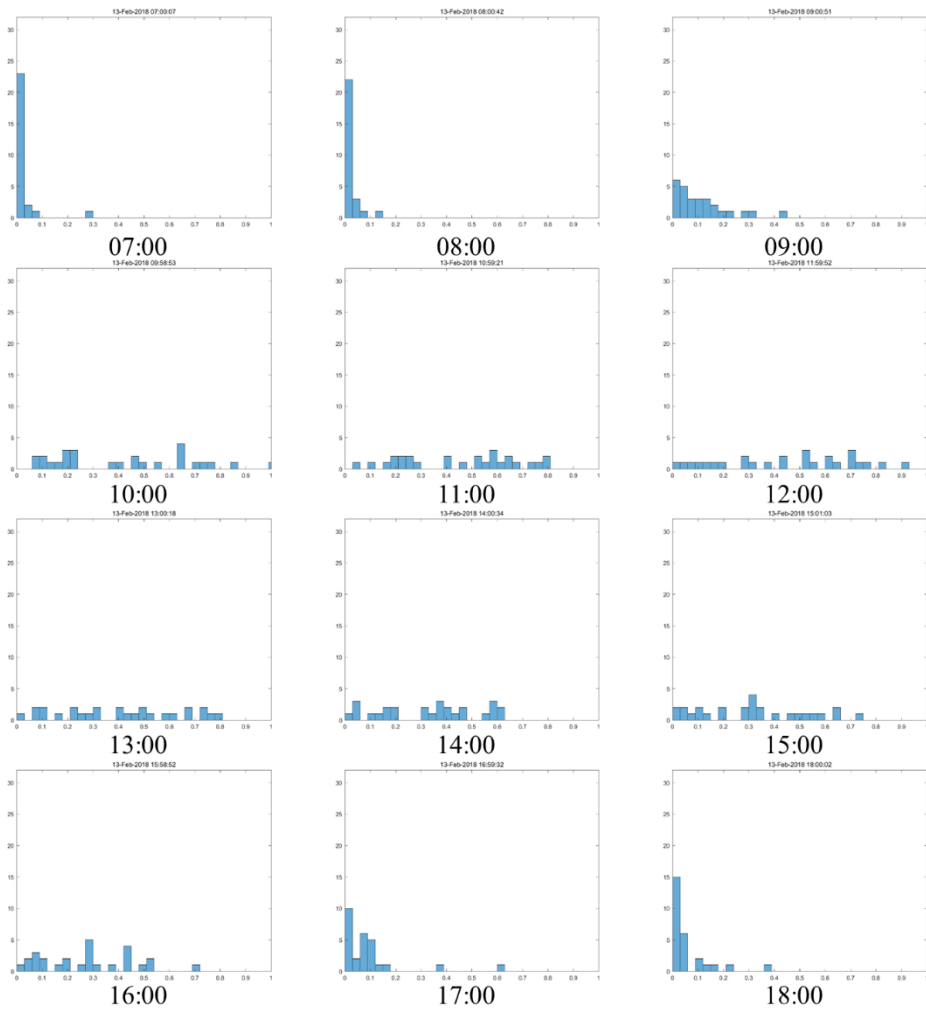


Figure 5-41. Histogram of 32 channels of sap flow rate on Feb. 13th (x-axis: sap flow (mm/s), y-axis: frequency).

5.2.10. Pedicel / peduncle sap flow measurement

Experiments to measure the sap flow in peduncle and pedicel of tomato plants were carried out. Figure 5-42 shows the sensor installed on the pedicel and peduncle. One sensor was installed in tomato peduncle. The peduncle was

connected to two fruits. The other sensor was installed on a pedicel attached to the larger fruits. Measurements were taken from 2017 September 30th, to October 10th.



Figure 5-42. Microneedle sap flow sensors installed on tomato peduncle and pedicel.

5.2.11. Result of pedicel / peduncle measurement

Figure 5-43 and Figure 5-44 show the sap flow rate and internal relative temperature of the peduncle. Figure 5-45 and Figure 5-46 show the sap flow rate and internal relative temperature of the pedicel. The sap flow of peduncle and pedicel was similar to the sap flow in the stem. The sap flow of peduncle and pedicel was higher during the days than the nights. From the result, it can be deduced that the growth of the fruit occurs during the day with the sap flow. It was observed that the sap flow rate decreased over the measurement period, which was due to the fact that the fruit growth rate slowed as the fruit grew.

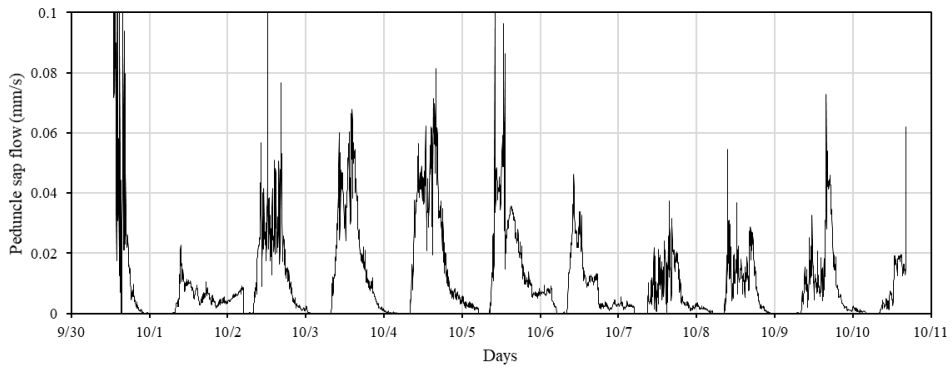


Figure 5-43. Sap flow rate of tomato peduncle.

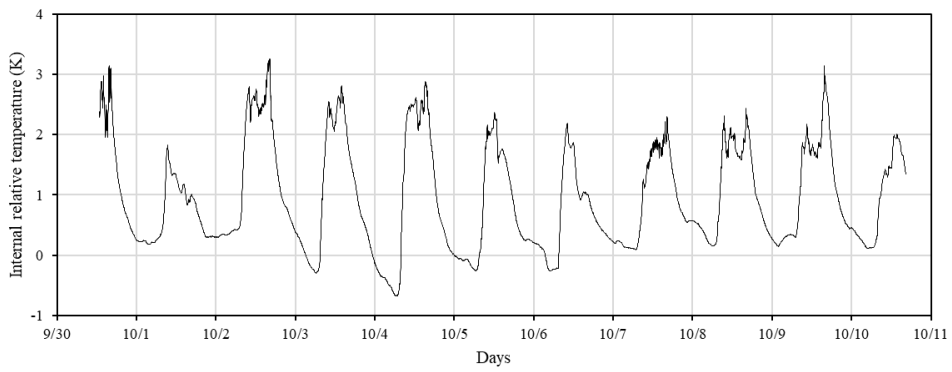


Figure 5-44. Internal relative temperature of tomato peduncle.

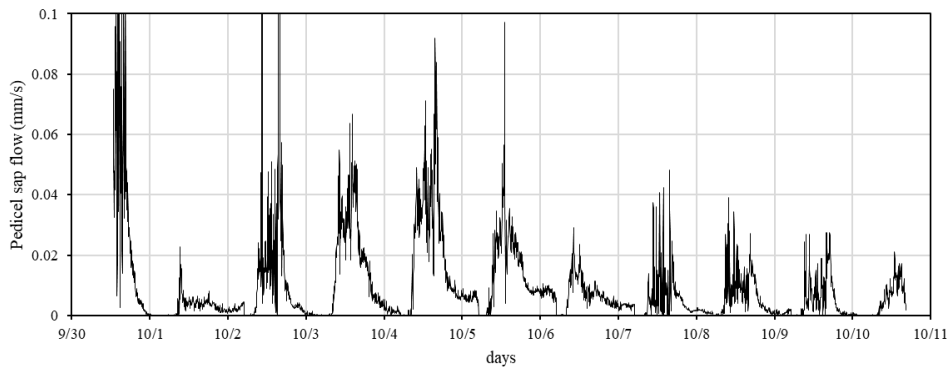


Figure 5-45. Sap flow rate of tomato pedicel.

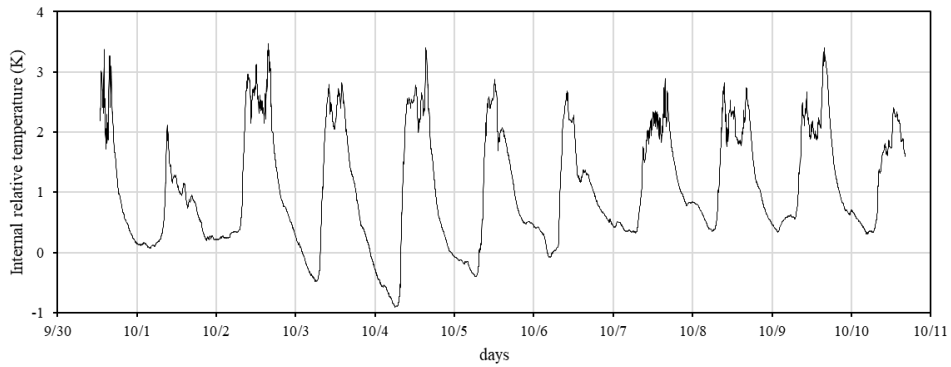


Figure 5-46. Internal relative temperature of tomato pedicel.

5.2.12. Conclusion of in-vivo measurement of tomato plant

Through the field experiment of tomato, it was confirmed that the sap flow and internal relative temperature of plants can be measured over a long period by using microneedle sap flow sensor. Also, it was found that the sap flow in plants was sensitive to environmental variables such as temperature, light intensity and VPD. Through the irrigation cut experiment, the response of the sap flow to the water stress condition of the plant was observed. A method has been proposed to predict the growth of a large number of plants and to compare the health status of individual plants through statistical analysis of the sap flow measurement data. Measuring the fluid flow of peduncle and pedicel has suggested a way to infer the hypertrophic state of the fruit.

5.3. In-vivo measurement of other plants

5.3.1. Measurement methods

The sap flow of various herbaceous plants was measured. The measurement period was from 2017 April 1st to 2018 April 2nd. The sap flow of paprika (*Capsicum annuum*), cucumber (*Cucumis sativus*), Clusia (*Clusia major*) and rubber tree (*Ficus elastica*) was measured. 26 measurements were made during a total of 260 days (Table 5-2).

Table 5-2. List of field experiments of microneedle sap flow sensor for other herbaceous plants.

Subject	Period	Duration	# of sensors	Place
Paprika	2017-06-15 ~ 2017-07-25	41	8	Hwasung
Paprika	2017-07-25 ~ 2017-08-17	24	4	Haman
Cucumber	2017-04-01 ~ 2017-04-28	28	4	Ilsan
Clusia	2017-04-27 ~ 2017-05-16	20	2	Gwanak
Clusia	2017-09-21 ~ 2017-11-20	61	2	Gwanak
Clusia	2018-03-09 ~ 2018-04-02	25	4	Gwanak
Rubber plant	2017-09-21 ~ 2017-11-20	61	2	Gwanak

5.3.2. In-vivo measurement of paprika

The measurement of paprika was made for 24 days from 2017 July 25th to 2017 May 17th. Figure 5-47 shows the sap flow sensor installed on the paprika stem. The sensor was installed about 10 cm from the root. A total of eight sensors were installed. The maximum sap flow rate of paprika was found to be about 0.1

mm/s to 0.25 mm/s (Figure 5-48).



Figure 5-47. Experiment set up for in-vivo measurement of paprika (left). Microneedle sap flow sensor installed on paprika stem (right).

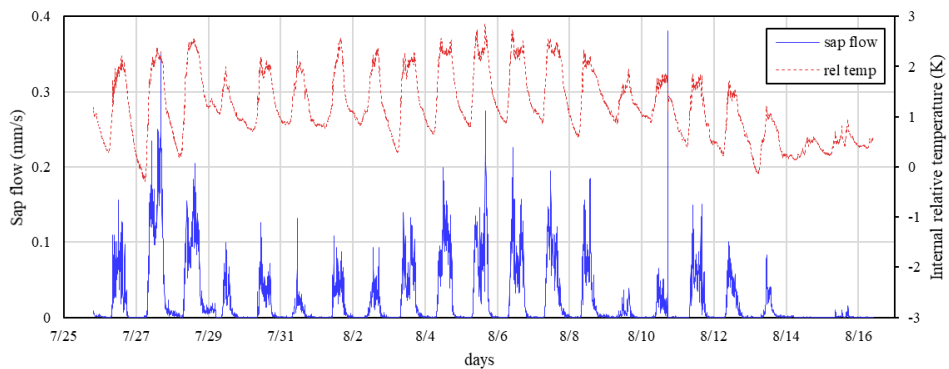


Figure 5-48. Sap flow and internal relative temperature of paprika stem.

5.3.3. In-vivo measurement of cucumber

The measurement of cucumber was made for 28 days from 2017 April 1st to 2017 April 28th. Figure 5-49 shows the sap flow sensor installed on the cucumber. The sensor was installed about 50 cm from the root. A total of four sensors were

installed. The maximum flow rate of the cucumber was about 0.4 mm/s to 0.6 mm/s (Figure 5-50).



Figure 5-49. Experiment set up for in-vivo measurement of cucumber (left).

Microneedle sap flow sensor installed on cucumber stem (right).

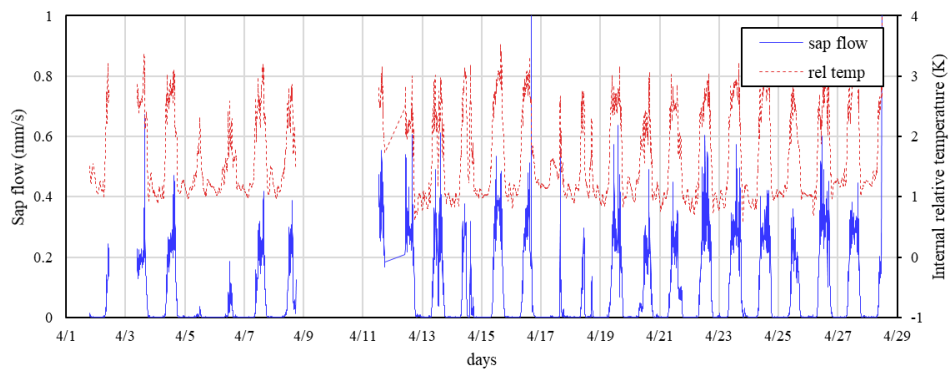


Figure 5-50. Sap flow and internal relative temperature of cucumber stem.

5.3.4. In-vivo measurement of clusia

The measurement of clusia was made for 20 days from 2017 April 27th, to 2017 May 16th. Figure 5-51 shows a sap flow sensor installed on a clusia. The

sensor was installed about 1 cm from the root. A total of four sensors were installed. The maximum flow velocity of the rubber tree was about 0.002 mm/s to 0.005 mm/s. The sap flow measurement result of the clusia was different from that of other plants (Figure 5-52, 53). In Figure 5-52 and 53, the parts marked in red indicates daytime. The sap flow of most plants occurs in daytime (diurnal sap flow) and during the night, there is little sap flow. However, in clusia case, there was little sap flow in daytime. After the sunset, sap flow rate increased (nocturnal sap flow) (Figure 5-52). Also, during some periods, switching between diurnal sap flow and nocturnal sap flow was observed (Figure 5-53). This is because Clusia is a C3-CAM photosynthesis plant [1].

The C3 photosynthesis process takes place in normal plants (Figure 5-54). This process is highly efficient in converting light into energy, but it has the disadvantage of large water losses due to transpiration during the day. Thus, many plants that live in arid regions get energy from CAM photosynthesis process. During the CAM photosynthesis process, CO₂ is stored as the four-carbon acid malate in vacuoles at night. During the daytime the stomata is closed and photosynthesizes consuming malate acid [2]. Transpiration occurs during the night time when the stomata are opened and sap flow occurs at night. Clusia can switch between the C3 and CAM photosynthesis selectively depending on the climate [3]. Therefore, the sap flow of clusia can occur as either nocturnal sap flow and diurnal sap flow [4, 5].



Figure 5-51. Experiment set up for in-vivo measurement of clusia (left). Microneedle sap flow sensor installed on clusia stem (right).

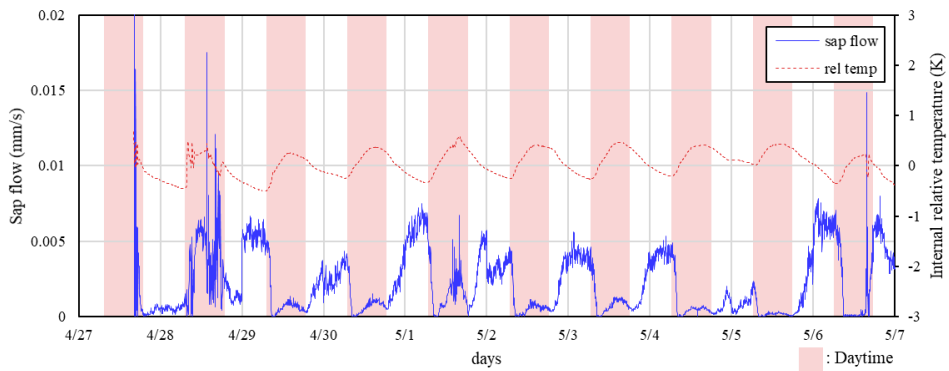


Figure 5-52. Sap flow and internal relative temperature of clusia stem. The daytime is marked with red box.

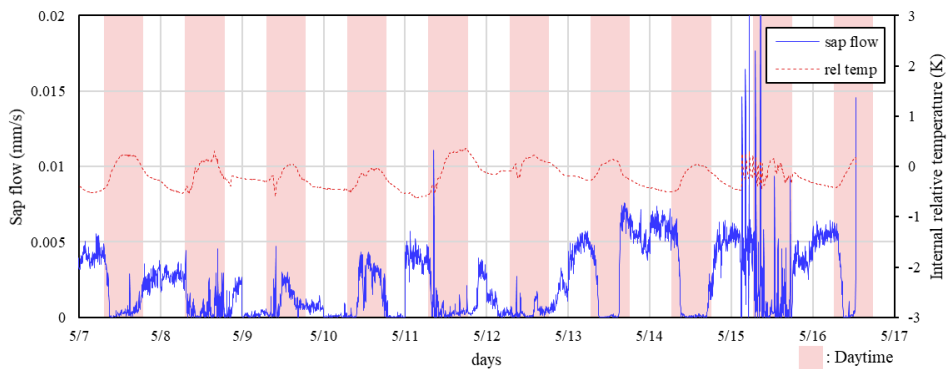


Figure 5-53. Sap flow and internal relative temperature of clusia stem. The daytime is marked with red box.

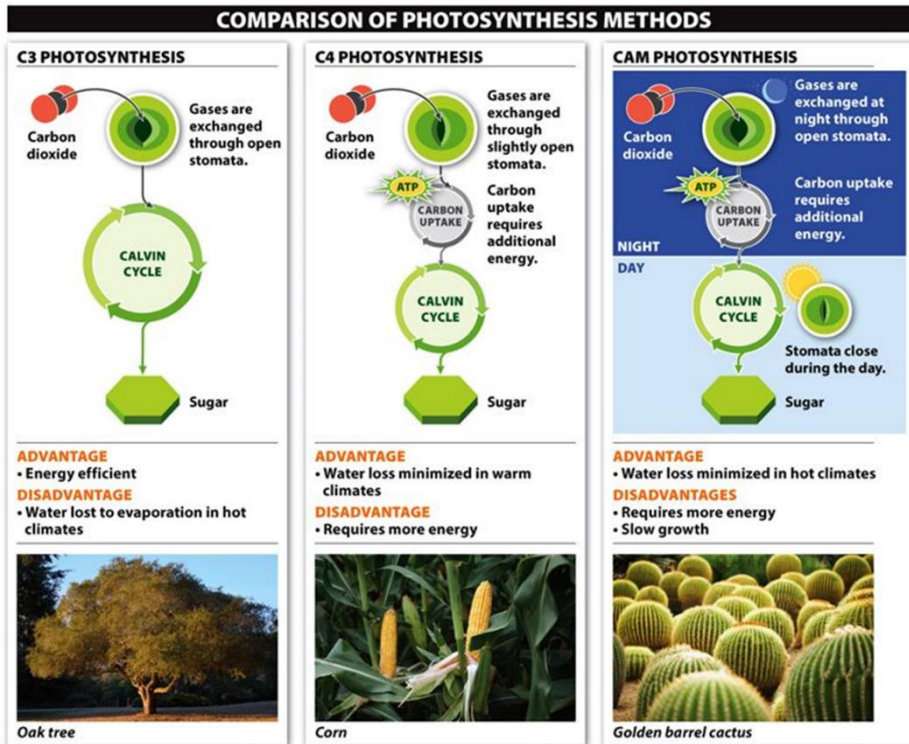


Figure 5-54. Comparison between C3, C4 and CAM photosynthesis mechanism [6].

5.3.5. In-vivo measurement of rubber tree

From 2017 September 21st to 2017 November 20th, sap flow measurements of rubber tree were made for 61 days. Figure 5-55 shows a sap flow sensor installed on a rubber tree. The sensor was installed about 20 cm from the root. A total of two sensors were installed. The daily maximum flow velocity of the rubber tree was about 0.02 mm/s to 0.08 mm/s (Figure 5-56).



Figure 5-55. Experiment setup for in-vivo measurement of rubber tree (left).

Microneedle sap flow sensor installed on rubber tree stem (right).

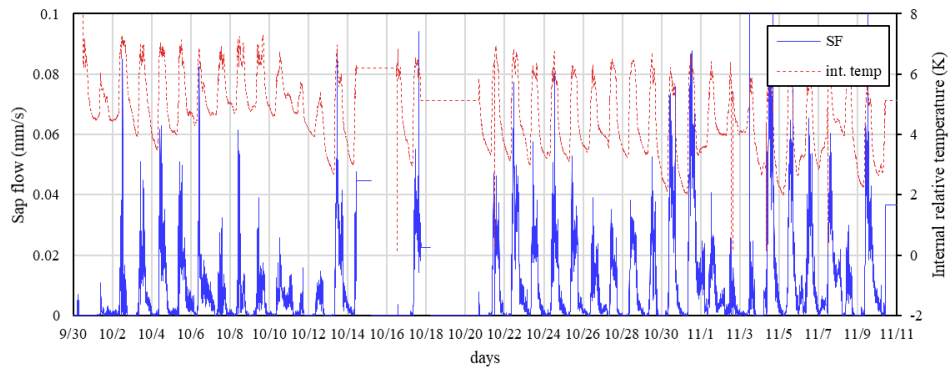


Figure 5-56. Sap flow and internal relative temperature of rubber tree stem.

5.4. Microneedle implantation effect

Implantation and measurement tests showed a good adaptation of the microneedle probes in the plant tissue. A concern was raised regarding the biological rejection of the plant against needle implantation. Woody plants, for example, form a compartment to reject the wound when a thick object is inserted into the stem [7]. Obviously, this wounding effect will stop the measurement. In our case, however, the implanted microneedle survived for a long period. The longest measurement, so far, was over 60 days. It appears that the soft tissue of tomato stem is relatively generous against the insertion of a thin object like the microneedle. Furthermore, the temperature increase during the measurement was limited to 2.5°C which had a small thermal impact on the plant. This is in contrast with the conventional thermal probes that need the temperature increase up to 8-10°C with a direct impact on the growth because of the large heat capacity of the thermal probes.

Figure 5-57 shows the surface of implantation site after 37 days of measurement. The microneedle probe was broken before taking the picture. The photographs of the tomato stem surface showed an apparently clean appearance except for a slight browning. Figure 5-58 shows the cross section of the tomato stem that shows the xylem area and the trace of implanted microneedle. The image was taken with micro-computed tomography (Skyscan 1172, Skyscan). It was also observed that the plant had no degradation due to the implantation. The sensor functioned properly when placed in the xylem area. In some cases, however, it landed in the pith area where the sap flow was very weak. The location of the xylem and the state of implant can be monitored when multiple patterns are used

in an array. In this case, the flow pattern in the stem can be traced for a more accurate measurement. This technique will be introduced in the following sections. Most failure occurred because of the breakage during agricultural treatment and electrical breakdown of the metal patterns rather than biological rejection. It is interesting to note that the signal is weak and unstable right after the insertion of the microneedle. The signal, however, becomes clear and stable within a day after the insertion as the plant tissue grows and firmly grips around the microneedle from the exterior skin. It was often observed that the microneedles were not easily removed from the plants because of the tight engagement.



Figure 5-57. Surface of tomato stem after 37 days of measurement.

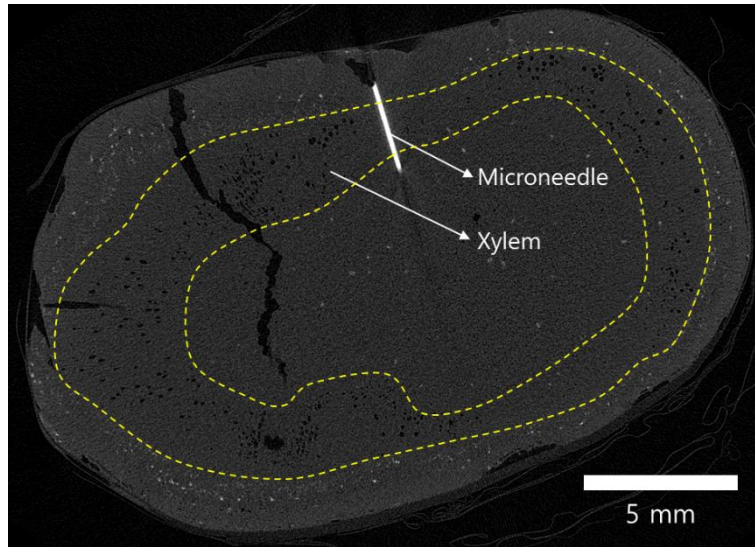


Figure 5-58. Micro CT image of tomato stem with the trace of the microneedle sensor. The position of the microneedle sap flow sensor is indicated by the white line. The distribution of xylem in the tomato stem is marked with yellow dotted lines.

5.5. Conclusion

The sensors were installed a greenhouse plants to measure the *in-vivo* signal with minimal invasion for 612 days. More than 207 sensors were installed and sap flow and internal relative temperature were measured. Through the tomato artificial light experiment, the sap flow caused by artificial light was measured. Through field experiments, we could measure the sap flow of tomato in long-term for over 60 days. The measured sap flow signal showed a close relationship with the solar radiation and other environmental variables. There was close correlation between the sap flow of tomato and environmental variables such as temperature, light intensity and VPD. Through the irrigation cut experiment, the response of the sap flow to the water stress condition of the plant was observed. Measuring sap flow of multiple plants and comparing the health status of individual plants method was proposed from the mass population measurement and statistical analysis of sap flow data. Measuring the sap flow of peduncle and pedicel suggests a way to infer the hypertrophy of the fruit. The sensors were installed on other herbaceous plants such as paprika, cucumber, clusia, and rubber trees, and were able to measure physiological information of various plants. Interesting phenomena such as nocturnal sap flow were observed during the experiment.

Bibliography

- [1] A. Roberts, A. M. Borland, K. Maxwell, and H. Griffiths, "Ecophysiology of the C3-CAM intermediate *Clusia minor* L. in Trinidad: seasonal and short-term photosynthetic characteristics of sun and shade leaves," *Journal of Experimental Botany*, vol. 49, no. 326, pp. 1563-1573, 1998.
- [2] W. Cockburn, I. P. Ting, and L. O. Sternberg, "Relationships between Stomatal Behavior and Internal Carbon Dioxide Concentration in Crassulacean Acid Metabolism Plants," *Plant Physiology*, vol. 63, no. 6, pp. 1029-1032, 1979.
- [3] U. Lüttge, "Photosynthetic flexibility and ecophysiological plasticity: questions and lessons from *Clusia*, the only CAM tree, in the neotropics," *New Phytologist*, vol. 171, no. 1, pp. 7-25, 2006.
- [4] M. A. Forster, "How significant is nocturnal sap flow?," *Tree Physiology*, vol. 34, no. 7, pp. 757-765, 2014.
- [5] A. Herrera, C. Ballestrini, and W. Tezara, "Nocturnal sap flow in the C3-CAM species, *Clusia minor*," *Trees*, vol. 22, no. 4, pp. 491-497, 2008.
- [6] J. Phelan, *What is Life? A Guide to Biology*. W.H. Freeman and Company, 2010.
- [7] K. T. Smith, "Wounding, compartmentalization, and treatment tradeoffs," *Journal of Arboriculture*, vol. 14, no. 9, pp. 226-229, 1988.

Chapter 6. Compensation of Natural Temperature Gradient

6.1. Introduction to natural temperature gradient (NTG)

6.1.1. What is NTG

A natural temperature gradient (NTG) is a spatio-temporally variable temperature gradient in tree trunks occurring due to the natural and environmental forces [1]. The NTG depends on climatic conditions of an area investigated including seasonal solar incidence, wind speed and direction, latitude, cloud cover, density of vegetation, species type, biometric properties, the height of the measuring point above the ground, thickness of the bark, azimuthal positioning at the perimeter of a stem, positioning with respect to adjacent trees, growth irregularities of the tree trunk, soil type, canopy shielding and possibly other unknown factors yet to be discovered [2].

6.1.2. Effect of NTG in sap flow measurement

NTG biases the thermal dissipation probe measurements in a way that is undetectable when a standard thermal dissipation probe setup is applied [3]. It is observed by experiments that the impact of NTG upon the measured sap flow is most significant in sparse savannah vegetation well exposed to the sun, in conditions of large diurnal temperature variations [2, 4] and on trees with low sap flows [5].

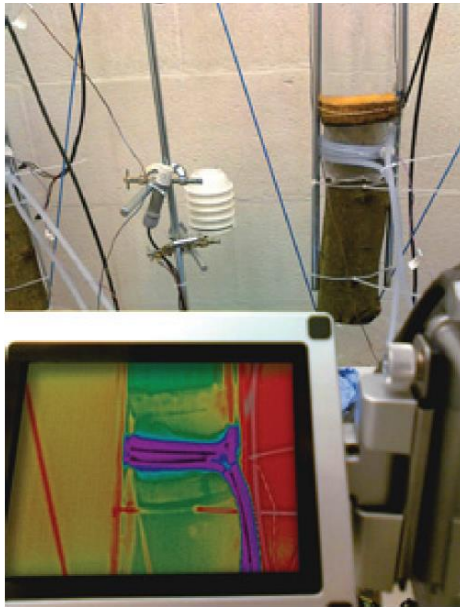


Figure 6-1. Temperature gradient monitored by infrared imagery [6].

6.2. Compensation of NTG

6.2.1. Compensation method for NTG

There have been efforts to reduce the error caused by NTG. F. Do attempted to measure NTG using a non-continuous heating system and calibrate the effect of NTG in thermal dissipation probe [7]. Lubczynski analyzed the thermal response of thermal dissipation probes and attempted to estimate and correct NTG values through heat model and extrapolation [1]. All of these studies address the spatial NTG correction method for the thermal dissipation method, which uses two probes for sap flow measurement. For the presented sap flow measurement method which uses single microneedle probe, temporal NTG comes into play. The single microneedle probe can remove the spatial NTG effect. However, the probe is affected by the temporal NTG that occurs during the ambient temperature change. Therefore, a correction method that can remove temporal NTG is needed.

A reference probe that capable of measuring the NTG value was proposed in order to remove the temporal NTG from the sap flow measurement. This reference probe can calibrate the temporal NTG value by measuring the temperature change inside the plant due to the ambient temperature change. The reference probe has the same structure as the microneedle probe but does not generate heat and only measures the relative temperature in the plant (Figure 6-2).

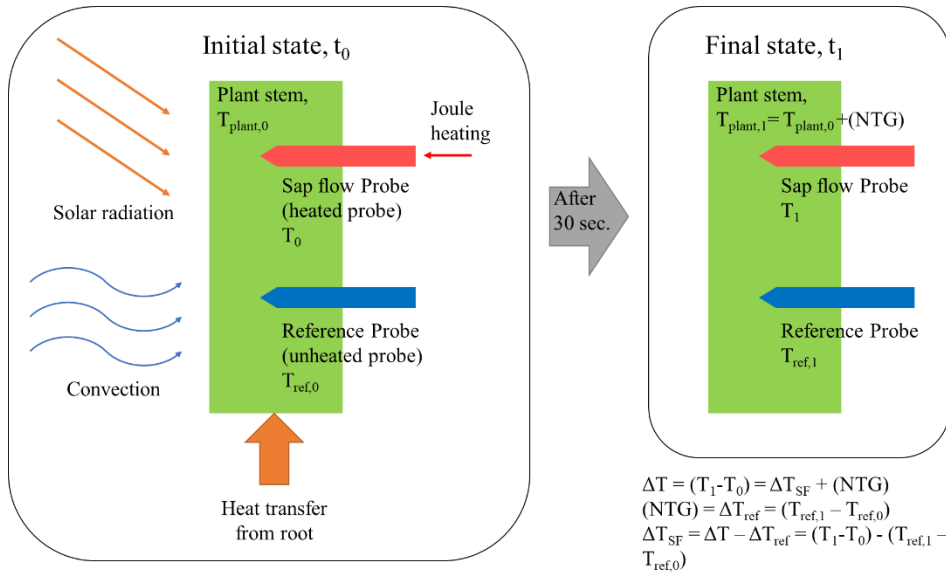


Figure 6-2. Installation of reference probe for NTG compensation and compensation method.

Figure 6-2 shows the installation method of reference probe and compensation process. The thermal probe can be affected by the external temperature change, heating and cooling. The temperature difference signal ΔT is sum of the thermal dissipation signal (T_{SF}) and NTG:

$$\Delta T = (T_1 - T_0) = T_{SF} + NTG, \quad (6-1)$$

where T_1 is heated temperature of sensor probe, T_0 is unheated temperature of a sensor probe, T_{SF} is thermal dissipation signal. NTG is measured from the reference probe. The reference probe is not heated and measures the temperature change during the heating process of sensor probe:

$$NTG = T_{ref,1} - T_{ref,0}, \quad (6-2)$$

where $T_{ref,0}$ is initial reference temperature and $T_{ref,1}$ is reference probe temperature after heating process. The thermal dissipation signal (T_{SF}), the temperature difference due to the sap flow, is obtained by subtracting NTG from the temperature difference signal (ΔT):

$$T_{SF} = \Delta T - NTG = (T_1 - T_0) - (T_{ref,1} - T_{ref,0}). \quad (6-3)$$

Figure 6-3 shows the measurement setup for the NTG calibration experiment. A tomato seedling of about 60 cm in height were used for the experiment. The tomato seedling was placed in a 60 * 60 * 60 cm artificial light experimental box. The artificial light box is equipped with two 300 W halogen lamps and one 30 W white LED light. The artificial temperature gradient and sap flow of the tomato plant is triggered by the artificial light. By turning the lights on and off at 2-hour intervals, to make rapid temperature and light intensity changes we observed the reaction of plants and sensors. Measurement setup and data collection program modifications were made for the experiment.



Figure 6-3. Experimental setup for NTG compensation.

6.2.2. NTG compensaion result

The measured internal relative temperature of the plant is shown in Figure 6-4. The periods when the plant are heated by the light source is indicated by red boxes. In each of three irradiation intervals, the relative temperature in the plant varied by about 1°C, 3°C, and 2.2°C. The rapid temperature change was observed after turning on and off the light. The NTG effect is expected to be high during sudden changes in light condition.

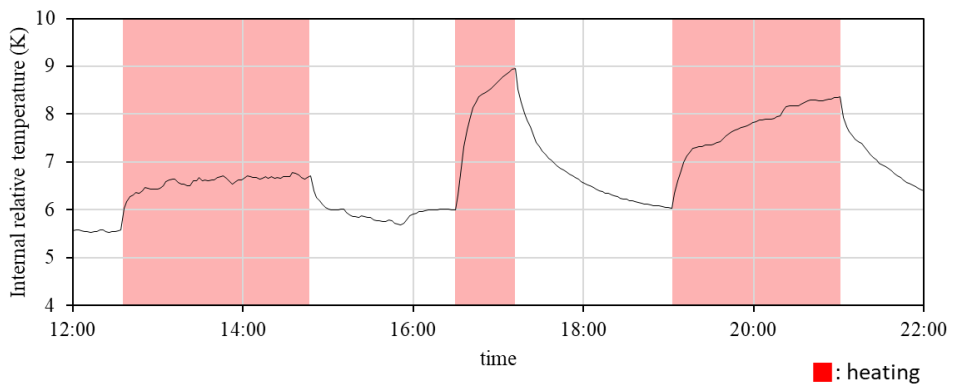


Figure 6-4. Internal relative temperature during NTG compensation experiment.

Figure 6-5 shows the temperature difference signal measured by the sensor probe. The transpiration and sap flow occur actively after turning on the light, which lowers the temperature differential signal. Also, the error peaks due to the NTG were observed after turning on and off the light. Figure 6-6 shows the NTG value measured by the reference probe. The measured NTG was similar with Figure 6-5. Spiking of NTG was observed when there was rapid change of internal relative temperature. Also the NTG from the other environmental factors such as convection was observed when the light was off. Figure 6-7 shows the compensated thermal dissipation signal which is the temperature difference signal minus NTG value. Figure 6-7 shows a smooth graph shape compared to Figure 6-5.

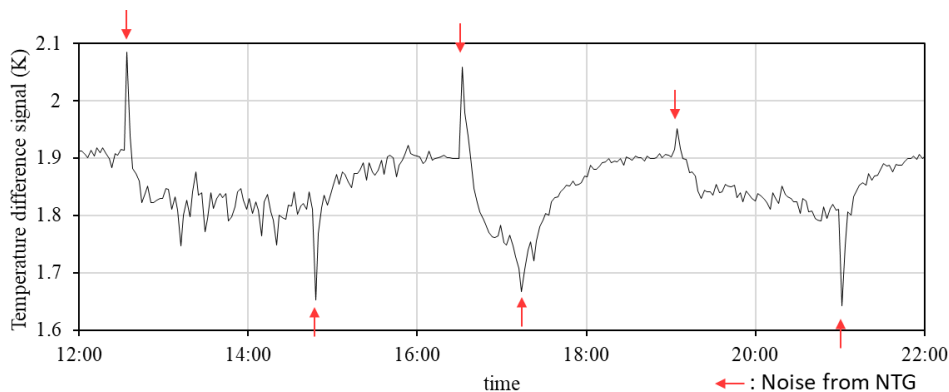


Figure 6-5. Temperature difference signal during NTG compensation experiment.

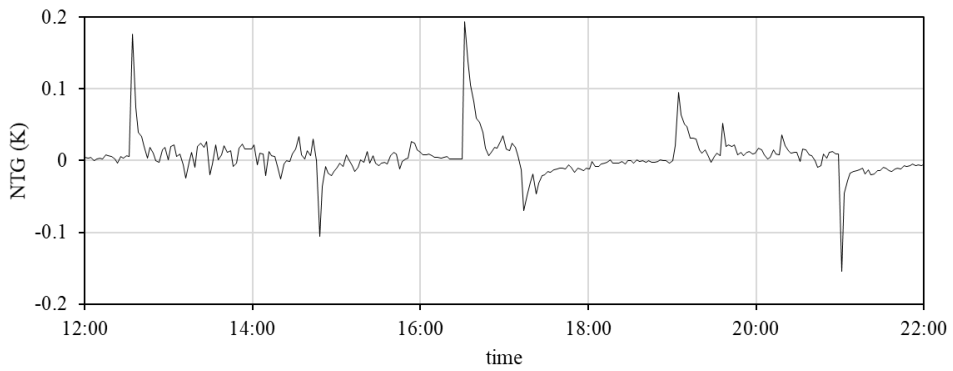


Figure 6-6. Natural temperature gradient error during NTG compensation experiment.

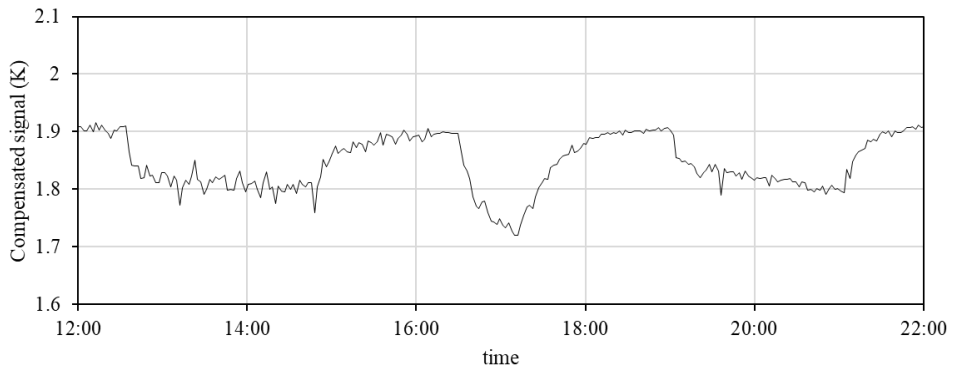


Figure 6-7. Compensated thermal dissipation signal during NTG compensation experiment.

Figure 6-8 shows the sap flow measurement results without NTG compensation. The change of the sap flow rate due to the artificial light is superposed by errors due to NTG. Figure 6-9 shows the measured sap flow rate with NTG compensation. In the graph, it can be seen that the error due to NTG is considerably reduced after removing the error peaks. Also, Figure 6-9 shows a smooth graph shape compared to Figure 6-8.

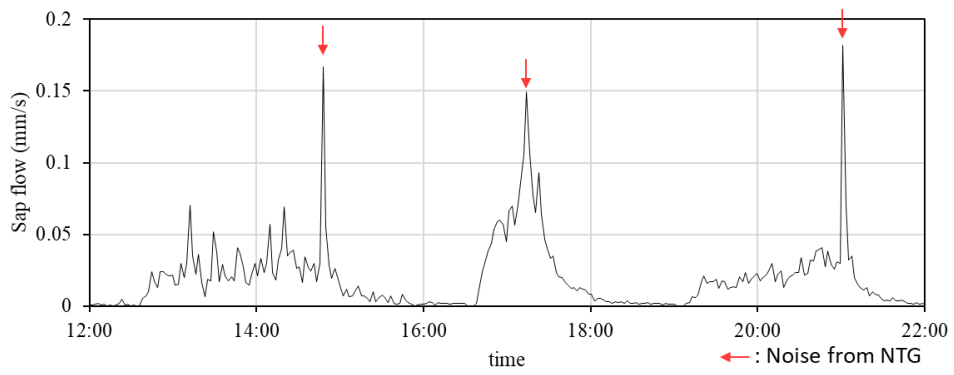


Figure 6-8. Measured sap flow rate without NTG compensation.

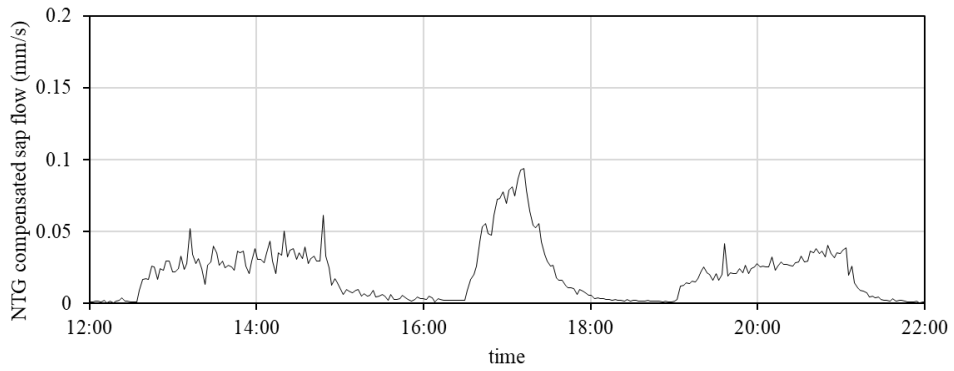


Figure 6-9. Measured sap flow rate with NTG compensation.

6.3. Conclusion

NTG is a spatio-temporally variable temperature gradient in tree trunks occurring due to the natural and environmental forces. NTG biases the thermal dissipation probe measurements. Compensation of NTG method by using reference probe was proposed and tested. An artificial light illumination test with NTG compensation was conducted. It was possible to reduce the NTG error from the thermal dissipation signal with NTG compensation method. The compensation method can reduce the error peak caused by NTG. This method can compensate for the influence of the advection, the ambient temperature fluctuation, etc., and the overall noise reduction of the sap flow is possible. It is expected to increase the accuracy of measurement when it is applied in conditions of large diurnal temperature variations.

Bibliography

- [1] M. W. Lubczynski, D. Chavarro-Rincon, and J. Roy, "Novel, cyclic heat dissipation method for the correction of natural temperature gradients in sap flow measurements. Part 1. Theory and application," *Tree Physiology*, vol. 32, no. 7, pp. 894-912, 2012.
- [2] J. Čermák and J. Kučera, "The compensation of natural temperature gradient at the measuring point during the sap flow rate determination in trees," *Biologia Plantarum*, vol. 23, no. 6, pp. 469-471, 1981.
- [3] A. Granier, "Une nouvelle méthode pour la mesure du flux de sève brute dans le tronc des arbres," *Ann. For. Sci.*, vol. 42, no. 2, pp. 193-200, 1985.
- [4] F. Do and A. Rocheteau, "Influence of natural temperature gradients on measurements of xylem sap flow with thermal dissipation probes. 1. Field observations and possible remedies," *Tree physiology*, vol. 22, no. 9, pp. 641-648, 2002.
- [5] J. L. Reyes-Acosta, M. W. Vandegehuchte, K. Steppe, and M. W. Lubczynski, "Novel, cyclic heat dissipation method for the correction of natural temperature gradients in sap flow measurements. Part 2. Laboratory validation," *Tree physiology*, vol. 32, no. 7, pp. 913-929, 2012.
- [6] J. L. Reyes-Acosta, "Tree-water Interactions at Varying Spatiotemporal Scales in a Water Limited Environment," 2015.
- [7] F. Do and A. Rocheteau, "Influence of natural temperature gradients on measurements of xylem sap flow with thermal dissipation probes. 2. Advantages and calibration of a noncontinuous heating system," *Tree physiology*, vol. 22, no. 9, pp. 649-654, 2002.

Chapter 7. Array Sensor Measurement

7.1. Introduction

7.1.1. Measurement of sap flow distribution

The stems and roots of plants are highly specialized conductive organs that can transport water, nutrients, photosynthetic products and chemical regulatory signals. These organs contain two types of conductive tissue: phloem and xylem [1]. The xylem is responsible for the transport of water and nutrients from the soil to the leaves, whereas the phloem is responsible for the transport of photosynthesis, amino acids and electrolytes from source leaves to the rest of the plant [2]. Therefore, if the water transportation in phloem and xylem can be measured individually, it is possible to monitor the biometric information of plants.

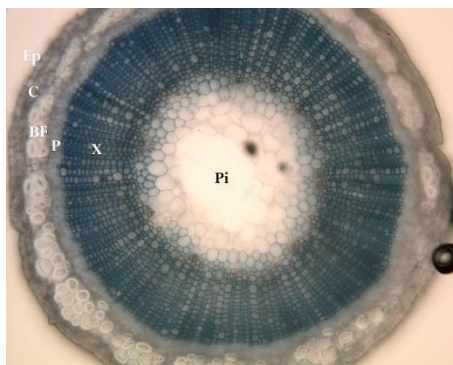


Figure 7-1. Cross-sectional image of a plant stem (Ep: epidermis, C: cortex, BF: bast fibres, P: phloem, X: xylem, Pi: pith) [3].

The microneedle sap flow sensor measures the sap flow by thermometric method. The thermal conductivity of silicon is very high and this makes heat dissipate through the sensor body (Figure 7-2). The microneedle sap flow sensor with silicon substrate have limited performance for local measurement due to its thermal property. Therefore, development of a sensor capable of local measurement is desired.

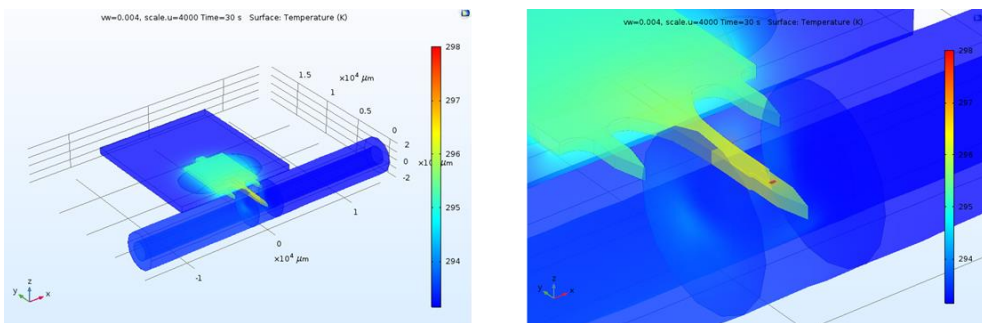


Figure 7-2. Thermal simulation for silicon substrate microneedle.

7.2. Design and fabrication

7.2.1. Sensor design

Microneedle sap flow sensor for local measure was designed. A substrate material to replace silicon was selected. The substrate material should have low thermal conductivity and also should be compatible with MEMS fabrication process. Several materials were considered as the substrate material (Table 7-1). Quartz wafer was selected for the substrate material. Pyrex glass and Polyimide have low thermal conductivity but were excluded due to their compatibility problem with semiconductor processes.

Table 7-1. Comparison of material properties for substrate materials.

Material	Silicon	Sapphire	Quartz	Pyrex glass	Polyimide
Thermal conductivity (W/mK)	130	23	1.46	1.11	0.12
Semiconductor process compatibility	O	O	O	X	X
High temperature process compatibility	O	O	O	O	X

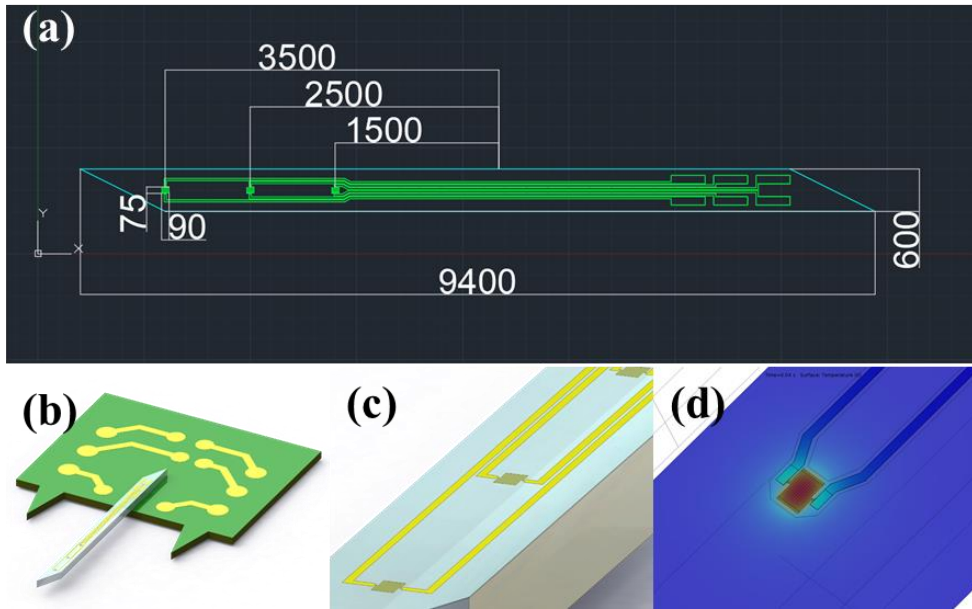


Figure 7-3. Blueprint of quartz microneedle probe sensor (a). Design scheme of quartz microneedle probe assembly (b). Magnified image of heating thermistor (c). Heat transfer simulation results (d).

Figure 7-3 (a) shows the blueprint of quartz microneedle probe. The outer dimension of sensor was $9400 \times 600 \times 300 \mu\text{m}$. The size of heating thermistor was $75 \times 90 \mu\text{m}$ and arranged at 1-mm intervals. The depth of thermistor was 3.5, 2.5, and 1.5 mm when inserted. The contact pads were placed on the other side. The cross sensitivity effect due to the thermal conduction through the substrate was studied using COMSOL multiphysics simulation. The heat transfer simulation shows that the temperature change due to heat generated by the heater were negligible at more than $100 \mu\text{m}$ away from the heating element (Figure 7-3 (d)).

7.2.2. Sensor fabrication

Deep reactive ion etching process was used to make needle shape in silicon microneedle fabrication. However, it is not possible to process quartz wafer (silicon dioxide) with DRIE process. The alternative microneedle formation process was required for quartz microneedle probe sensor. Dicing process was used for needle formation process. A needle shape with sharp ends was obtained by obliquely cutting in the longitudinal direction of the needle. Detailed fabrication process is shown in Figure 7-4.

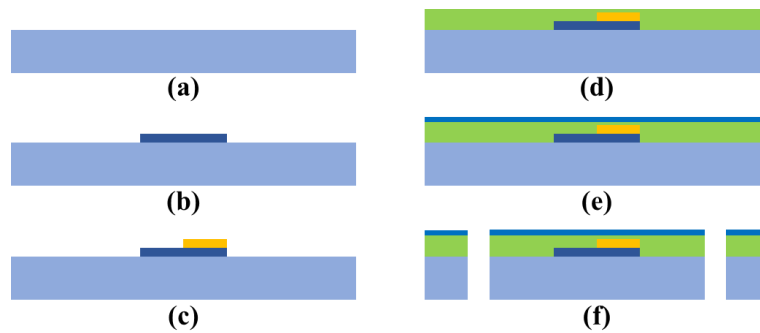


Figure 7-4. Fabrication process of quartz microneedle probe. Substrate preparation (a). Electrode 1 patterning (b). Electrode 2 patterning (c). Dielectric layer deposition (d). Polymer layer deposition (e). Dicing (f).

The fabrication was performed at Inter-University Semiconductor Research Center, SNU, and Korea Advanced Nano Fab Center. 4-inch 300- μm quartz wafers were used for substrate (WRS materials). The wafers were prepared with piranha cleaning (Figure 7-4 (a)). 4000 \AA Titanium and 2000 \AA gold layers were deposited with e-gun evaporation (ZZS550-2/D, MAESTECH) method, and patterned with

photolithography (MA-6, Karl-suss) and inductive coupled plasma (PlasmaPro ICP System100 Cobra, Oxford instruments) etching process (Figure 7-4. (b, c)). Three layers of 2000 Å silicon nitride film and two layers of 2000 Å silicon oxide film were alternately deposited (Ni-Ox-Ni-Ox-Ni) as the top insulation layer with a plasma enhanced chemical vapor deposition (VL-LA-PECVD, Unaxis) (Figure 7-4. (d)). 1000 Å parylene layer is deposited as the polymer protection layer (PDS-2010, SCS INC.) (Figure 7-4. (e)). The wafer was cut and needle shape was formed with dicing saw (DAD 522, DISCO) (Figure 7-4. (f)). The number of manufactured sensors was about 550 samples per 4-inch wafer. The yield was 95% or more. The sensor was packaged with wire bonding. A needle structure was built on the PCB board to prevent it from turning when installed on plants.

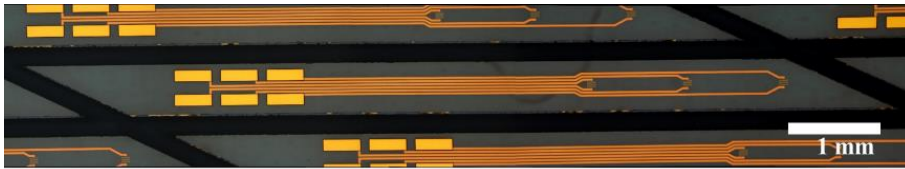


Figure 7-5. Optical microscope image of quartz microneedle.

7.3. Test and calibration

7.3.1. Operation power test

The thermal response of the probe according to the operation power was tested. The sensor is driven at a constant power and the temperature difference is measured. A sensor with $800\ \Omega$ of resistance was used for the experiment. The microneedle probe was inserted into a tomato plant stem about 1.5 cm in diameter. The heating power was increased from 5 mW to 40 mW at intervals of 5 mW and the experiment was repeated.

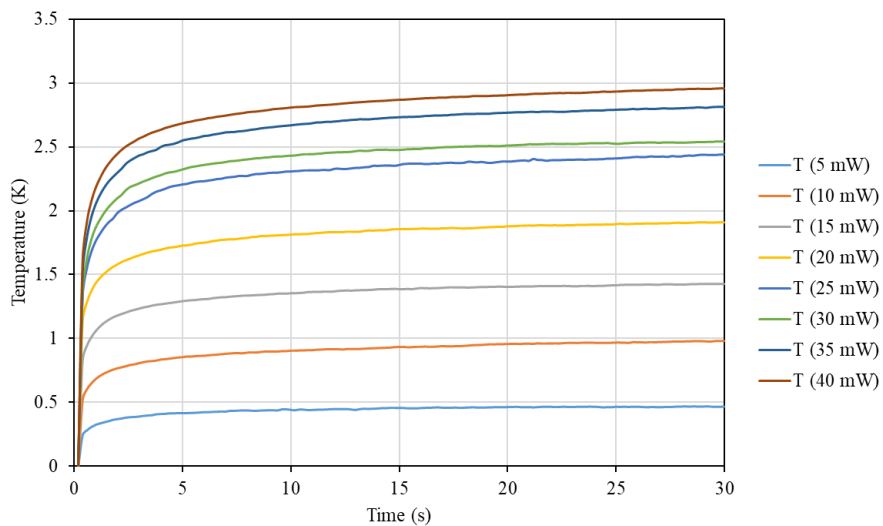


Figure 7-6. Temperature graph of microneedle probe while heating.

Table 7-2. Table of operating voltage, resolution, ADC value change, temperature change by the driving power of microneedle probe.

Power (mW)	Voltage (V)	resolution (K)	ADC value change	ΔT (K)
5	2.00	0.001176	380	0.47
10	2.83	0.000831	1178	0.98
15	3.46	0.000679	2150	1.42
20	4.00	0.000588	3342	1.91
25	4.47	0.000526	4769	2.44
30	4.90	0.00048	5380	2.54
35	5.29	0.000444	6473	2.81
40	5.66	0.000416	7330	2.96

The experimental results are shown in Figure 7-6 and Table 7-2. The temperature change graph during heating of the microneedle probe was similar to that of the exponential decay (Equation 3-16). Table 7-1 shows the detailed experimental conditions and results for each heating power. For example, to drive a sensor with a resistance of 800Ω to 5 mW, 2 V of driving voltage is required. At this time, the minimum temperature change that can be measured using the ADC is 0.00118 K. After heating for 30 seconds, the change in measured value at ADC is 380. The temperature change after heating was 0.47 K. The experiment was repeated while increasing the driving power. The lower driving voltage is preferred because the dielectric layer of the microneedle probe becomes more vulnerable to electrical breakdown as the driving voltage increases. The desirable operating voltage was less than 5 V. The temperature resolution of the electronics decreased as the driving voltage increased. Temperature resolution less than 1 mK was required for precise measurement. The maximum operating temperature difference

was limited to 2.5 K. Taking all of the above into account, the desirable operation power was 20 mW.

3-element lumped capacitance model (Equation 3-35) was used for analysis of heating temperature response of a microneedle probe. Table 7-3 shows the result of curve fitting of the probe temperature variation graph according to the driving power. In the curve fitting results, y_0 represents the temperature rise of the probe when the heating time is infinite. As shown in Figure 7-7, the temperature rise is linearly proportional to the heating power. Figure 7-8 shows the change of time constant by the driving power. There were three time constants in the curve fitting. The shortest time constant (τ_1) is speculated to be related to heat transfer between heater element and probe body which is the fastest thermal equilibrium process. Likewise, τ_2 is speculated to be related to heat transfer between probe body and surrounding plant tissue. The longest time constant (τ_3) is speculated to be related to thermal dissipation of plant tissue. The driving power of microneedle probe did not affect the time constant during transient heat dissipation. The average time constant value of τ_1 , τ_2 , and τ_3 . The coefficient of determinations for curve fitting were above 0.995 for all cases.

Table 7-3. Temperature change curve of probe according to heating power.

Power (mW)	y0 (°C)	A1 (°C)	τ_1 (s)	A2 (°C)	τ_2 (s)	A3 (°C)	τ_3 (s)	R^2
5	0.47	2.31	0.089	0.158	1.11	0.095	8.10	0.99798
10	1.01	4.27	0.097	0.298	1.27	0.206	14.72	0.99929
15	1.43	10.18	0.079	0.458	0.94	0.247	8.52	0.99967
20	1.92	11.55	0.087	0.537	1.12	0.307	9.55	0.99946
25	2.47	9.53	0.106	0.786	1.49	0.340	13.94	0.99936
30	2.55	9.45	0.107	0.862	1.11	0.387	8.44	0.99974
35	2.82	10.90	0.104	0.941	1.09	0.456	9.24	0.9997
40	2.97	11.44	0.105	0.988	1.08	0.456	10.31	0.99975

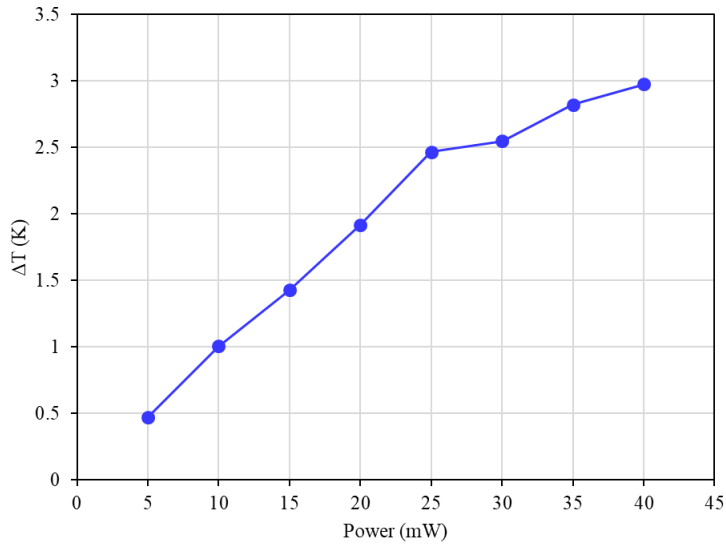


Figure 7-7. Steady state probe temperature according to heating power.

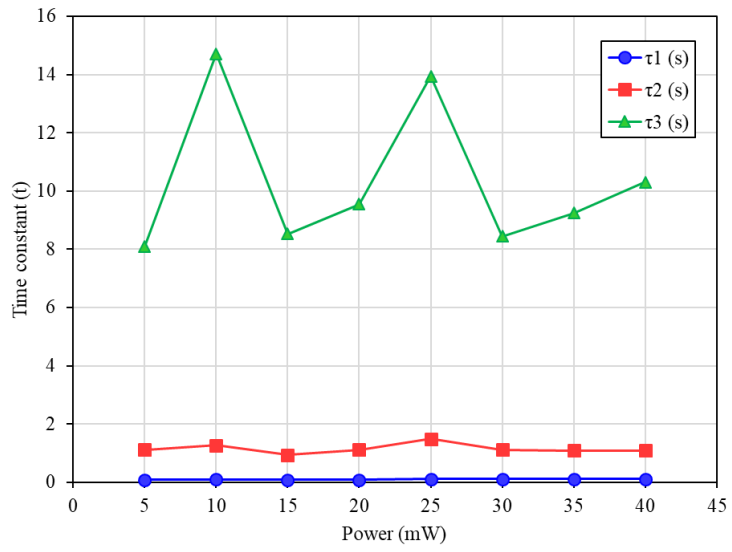


Figure 7-8. Change of time constant according to heating power.

7.3.2. Calibration

The response of the sensor to the xylem flow was calibrated. The calibration procedure was applied to a plant stem to analyze the correlation between the measured signal and the xylem flow (Figure 4-13). A tomato stem sample of 5 cm in length and 2 cm in diameter was collected from a greenhouse. A Mariotte-based test system was used for the calibration. The Mariotte's bottle connected to the stem segment delivered a constant flow. An isotonic saline solution (40 mOsm/L NaCl solution) was prepared and used to prevent xylem bundle deformation due to osmotic pressure during the testing. Two glass columns were inserted into an Erlenmeyer flask. One of the columns was connected the plant segment through a silicon tubing. The column and the tubing were filled with the solution and functioned as a siphon. The height of the Erlenmeyer flask was adjusted to control the hydraulic pressure applied to the plant segment, resulting in varied flow rate. The weight of solution flown through the plant segment was measured with a digital scale (HS-400L, Hansung). The xylem was stained with 0.1 wt.% crystal violet solution after the whole measurement to obtain the cross-sectional area. The picture of stem cross section was taken with digital camera and the area of the xylem was obtained with image processing program (ImageJ, NIH). The gravimetric mass flow rate through plant stem is obtained from the weight increase of scale per unit time. The average flow speed of xylem flow is obtained by dividing mass flow rate by the density of solution and cross-sectional area of xylem. The average xylem flow speed is used as the calibration standard. The temperature of the probe was measured while the probe was generating heat at a constant power (Figure 7-9).

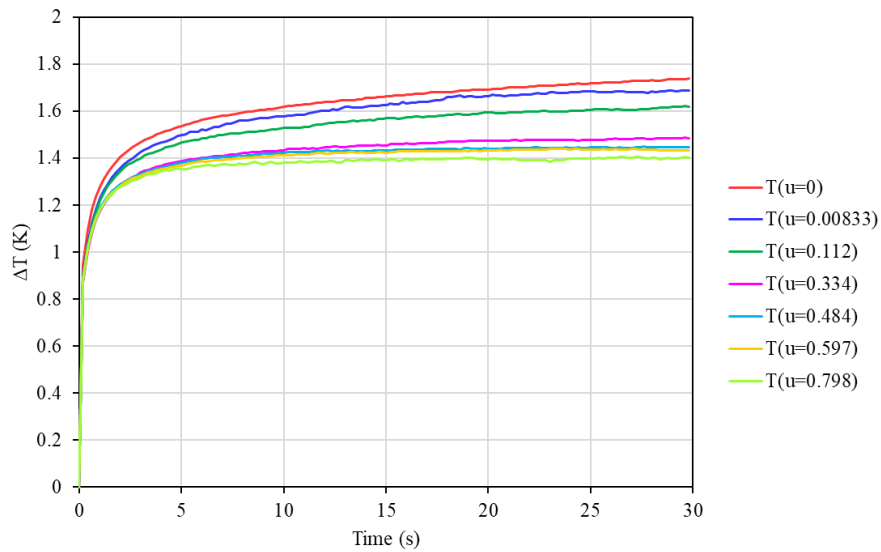


Figure 7-9. Temperature change of heating probe in xylem flow by flow speed.

Based on the 3-component lumped capacitance model obtained from Equation 3-35, the curve fitting of the temperature-time graph was performed. Table 7-4 shows the curve fitting result of time-temperature graph and the 3-component lumped capacitance model. As the flow rate increases, the steady-state heated temperature decreases (Figure 7-10). As the flow rate increases, the time constants τ_1 , τ_2 , and τ_3 decrease (Figure 7-11). The curve fit results were consistent with the 3-component lumped capacitance model and simulation results.

Table 7-4. Curve fitting result of time-temperature graph of heating probe in pipe flow by flow speed based on 3-component lumped capacitance model.

Flow (mm/s)	T_M (°C)	A1 (°C)	τ_1 (s)	A2 (°C)	τ_2 (s)	A3 (°C)	τ_3 (s)	R^2
0	1.77	0.997	0.09729	0.451	1.2458	0.320	13.595	0.9997
0.00833	1.68	0.609	0.00367	0.608	0.9834	0.458	10.151	0.99551
0.112	1.63	0.873	0.08420	0.487	0.3837	0.267	5.976	0.99966
0.334	1.47	0.599	0.00277	0.496	0.3088	0.369	3.064	0.99276
0.484	1.44	0.633	0.00484	0.496	0.3702	0.309	2.694	0.99734
0.597	1.43	0.530	0.00557	0.531	0.2260	0.366	2.463	0.99614
0.798	1.38	0.488	0.00530	0.421	0.5858	0.423	0.620	0.95621

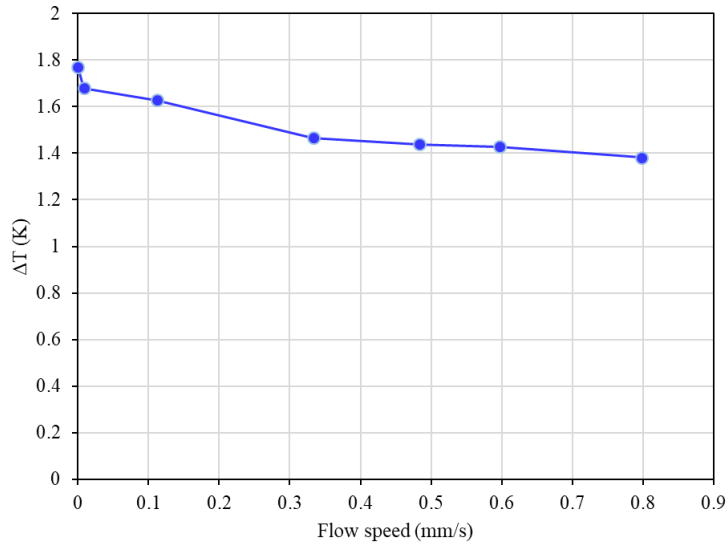


Figure 7-10. Flow speed – steady state heated temperature for xylem flow.

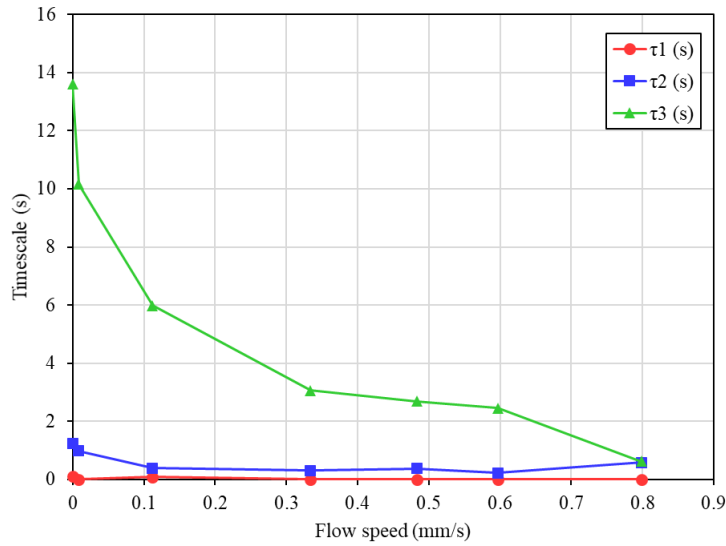
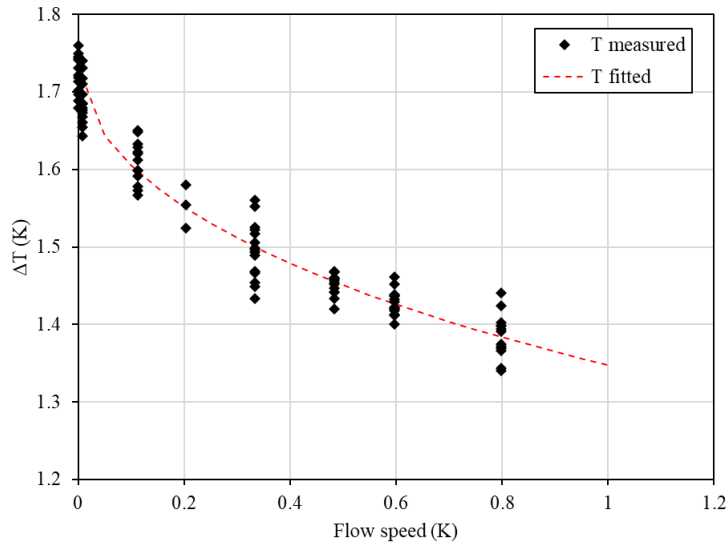


Figure 7-11. Flow speed–exponential dissipation time constant plot for xylem flow.

The measurement was carried out at six different flow speeds from 0 to 0.798 mm/s. The measurement was repeated 10 times for each flow speed. The temperature difference between the heated and the unheated state (ΔT) was measured. Figure 7-12 shows the temperature difference (ΔT) according to the flow rate. Equation 7-1 is the result of curve fitting for the correlation between flow velocity and temperature change using Equation 3-21.



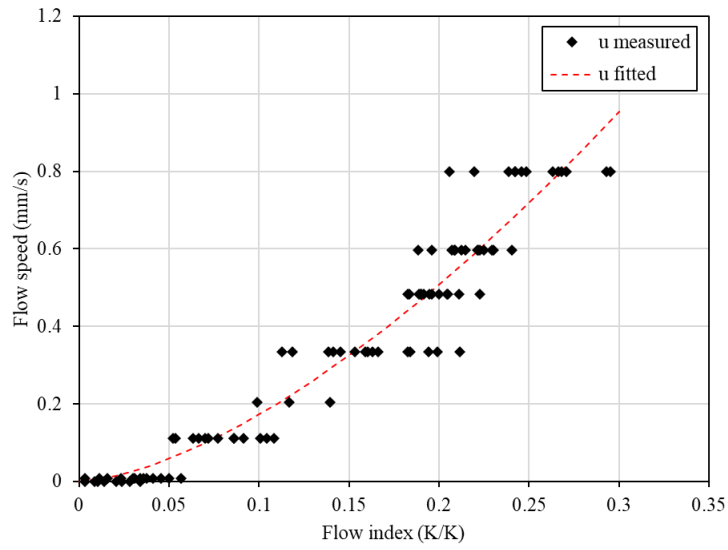


Figure 7-13. Relation between flow index $\left(\frac{\Delta T_M - \Delta T}{\Delta T}\right)$ and flow speed in pipe flow.

7.4. Field application of array measurement sensor

7.4.1. Field measurement method of array sensor

The experiment was conducted in the Gwanak greenhouse (Figure 7-14). The experiment period was from April 5th 2018 to April 30th 2018. Tomato seeds were sown on a rock wool cube and grown for over 30 days. The height of tomato plant was about 30 cm when the sensor is installed. The sensor was installed 10 cm from the root. The sap flow and internal relative temperature of tomato stem were measured with the microneedle sensor. During the experiment, the temperature was maintained at 21°C and the humidity was maintained at 40%.



Figure 7-14. Picture of array measure sensor (left). Array measure sensor installed in tomato plant stem (right).

7.4.2. Field measurement result of array measure sensor

Array measurement of sap flow of tomato stem was conducted for 20 days. Figure 7-15 shows the installed sensor position in a plant stem. The sensor channel

1 is the innermost sensor and channel 3 is the outermost sensor. The depth of each sensor was 1.5, 2.5, 3.5 mm from the epidermis. Figure 7-16 shows the measurement result. The average daytime sap flow speed was around 0.1 mm/s. The diurnal pattern of sap flows from each sensor was similar. However, the magnitude of sap flow rate varied by the measurement depth. Figure 7-16 shows daily integrated sap flow rate. The daily cumulative sap flow rate changed by the date. From Apr. 15th to Apr. 19th, the sap flow rate of channel 1 was higher than other channels and decreased after Apr. 20th. On the other hand, the relative sap flow amount of channel 3 increased during the measurement period. Figure 7-18 shows the cross-sectional image of tomato stem after the sap flow measurement. The xylem area was stained with 0.1% crystal violet solution. The sensor channel 2 and 3, which showed high sap flow, were in contact with the xylem. On the other hand, channel 1, in which the fluid flow was low, was found not to be in direct contact with the xylem.

Through the cross section observation of the plant stem, it was confirmed that the sap flow was measured in the sensor adjacent to the xylem. The sap flow rate of channel 1 was high, but it was decreased over the measurement period. While, the measures sap flow rate of channel 3 increased. The reason for the change in sap flow rate with the depth of the measurement was presumed to be due to the change in the position of the vascular bundle with respect to plant growth (Figure 7-19).

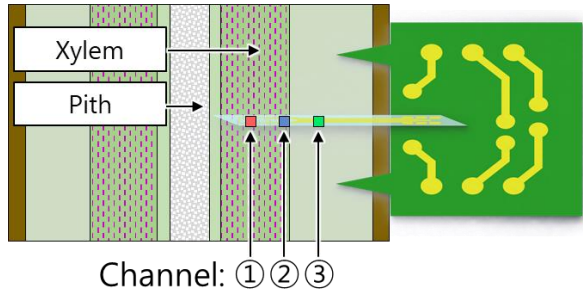


Figure 7-15. Installation of array measurement sensor.

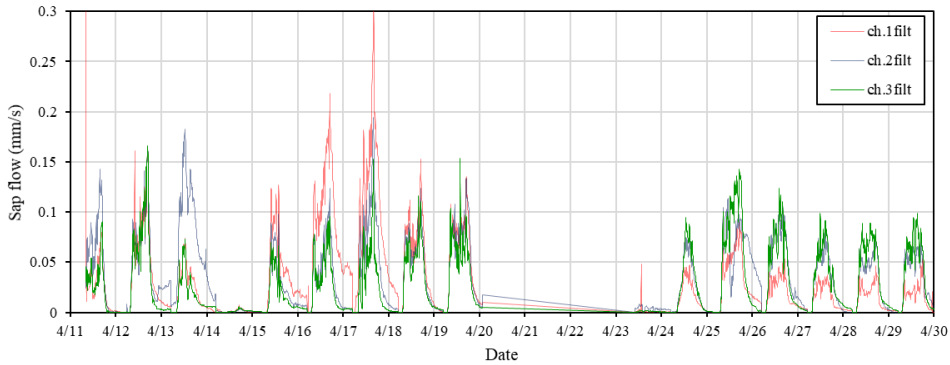


Figure 7-16. Sap flow measure result of array measure sensor.

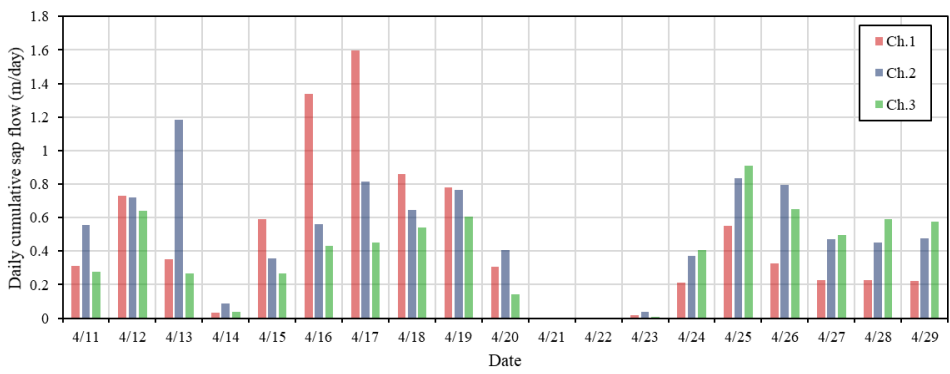


Figure 7-17. Daily cumulative sap flow of array measure sensor.

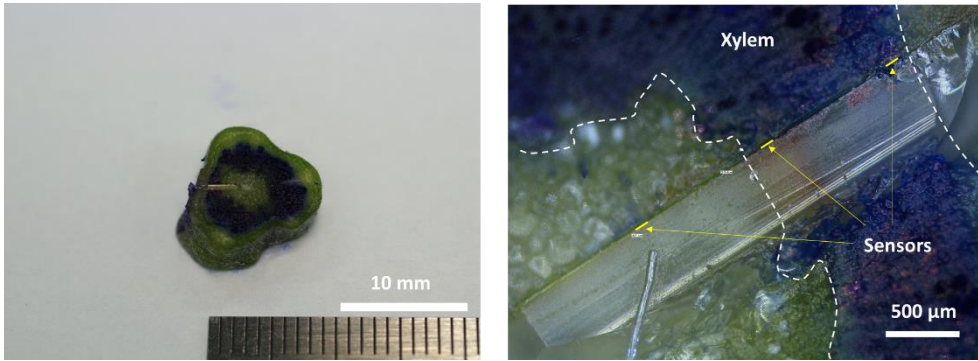


Figure 7-18. Picture of plant stem cross section and installed sensor (left). Microscope image of plant tissue near the installed sensor (right).

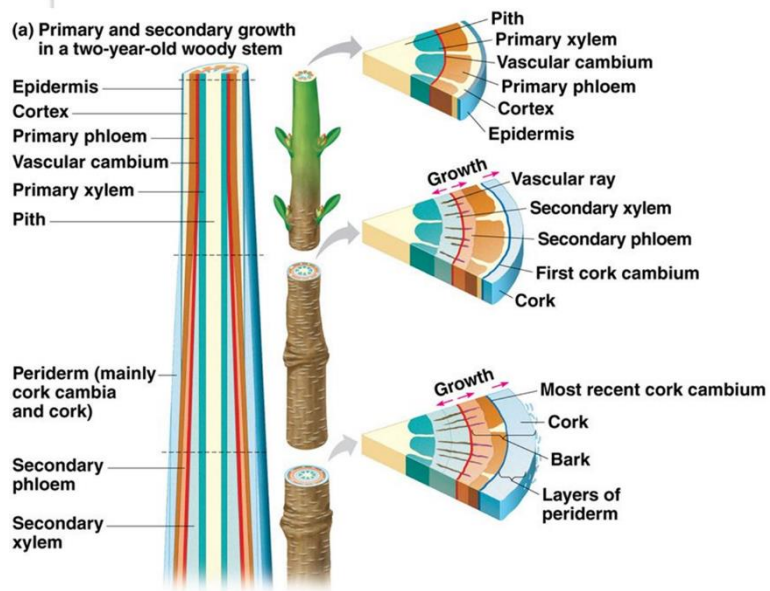


Figure 7-19. Secondary growth in a plant stem [4].

7.5. Conclusion

The microneedle sap flow sensor with silicon substrate had limited local measurement performance due to its high thermal conductivity. Quartz wafer was selected as the substrate material due to its low thermal conductivity and microfabrication compatibility. The microneedle sensor for measuring local sap flow at multiple points is designed and fabricated. The array measurement microneedle sensor was installed on a young tomato stem and measurement was performed for 20 days. Local and array measurement of sap flow signal was obtained during the experiment period. The measured sap flow signal was different depending on the depth of the sensor. The magnitude of the sensor signal according to the depth can be distinguished. And the sensor signal changed with the growth stage. The xylem of the stem was stained. And the cross section of a plant with installed array measurement sap flow sensor was observed with optical microscope. A high sap flow signal was measured near the xylem tissue. This sensor may allow differentiation between plant organs by the sap flow measurement.

Bibliography

- [1] A. A. Myburg, S. Lev-Yadun, and R. R. Sederoff, "Xylem structure and function," eLS, 2013.
- [2] C. W. Windt, F. J. Vergeldt, P. A. De Jager, and H. Van As, "MRI of long-distance water transport: a comparison of the phloem and xylem flow characteristics and dynamics in poplar, castor bean, tomato and tobacco," *Plant, Cell & Environment*, vol. 29, no. 9, pp. 1715-1729, 2006.
- [3] Flax stem cross-section Available from: <https://en.wikipedia.org/>
- [4] Secondary growth in a plant stem Available from: <http://www.bio.miami.edu/>

Chapter 8. Conclusion

A microneedle probe sap flow sensor that can measure the sap flow of a plant in minimally invasive way is presented. The thermometric method that can measure sap flow of plants using a single probe was proposed. The measurement method is based on the thermal dissipation phenomena of a heated object. The sap flow rate is measured by measuring the convective dissipation of the heated probe. The microneedle sensor probe was designed and fabricated with MEMS fabrication process. Thermal and structural design of microneedle probe was conducted. Both surface micromachining and bulk micromachining technology were used for fabrication of microneedle sensor. 40 samples were fabricated on a 4-inch wafer. The yield was higher than 95%. A system for signal measurement and data acquisition of sensors has been configured and evaluated. Analog measurement circuit and microcontroller was used for electronics. The evaluated signal to noise ratio of the measurement circuit was higher than 1500. Various methods for preventing electrical breakdown were applied. The fabrication method, dielectric layer composition, and electronics were modified to increase the lifetime of the sensor.

The thermal characteristics of the microneedle probes were analyzed and verified by simulation. The heat transfer in plant tissue is assumed as conjugated heat transfer in porous media. The steady state and transient thermal response of microneedle probe is predicted with analytical model and confirmed with multiphysics simulation. The simulation result showed a consistent thermal response and predicted the thermal characteristic of the sensor.

The accuracy of the sensor was confirmed and quantitated from the pipe flow

calibration with well-defined system. The thermal characteristic and calibration curve of microneedle sap flow sensor was obtained for pipe flow. The thermal characteristic of microneedle was well fitted with the transfer model. The adjusted R^2 value of our pipe calibration was 0.993. The root mean square error of the measured flow speed was 0.115 mm/s.

In order to measure the sap flow of a 'real plant', additional calibration for xylem flow was necessary for field application. The plant xylem consists of many vascular bundles that is substantially different in heat transfer compared with the simple plastic tube. Thus the response of the sensor to the xylem flow should be different from the response to the pipe flow. The thermal characteristic and calibration curve of microneedle sap flow sensor was obtained for xylem flow. The heat transfer parameters and calibration curve of the sensor in xylem flow was different from those in pipe flow and it was explained in terms of heat transfer model.

The sensors were installed to greenhouse plants to measure the *in-vivo* signal with minimal invasion for 612 days. More than 207 sensors were installed and sap flow and internal relative temperature were measured. Through the tomato artificial light experiment, the sap flow caused by artificial light was measured. Through field experiments, we could measure the sap flow of tomato over 60 days of long period of time. The measured sap flow signal showed a close relationship with the solar radiation and other environmental variables. There was close correlation between the sap flow of tomato and environmental variables such as temperature, light intensity and VPD. Through the irrigation cut experiment, the response of the sap flow to the water stress condition of the plant was observed. Predicting the growth of many plants and comparing the health status of individual

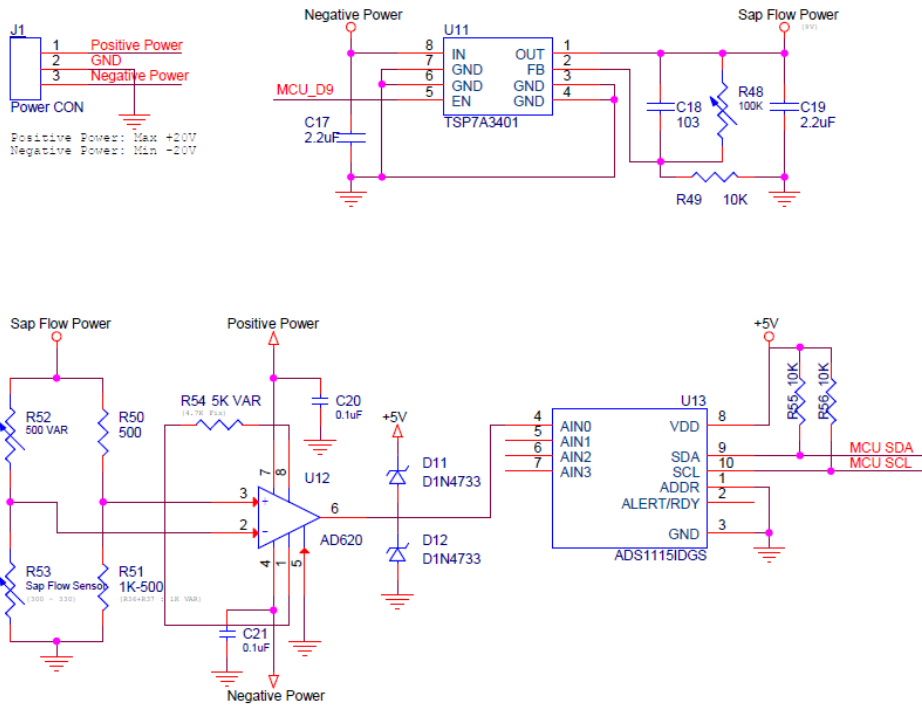
plants method was proposed from the mass measurement and statistical analysis of sap flow data. Measuring the sap flow of peduncle and pedicel suggests a way to infer the hypertrophy of the fruit. The sensors were installed on other herbaceous plants such as paprika, cucumber, clusia, and rubber trees, and were able to measure biochemical information of various plants. Interesting phenomena such as nocturnal sap flow were observed during the experiment.

Microneedle sap flow sensor has many advantage with its simple configuration and small size. By using temperature detection via resistance, heating and temperature measurement is possible with a single electrode on a single probe. This enables simple and reliable measurement. The small size of the probe minimizes the invasion and disturbance to plant growth. Small thermal capacity increases the sensitivity with better time resolution while the thermal impact on the plant is kept low.

The microneedle probe has a very small sensing part. This will possibly allow measuring the local water transportation at a particular organ of a plant, which will be useful for plant physiological research. The microneedle probe platform is not limited to the sap flow measurement but can be incorporated with other in vivo sensing techniques such as electrical conductivity, ion concentration, or nutrition monitoring. The silicon-based microsensors will open up new opportunities for the agricultural applications due to their physical benefits and economical cost. Sensing quality will increase as a large number of sensors are implanted on many plants, representing the state of a whole farm. The productivity and the quality of agricultural products will be improved by accessing the key information of plants in the precision farming.

Appendix

A. Circuit diagram of measurement circuit.



B. Matlab code for sap flow conversion

```
xmin= datetime('2018-01-01 00:00:00');
xmax= datetime('2018-01-31 00:00:00');
day= (xmin:1:xmax).';

N=length(t);
M=length(day);

tick= 12;
SFmin= -0.0;
SFmax= 1;
Tmin= -5;
Tmax= 5;

alpha=4.45;
beta=1.83;

TCR=0.0034;
gain=49.4/2.2+1;
ADCrange=4.096*3/2;
ADCsteps=2^15;
Vcc=9;
Rwire=180;
Rref=180;
sap_area=200;

filter= 1;
cutoff_freq = 600^-1;
sample1 = 120^-1;
order1 = 1;
cutoff1 = cutoff_freq / sample1 *2;
[b,a]=butter(order1,cutoff1,'low');
value_filter_nodelay=filtfilt(b,a,value);

if filter == 0
    temp_differ =
1/TCR/gain/ADCsteps*ADCrange/Vcc*(Rwire+Rref)/Rwire*value;
else
    temp_differ =
1/TCR/gain/ADCsteps*ADCrange/Vcc*(Rwire+Rref)/Rwire*value_filter_nodel
ay;
end

calibration_method = 2;

if calibration_method == 0
```

```

for m=1:M
    temp_differ_max(m) = 1.46;
end
end

if calibration_method == 1
for m=1:M
    index=find( (xmin +m-1 +hours(5) <= t) & (t < xmin +m-1
+hours(6)) );
    Tm_value(m) = mean(value(index));

    if isnan(Tm_value(m))
        if m==1
            Tm_value(m)=1;
        else
            Tm_value(m) = Tm_value(m-1);
        end
    end
end
end
Tm_value(1) = Tm_value(2);
temp_differ_max=
1/TCR/gain/ADCsteps*ADCrange/Vcc*(Rwire+Rref)/Rwire*Tm_value;
end

if calibration_method == 2
    value_moving_avg = movmean(value,30);
for m=1:M
    index = find( (xmin +m-2 +hours(18) <= t) & (t < xmin +m-1
+hours(9)) );

    if isempty(max(value_moving_avg(index)))
        if m==1
            Tm_value(m) = 1;
        else
            Tm_value(m) = Tm_value(m-1);
        end
    else
        Tm_value(m) = max(value_moving_avg(index));
    end
end

end
Tm_value(1) = Tm_value(2);
temp_differ_max=
1/TCR/gain/ADCsteps*ADCrange/Vcc*(Rwire+Rref)/Rwire*Tm_value;
end

```

```

dailycalibrate=1;
if dailycalibrate==1
    for m=1:M
        index = find( (xmin +m-1 +hours(5) <= t) & (t < xmin +m
+hours(5)) );
        TDP(index) = ((temp_differ_max(m)-
temp_differ(index))./temp_differ(index));

sap_flux_density(find(TDP>0))=alpha*real(TDP(find(TDP>0)).^beta);
        sap_flux_density(find(TDP<=0))=0;

        end
    else
        sap_flux_density=alpha.*real(((temp_differ_max(1)-
temp_differ)./temp_differ).^beta);
        end

        if calibration_method == 0
            sap_flux_density = sap_flux_density.';
        end
        sap_flux=sap_flux_density*sap_area;
        Z_g = cumtrapz(t,sap_flux);
        Z_g = seconds(Z_g);
        Z_g = Z_g.*1E-6;

        duration=days(max(t)-min(t));
        for m=1:1+duration
            daily_irrigation(m) = Z_g(min(find(xmin +m <= t)))-
Z_g(min(find(xmin +m-1 <= t)));
        end

        daily_irrigation=daily_irrigation.';

figure()
plot(t,sap_flux_density,'b')
xlabel('time(dd)')
ylabel('velocity(mm/s)')

xlim([xmin xmax])
ylim([SFmin SFmax])
set(gca,'XTick',[xmin:tick:xmax])
datetick('x','HH','kepticks')

figure()
plot(t,Z_g,'b')
xlabel('time(hh:mm)')
ylabel('transpiration(l)')

```

```
figure()
reltemp=reltemp-reltemp(10);
plot(t,reltemp,'b')
xlabel('time(HH)')
ylabel('relative temperature(C)')
xlim([xmin xmax])
ylim([Tmin Tmax])
set(gca,'XTick',[xmin:tick:xmax])
datetick('x','HH','keepticks')
```

C. Processing code for data acquisition

```
import processing.serial.*;
Serial myPort;

int numChannel = 4; //number of channels
int numValue = 3; // number of input values or sensors, 0:Channel, 1:
Datasort, 2:Data
int numData = 3; //numbers of graph per each channel
int numGraph = numChannel * numData; // number of graphes

//constants
float e=2.718281828459;
//euler number

long ADC_max = (long)pow(2,15)-1;
long ADC_min = 0;
long delta_max = (long)pow(2,14);
long delta_min = 0;
float vel_max = 1000;
float vel_min = -1000;
color ADC_color = color(255, 0, 0);
color delta_color = color(0, 0, 255);
color vel_color = color(0, 255, 0);
color bg_color = color(0, 0, 0);
int txt_size = 18;

float[] value = new float[]{0,0,0};
float[][] max = new float[][]{{ADC_max, delta_max, vel_max},{ADC_max,
delta_max, vel_max},{ADC_max, delta_max, vel_max},{ADC_max, delta_max,
vel_max}};
float[][] min = new float[][]{{ADC_min, delta_min, vel_min},{ADC_min,
delta_min, vel_min},{ADC_min, delta_min, vel_min},{ADC_min, delta_min,
vel_min}};
color[][] valColor = new color[][]{{ADC_color, delta_color,
vel_color},{ADC_color, delta_color, vel_color},{ADC_color, delta_color,
vel_color},{ADC_color, delta_color, vel_color}};

float partH; // partial screen height
float[][] mappedVal = new float[numChannel][numData];
float[][] mappedVal_old = new float[numChannel][numData];

int[][] xPos = new int[numChannel][numData]; // horizontal position of the
graph
int[][] xPos_old = new int[numChannel][numData];
boolean[][] clearScreen = new boolean[numChannel][numData]; // flagged
when graph has filled screen

int ch = 0; //channel
```

```

int type = 0; //datatype
float data = 0; //data value
float vel = 0; //velocity
PrintWriter output;

void setup() {
    size(500, 1000);
    partH = height / numGraph;

    myPort = new Serial(this, "COM12", 9600);

    myPort.bufferUntil('\n');
    output = createWriter(year()+" "+month()+" "+day()+" "+hour()+" "+minute()+" .txt");

    textSize(txt_size);
    background(bg_color);
    noStroke();

    output.println("channel,type,value,"+"YYYY"+"-"++"MM"+"-"++"DD"+" "+:"hh"+" ":"mm"+" ":"ss");
}

void draw()
{

    for(int i = 0; i < numData; i++)
    {
        if (clearScreen[ch][i])
        {
            fill(0);
            noStroke();
            rect(0,partH*(ch*3+type),width,partH);
            clearScreen[ch][i] = false; // reset flag
        }
    }

    if(type==0) //draw ADC value
    {

        // map to the range of partial screen height:
        mappedVal[ch][type] = map(data, min[ch][type], max[ch][type], 0,
partH);

        // draw lines:
        stroke(valColor[ch][type]);
        line(xPos[ch][type], partH*(ch*3+type+1), xPos[ch][type],
partH*(ch*3+type+1) - mappedVal[ch][type]);
    }
}

```

```

// draw dividing line:
stroke(255);
line(0, partH*(ch*3+type+1), width, partH*(ch*3+type+1));

// display values on screen:
fill(30);
noStroke();
rect(0, partH*(ch*3+type)+1, 150, txt_size+2);
fill(255);
text(round(data), 2, partH*(ch*3+type)+txt_size);
fill(125);
text("/"+round(max[ch][type]), 80, partH*(ch*3+type)+txt_size);
fill(0);
noStroke();
rect(250, partH*(ch*3+type)+1, 150, txt_size+2);
fill(255);
text("Ch "+ch+" ADC value", 250, partH*(ch*3+type)+txt_size);
}

if(type==1) //draw differential value
{

// map to the range of partial screen height:
mappedVal[ch][type] = map(data, min[ch][type], max[ch][type], 0,
partH);

// draw lines:
stroke(valColor[ch][type]);
line(xPos[ch][type], partH*(ch*3+type+1), xPos[ch][type],
partH*(ch*3+type+1) - mappedVal[ch][type]);

// draw dividing line:
stroke(255);
line(0, partH*(ch*3+type+1), width, partH*(ch*3+type+1));

// display values on screen:
fill(50);
noStroke();
rect(0, partH*(ch*3+type)+1, 150, txt_size+2);
fill(255);
text(data, 2, partH*(ch*3+type)+txt_size);
fill(125);
text("/"+max[ch][type], 80, partH*(ch*3+type)+txt_size);
fill(0);
noStroke();
rect(250, partH*(ch*3+type)+1, 150, txt_size+2);
fill(255);

```

```

        text("Ch "+ch+" delta", 250, partH*(ch*3+type)+txt_size);
        output.flush();
    }

void serialEvent(Serial myPort) {
    try
    {
        String inString = myPort.readStringUntil('\n');

        if (inString != null)
        {
            inString = trim(inString);

            value = float(splitTokens(inString, ", \t")); // delimiter can be comma
space or tab
            ch = (int)value[0];
            type = (int)value[1];
            data = value[2];

            output.print(ch);
            output.print(",");
            output.print(type);
            output.print(",");
            output.print(data);
            output.print(",");
            output.println(year()+"-"+month()+"-
"+day()+" "+hour()+":"+minute()+":"+second());

            if(type == 1)
            {
                if(data>=threshold_H[ch])
                {
                    vel = v_min;
                }
                else if(data<=threshold_L[ch])
                {
                    vel = v_max;
                }
                else
                {
                    vel = pow(e, a[ch] + b[ch] * data + c[ch] * pow(data,2) );
                }
                vel = data * 10;
                output.print(ch);
                output.print(",");
                output.print(2);
                output.print(",");
                output.print(vel);
            }
        }
    }
}

```

```

        output.print(",");
        output.println(year()+"-"+month()+"-
"+day()+","+hour()+":"+minute()+":"+second());
    }

    if (value.length >= numValue)
    {

        if (xPos[ch][type] >= width)
        {
            xPos[ch][type] = 0;
            xPos_old[ch][type] = 0;
            clearScreen[ch][type] = true;
        }
        else
        {
            xPos[ch][type]++; // increment the graph's horizontal position
            if(type==1)
            {
                xPos[ch][type] = xPos[ch][type]+4;
            }
        }
    }
}
}
}
catch(RuntimeException e) {

    e.printStackTrace();
}
}

void keyPressed() {

    if (keyCode==ESC){
        output.flush(); // Writes the remaining data to the file
        output.close(); // Finishes the file
        exit();
    } // Stops the program
    else{
    }
}
}

```

D. Arduino code for measurement

```
#include <Wire.h>
#include <Adafruit_ADS1015.h>
Adafruit_ADS1015 ads(0x48);
#define BUTTON 2

char mode=0;
long val[4]={0,};
long valavg[4] = {0,};
long high_avg[4] = {0,}, low_avg[4] = {0,}, delta[4] = {0,};
long vel[4] = {0,};
int i=0, j=0, k=0, l=0, m=0;
float e=2.718281828459;

float running_time = 30;
int idle_time = 0;
int sampling_rate = 5;
int average_samples = 5;

int dt = 1000 / average_samples / sampling_rate;
unsigned int num_loops = running_time * sampling_rate;
unsigned int idle_time_ms = (idle_time) * 1000;

void calibrate(int ch);
void adc(int ch);

void setup()
{
  Serial.begin(9600); //baud rate = 9600
  pinMode(BUTTON, INPUT);
  pinMode(9,OUTPUT);
  pinMode(10,OUTPUT);
  pinMode(11,OUTPUT);
  pinMode(12,OUTPUT);
  attachInterrupt(digitalPinToInterrupt(BUTTON), toggle, HIGH);
  ads.begin();
}

void loop()
{
  if (mode == 0) //continous mode
  {
    for(m=0;m<=3;m++) //Ch 0-3 operation
    {
      calibrate(m);
    }
  }
}
```

```

else if (mode == 1) //on/off mode, get
differential value
{
    for(m=0;m<=3;m++) //Ch 0-3 operation
    {
        if(mode != 1)
        {break;}
        adc(m); //AD convert & send
    }
    for(i=1;i<=idle_time;i++) //delay while idle time
    {
        if(mode != 1)
        {break;}
        delay(1000);
    }
}

else
{}
}

void calibrate(int ch)
{
    for(i=9;i<=12;i++) //set pin 9~12 low
    {
        digitalWrite(i,LOW); //stop
    }
    digitalWrite(ch+9,HIGH); //run specific channel

    for(j=1;j<=average_samples;j++)
    {
//        val[ch] = val[ch] + analogRead(ch);
        val[ch] = val[ch] + ads.readADC_SingleEnded(ch);
        delay(dt);
    }

    val[ch] = val[ch] / average_samples;
    valavg[ch] = val[ch];
    val[ch] = 0;
    Serial.print(ch);
    Serial.print(',');
    Serial.print(0);
    Serial.print(',');
    Serial.print(valavg[ch]);
    Serial.print(',');
    Serial.print("\n");
    digitalWrite(ch+9,LOW);
return;

```

```

}

void adc(int ch)
{
    for(i=9;i<=12;i++)
    {
        digitalWrite(i,LOW);
    }
    digitalWrite(ch+9,HIGH);

    for(k=1;k<=num_loops;k++)
    {
        if(mode != 1)
            {break;}

        for(j=1;j<=average_samples;j++)
        {
            val[ch] = val[ch] + ads.readADC_SingleEnded(ch);
            delay(dt);
        }
        val[ch] = val[ch] / average_samples;
        valavg[ch] = val[ch];
        val[ch] = 0;

        for(l=1;l<=1;l++)
        {
            if(k == 1)
            {
                high_avg[ch] = high_avg[ch] + valavg[ch];
            }
        }
        high_avg[ch] = high_avg[ch] / 1;

        for(l=num_loops;l<=num_loops;l++)
        {
            if(k == 1)
            {
                low_avg[ch] = low_avg[ch] + valavg[ch];
            }
        }
        low_avg[ch] = low_avg[ch] / 1;
    }
    Serial.print(ch);
    Serial.print(',');
    Serial.print(0);
    Serial.print(',');
    Serial.print(valavg[ch]);
    Serial.print(',');
    Serial.print('\n');
}

```

```

    }

    delta[ch] = - high_avg[ch] + low_avg[ch];
    Serial.print(ch);
    Serial.print(',');
    Serial.print(2);
    Serial.print(',');
    Serial.print(high_avg[ch]);
    Serial.print(',');
    Serial.print('\n');

    Serial.print(ch);
    Serial.print(',');
    Serial.print(1);
    Serial.print(',');
    Serial.print(delta[ch]);
    Serial.print(',');
    Serial.print('\n');

    high_avg[ch] = 0;
    low_avg[ch] = 0;
    digitalWrite(ch+9,LOW);
return;
}

void toggle()
{
#if 1
    if(digitalRead(BUTTON) == HIGH)
    {
        delay(20);
        if(digitalRead(BUTTON) == HIGH)
        {
            // Serial.print('t');
            //Serial.print('\n');
            mode++;
            if (mode == 2)
            {mode = 0;}
        }
    }
#else
    mode++;
    if (mode == 2)
    {mode = 0;}
#endif
}

```

국문 초록

미세 바늘 센서를 이용한 생체 내 수액 흐름 측정 시스템

서울대학교 대학원

기계항공공학부

백상웅

식물의 수액 흐름을 측정하고 이해하는 것은 식물 생리학적 연구와 미래 농업 분야에서 응용을 위해 중요하다. 예를 들어 현대 수경재배에서 작물의 수액 흐름을 측정함으로써 태양광, 온·습도, 배지 수분 함량에 따른 식물의 반응을 측정할 수 있다. 그러나 기존의 수액 흐름 측정 방법들은 대형 목본 식물들에 국한되어 있다는 단점이 있다. 따라서 수경 재배 작물인 토마토나 파프리카와 같은 소형 초본 식물들은 기존 수액 흐름 측정장비의 이용이 제한된다. 본 연구에서는 소형 초본 식물의 수액 흐름을 측정하기 위해 미세 열 탐침이 제안되었고 개발되었다. 단일 미세 열 발산 탐침을 이용해 식물의 수액 흐름을 측정하는 방법이 제안되었고 탐침의 열적 특성이 분석되었다. 미세탐침 수액흐름 센서가 MEMS제작 공정을 이용해 제작되고 캘리브레이션이 이루어졌다. 전자회로와 데이터 수집장치를 포함한 측정 시스템이 제작되었다. 센서는 토마토를 포함한 시설원예 작물에 설치되어 식물의 체내 상대온도와 수액 흐름을 측정했다. 총

612일간의 측정 기간동안 207개 이상의 센서가 설치 되어 식물의 생체 정보를 측정하였다. 측정된 수액 흐름 신호는 태양광, 기온 등 환경변화에 의한 식물의 반응과 밀접한 연관성을 보였다. 32개 이상 복수의 센서를 동시에 설치해 측정데이터의 통계적 분석이 시도되었다. 개별 센서는 3개월 이상의 연속 측정이 가능했다. 단일 프로브를 이용함으로써 측정이 단순하며 식물에 가해지는 침습을 최소화 할 수 있었다. 센서는 MEMS 미세제작공정을 이용하여 제작되므로 높은 제작의 신뢰성과 양산성을 가진다. 따라서 저비용, 대량으로 생산되어 개별 작물의 생체 신호 모니터링과 생체 신호의 통계적 분석이 가능하다.

주요어: 유속 측정, 생체 내 센서, MEMS, 식물 이식형 센서